Computational and Experimental Investigation of Magnetic Nanoparticle Based Hyperthermia

A thesis submitted in fulfillment of the requirement for the award of the degree of

DOCTOR OF PHILOSOPHY

IN

MECHANICAL ENGINEERING

Submitted by:

Sandeep

(Registration No. : 901708017)

Under the supervision of

Dr. Neeraj Kumar
Assistant Professor,
Mechanical Engineering Department
TIET, Patiala.

Dr. Pramod Kumar Avti
Additional Professor
Department of Biophysics,
PGIMER, Chandigarh.

Department of Mechanical Engineering

Thapar Institute of Engineering & Technology, Patiala-147004, India

(Deemed to be University)

January, 2024

CERTIFICATE

I, Sandeep, Registration No. 901708017, hereby declare that the work being presented in this thesis entitled "**Computational and Experimental Investigation of Magnetic Nanoparticle Based Hyperthermia**" submitted to the Department of Mechanical Engineering at Thapar Institute of Engineering and Technology, Patiala, India is an authenticated record of my research work for the award of the degree "Doctor of Philosophy" under the supervision of **Dr. Neeraj Kumar**, Assistant Professor, Mechanical Engineering Department, TIET, Patiala, India, and Dr. **Pramod Kumar Avti,** Additional Professor, Department of Biophysics, PGIMER, Chandigarh, India. This report has not been submitted to any other institute for the award of any other degree.

Sandeep

Reg. No. 901708017

Place: Patiala, Punjab (India)

Dated: 16 January 2024

This is to certify that the above declaration made by the student is correct to the best of our knowledge.

Verified By:

Dr. Neeraj Kumar
(Supervisor)
Assistant Professor,
Mechanical Engineering Department
Thapar Institute of Engineering and Technology
Patiala-147004, Punjab, India.

Dr. Pramod Kumar Avti
(Co-supervisor)
Additional Professor
Department of Biophysics,
PGIMER, Chandigarh-160012,
India.

ACKNOWLEDGMENT

I dedicate my Ph.D. thesis work at the Thapar Institute of Engineering and Technology Patiala, Punjab, India, to my beloved family members. The undertaking of this Ph.D. has been a truly life-changing experience for me, and I would not have been able to complete it without the assistance and guidance of many people.

First and foremost, I wish to express my sincere gratitude to **Dr. Neeraj Kumar** and **Dr. Pramod Kumar Avti,** my supervisors, for their constant support and guidance at all stages of my Ph.D. The work would not have been possible without their valuable input, advice, and support. I am thankful for the positive suggestions and meticulous guidance that helped me to improve my scientific research skills. I would like to thank **Dr. Bhupendra Kumar Chudasama** for his valuable input and suggestions on magnetic hyperthermia.

I am grateful to my Ph.D. committee, which includes **Dr. Tarun Kumar Bera** (Chairman, Board of Studies), **Dr. Mudhup Mittal**, **Dr. Rajesh Kumar Shukla**, TIET, Mechanical Engineering Department, and **Dr. Surendra Deo Tiwari**, Associate Professor, School of Physics and Material Science, TIET, for keeping track of my progress and giving helpful suggestion to improve the work. I am also thankful to **Dr. Tarun Nanda** and **Dr. Gagandeep Bhardwaj**, our Ph.D. coordinators, for their approachability and for keeping me informed with all the relevant communication. I also extend my thanks to the entire staff (Teaching/Non-teaching) of the Mechanical Engineering Department for their constant support and cooperation.

I am grateful to acknowledge the financial support provided by the TIET- Virginia Tech Center of Excellence in Emerging Materials (CEEMS). I am thankful to my colleagues, friends, lab mates, and whoever crossed my path in this research journey. I am thankful to my parents and all other family members for their love and great support for me. Aside from the individuals mentioned above, I would like to thank "**Almighty God**," who has granted me countless blessings, knowledge, and opportunities to pursue and complete this research so that I can finally accomplish the thesis.

Abstract

Magnetic hyperthermia cancer treatment, uses magnetic nano-particles as heating source. In this magnetic nanoparticle hyperthermia (MNPH), heat is generated locally through nanoparticles induced to the targeted tissue (tumor tissue) under the influence of external magnetic field. This hyperthermia applicator has higher spatial control of heat generation thus targeted damage could be induced to tumor tissue while minimizing the thermal damage to the neighbouring healthy tissue. However, this novel therapy has some limitations and challenges in its practical implementation. These challenges are in the form of magnetic nanoparticle (MNP) heating power enhancement, regulating their dose and distribution, achieving spatial control of tumor temperature by multisite injections, and ensuring the safe infusion of particles. The present study aims to address these challenges and limitations to make magnetic hyperthermia applicable to the future cancer treatment therapy.

The important parameters for efficient heating in MNPH are the MNP's properties, size, materials, and externally applied magnetic field parameters (amplitude and frequency). A numerical investigation is done to analyze the effects of these parameters on heat generation for three nanoparticle systems ($CoFe_2O_4$, Fe_3O_4, and $MnFe_2O_4$. The quantification of specific loss power (SLP) or heat generation of different nanoparticle systems, which is influenced by their size-dependent magnetization (M_S) and the anisotropy energy has been done. Correlations for magnetization (M_S) and the anisotropy energy based on the previously reported experimental data have been established. These correlations are introduced into the Rosensweig model of induction heating for considered MNP systems. The comparisons show that SLP estimation using MNP size-dependent saturation magnetization (M_S) are much closer to the experimentally reported values of SLP for all three MNP systems in comparison to SLP estimated by fixed values of saturation magnetization on (M_S) and anisotropy energy constant (K_{eff}). Results show that dissipated power reaches a peak at a specific nano-particle size (D_O). However, the (D_O) varies with the magnetic field frequency and amplitude. It is also concluded that a particular size of MNP at resonant amplitude and frequency generates the maximum SLP. Additionally, in *In Intro* study, the SLP of magnetite (Fe_3O_4) nanoparticles dispersed in agar gel has been measured using a hyperthermia applicator (NAN201003 Magnetherm Applicator). The experimental temperature profiles were compared with the computational profile obtained using the bioheat model. The numerical results are in good agreement with

experimental results. This increases the confidence and applicability of the simulated results of MNPH for further computational investigation of MNPH.

In the first computational investigation of MNPH, tumor tissue position (depth) with respect to the skin surface as well as clinical environment conditions have been changed. The three-dimensional (3D) breast tumor model, enclosed by the healthy tissue is used for MNPH simulations. The position and heat transfer rate through the skin are altered to evaluate their effect on MNPH. The embedded tumor tissue (of size 1.5 cm) is positioned at six different depths with respect to the top surface and three heat transfer coefficients ($h_c = 2.5, 5, and\ 7.5\ W/m^2K$) on the skin are considered to simulate a wide range of clinical environment conditions during MNPH. The values of h_c is calculated from the analytical relations derived for natural and forced convection heat transfer from different posturing and ambient conditions exposed on human mannequin in literature. MNPH is induced for 1 hour with two heating powers (10 kA/m and 12.5 kA/m at 130 kHz) to assess thermal damage (Arrhenius (Ω=4.6) and cumulative equivalent minutes $(CEM43)_{60}$ in the tissue. Results show that a critical depth exists, which is nearly half of the tumor size, up to which the MNPH is influenced by the position of the tumor. Similarly, the effects of the ambient conditions during this thermotherapy on thermal dosimetry also cease beyond this critical depth. The estimation of the critical depth of the tumor will help in predicting the therapeutic effects of magnetic hyperthermia applicators for specifically positioned tumors in actual environmental conditions.

Further, the computational investigations are carried out to determine the breast tumor size-dependent MNP dose (mg of MNP/cm^3 of tumor tissue) for MNPH. The investigation is done through the simulations on the tumor models generated from DCE_MRI DICOM images of the patient's breast cancer from TCIA ('The Cancer Imaging Archive'). Five tumor models are produced from MRI data using 3D slicer software, ranging from 3 cm^3 to 15 cm^3. The FEM-based solver (COMSOL multi-physics) is used to simulate bioheat transfer physics in all five extracted models. Single and multipoint injection strategies have been used to induce MNP in tumor tissues. The required MNP dose that may induce necessary therapeutic effects is evaluated by comparing the therapeutic effects produced by constant dose (*CD*) (5 mg/cm^3) and variable reduced dose (*RD*) (5.5-2.8 mg/cm^3) methodologies. The current observation states that for the requisite therapeutic effects, injected MNP doses (mg/cm^3) should not remain constant as the size of the tumor increases. In fact, MNP dose (mg/cm^3) should be reduced as the size of the tumor increases. Results also show that *RD* works better with a multi-injection strategy than a single injection of MNP. It has been found that the effective MNP

dose (mg/cm^3) is reduced by 50% for the biggest tumor size (15 cm^3) using multi-injection MNP delivery with respect to the smallest tumor (3 cm^3) selected in this study.

Using the DICOM database, a more realistic tumor model has been developed. A more accurate physical model for MNPH application has an artery embedded inside the tumor. The MNP particles are infused to the tumor tissue using a multipoint injection strategy to gain a homogenous temperature distribution. The thermal damage of the tumor region has been evaluated with two conditions, i.e., with the flow and without the flow of blood through the artery. It has been observed that arterial blood flow, transports a substantial amount of heat. This reduces the thermal damage to tumor tissue during hyperthermia. It was noticed that the thermal damage was reduced by 25% due to the arterial blood flow in the partially submerged artery in the tumor region. It is concluded that besides the MNP distribution, its dose, and injection sites, the therapeutic effects of MNPH is significantly influenced by the blood vessels and arteries surrounding the tumor. The investigations carried out in this thesis aim to generate knowledge domain for MNPH that may help to optimize this therapy for future clinical applications.

List of publications

1. **Nain, Sandeep**, Neeraj Kumar, and Pramod Kumar Avti. "Computational investigation of the tumor position and ambient conditions on magnetic nanoparticle thermo-therapy." *Thermal Science and Engineering Progress* 34 (2022): 101396. https://doi.org/10.1016/j.tsep.2022.101396 **(SCI Journal, IF 4.8).**

2. **Nain, Sandeep**, Neeraj Kumar, Bhupendra Chudasama, and Pramod Kumar Avti. "The SLP estimation of the nanoparticle systems using size-dependent magnetic properties for the magnetic hyperthermia therapy." *Journal of Magnetism and Magnetic Materials* 565 (2023): 170219. https://doi.org/10.1016/j.jmmm.2022.170219 (**SCI Journal, IF 2.7**).

3. **Nain**, **Sandeep,** N. Kumar, and P. K. Avti, "Tumor size dependent MNP dose evaluation in realistic breast tumor models for effective magnetic hyperthermia.," *Med. Eng. Phys.*, p. 104065, 2023, https://doi.org/10.1016/j.medengphy.2023.104065 (**SCI Journal, IF 2.2**).

Contents

List of Figures

List of Table

Nomenclature

Roman Letters

A	Collision frequency factor of molecules (s^{-1})
C	Percentage of undamaged tissue
C_d	Thermal damage parameter
c_p	Specific heat ($Jkg^{-1}k^{-1}$)
D*	Tumor's location depth, and its size ratio
E_a	Activation energy barrier ($Jmol^{-1}$)
f	Magnetic field frequency (kHz)
H_0	Magnetic field strength (kAm^{-1})
h_c	Convective heat transfer coefficient (W/m^2K)
k	Thermal conductivity ($Wm^{-1}K^{-1}$)
K_B	Boltzmann constant ($J\ K^{-1}$)
L	Size of healthy tissue (cm)
$L_{...}$	Non-dimensional (N-D) tissue length
m	Mass of magnetic nanoparticles (mg)
Q_m	Metabolic heat generation (Wm^{-3})
Q_s	External heat source (Wm^{-3})
R	Universal gas constant ($8.314\ Jmol^{-1}K^{-1}$)
$Radius_{MNP}$	Radius of nanoparticles (m)
T	Temperature (℃)
t	Time (s)
V	Ambient air velocity (ms^{-1})
w_t	Size of the tumor tissue (cm)

$\overline{x}, \overline{y}, \overline{z},$	Injection location of MNPs in x, y, and z coordinate of tumor

Greek symbols

$\sigma_x, \sigma_y, \sigma_z$	Standard deviation of the MNPs spread in tumor
α	Correction factor
ρ	Density
η_b	Blood perfusion rate
Ω	Arrhenius thermal damage parameter
$\emptyset$	Solid volume fraction
χ_0	Static susceptibility
μ_0	Free space permeability
τ	Relaxation time
$\mathscr{K}$	Magnetic anisotropy

Subscript

a	Arterial blood
b	Blood
c	Body core
c	Combined
amb	Ambient air
CB	Core body surface
CS	Convective surface
t.t	Tumor tissue
ht	Healthy tissue

Abbreviations

AMF	Alternating magnetic field
TCIA	The Cancer Imaging Archive
NIC	National institute of cancer
CT	Computed tomographic
CD	Constant dose
MRI	Medical resonance imaging
DCE-MRI	Dynamic contrast-enhanced magnetic resonance imaging
DICOM	Digital Imaging and Communications in Medicine
STL	Stereo lithographic
ROI	Region of interest
CEM	Cumulative equivalent minutes
FEM	Finite element method
FVM	Finite volume method
MNPH	Magnetic nanoparticle hyperthermia
MTT	Minimum therapeutic temperature
MVS	Degree of microvascular stasis
MNP	Magnetic nanoparticles
SLP	Specific loss power
SAR	Specific absorption rate
RD	Reduced dose
HI	Heterogeneity index

CHAPTER 1

Introduction

1.1 General scenario

Cancer has become an epidemic in today's world. Cancer is the most significant cause of mortality globally, accounting for over 10 million deaths in 2020, or roughly one in every six [1]. It has been reported that the Asia continent and its countries are at higher risk of cancer according to a survey, 58.3 % of cancer-related mortality was reported only from Asia [2]. The most common cancers are breast, lung, colon, skin, rectum, and prostate. Among all types of cancer, breast cancer accounts for the maximum number of cases, and lung cancer accounts for the maximum number of deaths worldwide [1]. The statistical details of different types of cancer are compiled in the following section.

1.2 Cancer types and their status

There are 100 different types of cancer disorders that are categorized based on the type of cell mutations. Among these, some common types are carcinomas, sarcomas, leukemia, myelomas, etc, which originate from different cell types like epithelial, white blood cells, bone marrow, etc [3]. Cancer can affect different organs and tissues in the body, such as the breast, lungs, colon, skin, blood, bone, brain, etc. Various cancers manifest different symptoms, causes, risk factors, treatments, and prognoses [4].

Staging, which describes the extent to which the cancer has grown and spread at the time of

Table 1.1: Cancer status in different organs according to the Cancer Census 2020.[5]

Rank	Cancer	New cases in 2020	% of all cancers
	All cancers*	18,094,716	
1	Breast	2,261,419	12.5
2	Lung	2,206,771	12.2
3	Colorectal**	1,931,590	10.7
4	Prostate	1,414,259	7.8
5	Stomach	1,089,103	6.0
6	Liver	905,677	5.0

diagnosis, can be used to ascertain cancer status in various organs. Some of the cancers, which contribute more than 50 % of all cancers according to the Cancer Census 2020 are given in Table 1.1. Among all cancer types, 'Breast cancer' is the most commonly diagnosed cancer in women and the second leading cause of death worldwide [6]. Thus, in this work, breast tumor tissue has mainly been considered for the computational modeling of hyperthermia treatment. The following section describes some of the conventional cancer treatment methodologies.

1.2.1 Cancer therapeutic strategies/modalities.

Many new strategies and treatments have been evolving or are developing to cure, shrink, or prevent cancer progression. The choice of treatment depends on the type of cancer, the stage of cancer, and the goals of treatment methodology. The commonly used modalities for the battle against cancer are chemotherapy, radiation therapy, and surgery. Amongst these, chemotherapy is one of the most widely used cancer treatment methodologies. However, its advancement has been hampered by a variety of lethal side effects associated with the toxicity of common chemical medicines [7]. Developing tailored and localized medication or enhancement approaches might help to reduce the side effects by raising the therapeutic index of chemotherapy [8]. On the other hand, through technological advancement, radiation therapy (RT) is also routinely used for cancer treatment [9]. However, the development of radio resistance by cancer cells and the harm that RT-induced radiation causes to normal cells endanger the efficacy of radiotherapy. Surgery has also been utilized for reconstructive, supportive, and curative purposes. Surgery is successful for the treatment of early-stage cancer, in breast and colon cancer [10], as well as for a few cases in the advanced stage, like testicular cancer. There are other therapies, like immunotherapy, that aid the immune system in its battle against cancer. In this therapy, synthetic immune system proteins are administered orally, topically, intravenously, or via infusion, stimulating the immune system to function more effectively or intelligently against cancer cells. Conventional treatments like surgery, radiation therapy, and chemotherapy are still considered a preferred option to cure cancer. However, these conventional treatment methodologies for cancer are invasive and can have several harmful after-effects [11]–[13]. Therefore, the treatment methodology, which is minimally invasive and has fewer after-effects, has always been society's need. Several efforts have been made to develop such treatment methodologies for cancer treatment.

Hyperthermia is one such non-invasive or minimally invasive treatment therapy for cancer treatment. In this treatment, the body temperature is increased by 3 to 8 °C above normal body

temperature, i.e., 37 °C to kill the cancer cells. Usage of temperatures above this range results in cell necrosis, termed thermoablation. Hyperthermia can be applied as a standalone therapy or in conjunction with other conventional therapies. When applied in conjunction, hyperthermia enhances the therapeutic effects of radiation and chemotherapy [14]. Hyperthermia accelerates the inhibition of DNA repair when applied jointly with radiotherapy. This results in a hindrance to cancer cell proliferation [15]. Furthermore, for extreme hyperthermia or thermal ablation, the tissue temperature is generally raised above 60˚C to directly kill the tumor cells [16]. With new-age technologies, this therapy has brought new hope to cancer patients as a promising therapy among the alternative cancer-curing methods.

1.3 Hyperthermia

The word hyperthermia comes from two Greek words, 'hyper' and 'therme', which indicate "rise" and 'heat', respectively [17]. This condition is attributed to an increase in body temperature. William B. Coley [18] initially conducted experiments on inoperable tumors and observed that patients with high fever due to erysipelas, demonstrated spontaneous regression of tumors in some instances.

This brought forth the thermotherapy called hyperthermia, in which temperatures from 40 °C to 45 °C are used to treat tumors. Busch [19] and Kienle [20] also found that sarcoma disappeared due to a very high fever and suggested that cancer cells are susceptible to high temperatures. Maintaining the cells at a temperature between 41 °C and 46 °C for at least 20 minutes or up to 60 minutes causes direct damage to the cancer cell (varies in the literature) [21][22]. If the tissue temperature is maintained above 50 °C, it is termed coagulation, and if it remains between 60-90 °C, it is termed thermal ablation. In modern oncology, the temperature increment is artificially induced in a particular region of the body by some external heat source to kill tumor tissue or to sensitize it for another cancer treatment. Hyperthermia is induced by an external source, resulting in some adverse effects like blisters, burns, and discomfort. So, instead of exposing a large area or whole body to high temperatures, hyperthermia is now used locally to boost therapeutic efficiency.

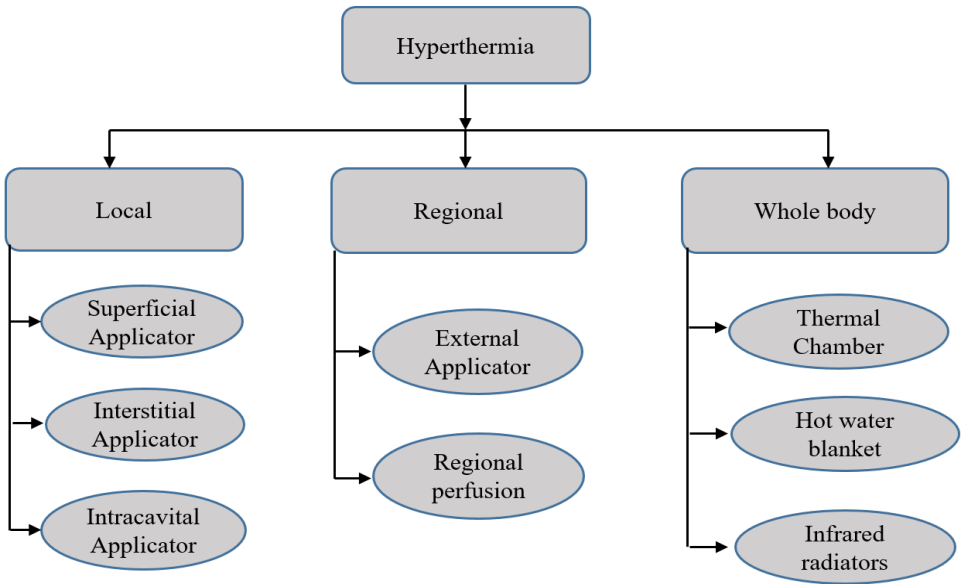

Figure 1.1: Types of hyperthermia and their respective clinical applicators.

There are three main types of hyperthermia methods employed, i.e., local, regional, and whole-body hyperthermia, as categorized in Figure 1.1. Several types of hyperthermia applicators that use different energy sources have been designed. Further details of these applicators have been summarized in the following section.

1.3.1 The different types of hyperthermia applicators

As categorized in Figure 1.1, the use of hyperthermia applicators depends upon the tumor location, its depth, and stage. The first one, i.e., local hyperthermia, is more dedicated to the small tumors (maximum 5-6 cm diameter) sited superficially or at an accessible location of the body [23]. The superficial tumors are clinically treated with different types of hyperthermia applicators. These consist of electromagnetic (EM) antennas, EM capacitive electrodes, ultrasonic transducers, and infrared heating systems. In general, these devices deposit energy to heat a limited volume of tissue close to the heating device. A brief introduction and summary of the operating principles of various systems for heating superficial tissue is in the next paragraph.

Electromagnetic (EM) antennas and electrodes use different waveguide structures, which operate in a range of 100-2000 MHz to generate the heating inside tissue termed as specific absorption rate (SAR) [24]. These EM applicators are designed in single and multi-element array configurations [25]. A water bolus is typically integrated into the applicator to control the surface temperature of the targeted tissue. These applicators have design flexibility (small or big size) as per the heating requirement but are limited to superficial tissue heating purposes.

The ultrasound (US) heating system works with ultrasound wave propagation at 2-20 MHz and focuses power into soft tissues to heat them. This therapy is suitable for small regions due to its narrow wavelength and is more directional than EM heating with minimal 'sidelobes'. It provides more precisely adjustable SAR with good penetration depth [26]. However, sound waves get absorbed in bones and initiate pain during treatment. The tiny microwave antenna array, laser fibers, RF electrodes, and US transducer applicators are generally employed in interstitial and intracavital hyperthermia. Among these, the interstitial applicators are inserted inside the tumor with an invasive procedure, and the intracavital applicators deliver heat through natural human body cavities like the rectum, urethra, esophagus, etc [23].

To heat the large parts of the body, regional hyperthermia (RH) is applied to the patients. The RH is applied using three main techniques, i.e., external applicators (for deep tumors), limb thermal perfusion, and continuous hyperthermic peritoneal perfusion (CHPP). The ring-shaped multi-element microwave antennas are being used for deep-seated tumors operating in 70-150 MHz frequency range. The tumor affecting arms, legs, lungs, liver, etc, can be treated with regional thermal perfusion in which the artery is bypassed and drained blood is heated externally. Sometimes, CHPP is also employed in conjunction with chemotherapy to enhance its efficacy in dealing with cancer in the abdominal cavities. If the patients have severe malignancy or tissue sarcoma, whole-body hyperthermia (WBH) is done instead of regional hyperthermia. The patient's body is dosed with anesthesia or sedation and is heated upto 42 °C for 1 hour or 41 °C for 3 to 4 hours [23]. As WBH offers the most homogenous heat distribution, but some complications are associated (thermal stress to the brain, lungs, liver, heart, etc.). Additionally, a novel cancer therapy employs heat treatment with magnetic nanoparticles. In this technique, iron oxide nanoparticles are injected into the tumor tissue and heated using a high-frequency magnetic field [27]. This offers a chance to heat tumors located in deep body areas, including the pelvis (prostate and cervical cancer) or skull (recurrent glioblastoma), resulting in controlled cell death [28]. This therapy offers better tumor targeting ability, ease in delivery of MNP, and subsequently, better temperature control inside the tumor region. Compared to the other therapies, magnetic nanoparticle hyperthermia (MNPH) is minimally invasive and effective in localized heating with fewer side effects. In addition, it can be applied in conjunction with other therapies, such as radiation and chemotherapy [27]. Current work is focused on the investigation of MNPH.

1.4 Magnetically induced hyperthermia.

Nanoparticles (NP) are being used in many biomedical applications, including magnetic bio-separation and detection of biological entities (cell, protein, nucleic acids, enzymes, bacteria, viruses, etc.), clinic diagnosis and therapy (such as MRI (magnetic resonance image), MNPH (magnetic nanoparticle hyperthermia) [29][30]. The MNPs (magnetic nanoparticles) suspended in fluid produce heat when exposed to an external alternating magnetic field (AMF). The heat generation by MNPs is mainly due to relaxation loss, hysteresis loss, and eddy current mechanisms [31].

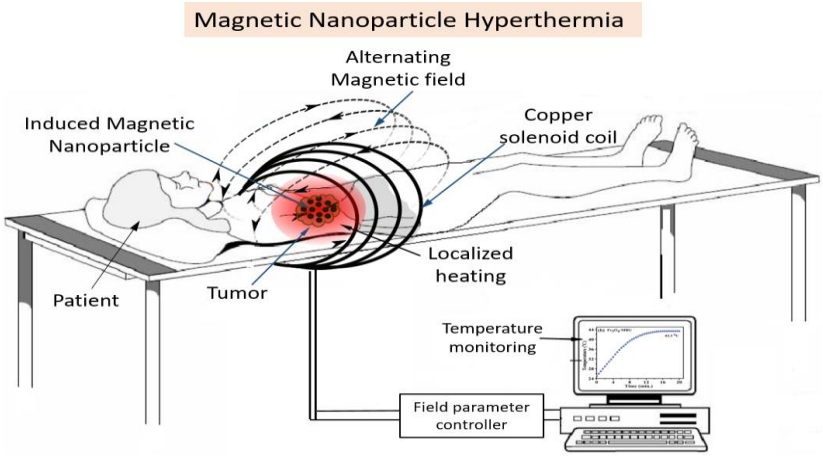

Figure 1.2. Schematic of magnetic nanoparticle hyperthermia applied as a standalone therapy.

The MNPs are generally injected/administered through the intravascular or directly into the tumor or targeted tissue. Subsequently, the MNPs are exposed to the external alternating magnetic field (AMF) to generate heat within the targeted tumor. This procedure leads to targeted and localized heat generation within the affected tissue, known as magnetic nanoparticle hyperthermia (MNPH) or magnetic nanofluid hyperthermia therapy (MNFHT), as shown in Figure 1.2.

1.4.1 Parameters influencing the heating efficiency of MNPs in hyperthermia.

The heat generation in the tissue with MNPH depends upon many parameters that include the magnetic and thermo-physical properties of MNPs, size and shape of the particles, distribution of MNPs in the tissue, magnetic field parameters (strength and frequency), and physiological structure of tumor tissue [32]–[34]. MNP material, shape, size, and magnetic properties are the key factors on which the heat generation by MNP depends. Therefore, nanoparticle synthesis

and devising adaptable physical and chemical properties for MNPH are key areas of research for MNPH. Mainly iron oxide nanoparticles and their ferrites like magnetite (Fe_2O_3), maghemite (γ-Fe_2O_3) are preferred for magnetic hyperthermia.

Table 1.2: Factors affecting the heating efficiency of MNPs in MNPH.

Parameters	Importance	Biological characteristics	References
Material of MNP	Ferromagnetic materials, especially iron and its ferrites in a 10 to 100 nm size range have excellent hyperthermia compatibility.	Ability to generate heat, Biocompatible, tunable morphology	[22][35]
Particle size	MNP in the superparamagnetic size (8-25 nm) range shows better heat induction.	Size with high infusibility optimum heat induction balance through relaxation losses is recommended for cellular uptake.	[36] [37]
Magnetization	Single-domain nano-size particles reflect high magnetization and heat generation.	Biocompatible material with high magnetization leads to less material intake to the tissue.	[38][39] [40]
Magnetic anisotropy	Less anisotropic MNPs have high induced heating.	This parameter quickly decides the best geometrical shape of the particle to be injected into the tissue.	[41][42]
Fluidic medium viscosity	It's a supporting medium that allows the MNP to inject and diffuse inside the tissue.	Cellular medium reduces the particle's magnetism to around half the water-based fluid value.	[43] [44]
Coating/Non-magnetic layer	It permits better dispersion, solubility, and colloidal stability by avoiding agglomeration of MNPs	Organic and inorganic materials are used to coat the MNP to have better biocompatibility.	[19][45]
MNP concentration	High deposition of MNPs at a site improves heating, but multi-site injection is preferred to reduce toxicity.	The particle concentration should be less than 4 mg/g of tissue to avoid acute toxicity.	[33][46] [47]
Particle distribution	MNP distribution and infusion rate have strong mutual dependencies. A controlled infusion leads to better spatial spread of MNPs in the tissue.	MNP spreads upto the tumor boundary by Gaussian distribution has a better heat rate than uniform spread.	[33][48] [49]
AMF amplitude and frequency	These key factors lead to heat induction when MNP-loaded tissue is exposed to AMF.	The combined effect ($f \times H_0$) exposure should be limited to 1.35×10^9 A/m. s.	[50][51]

These iron based MNPs offer the advantages of long-term chemical stability and biocompatibility, as well as ease of surface modification and functionalization. These factors affect the interaction of MNPs with biological tissue at the molecular level [52]. Surface functionalization plays a vital role in the synthesis of MNPs for MNPH to prevent aggregation of bare MNPs. The outer surface MNPs can be coated with different ligand materials, such as organic, inorganic polymeric, and non-polymeric surfactants [53]. These surfactants and ligands enhance the colloidal stability, cell viability, biocompatibility, and circulation of MNPs in the tissue as well as reduce the risk of blockage in blood capillaries [34]. The MNPs of high magnetization and superparamagnetic size range (8 to 25 nm) [36][37] always is a better choice to produce high specific loss power (SLP), i.e., the electromagnetic energy power generated per unit mass. Since magnetic hyperthermia typically utilizes smaller magnetic particles (less than 30 nm), the SLP generation happens through relaxation processes, specifically Neel and Brownian relaxation. It is noticed in the literature that the Rosenwieg model [32] for SLP calculation of MNP inside the biological media under a magnetic field is commonly utilized by researchers [54] [55]. On the other hand, experimental measurement of SLP by the calorimetric method (initial slope method) is also well documented in experimental studies of hyperthermia [56][50][57][58].

As discussed in this section, heat generation by magnetic nanoparticles under the action of high-frequency alternative magnetic depends upon many factors. The effect of each factor on the heat generation during MNPH is summarised in Table 1.2. It should be noted from this table that beyond the MNP properties, other factors like MNP fluid viscosity, ligand material, MNP concentration, and their spread inside the tissue also affect the SLP generation. The factors affecting heat generation during MNPH is summarised in Table 1.2.

1.5 Works on MNPH

1.5.1 MNP materials and SLP estimation for MNPH:

There are various parameters that have a significant impact on the amount of heat generation from MNPs during MNPH is discussed in the previous section. These are the material type, size, and concentration of MNPs, their spatial distribution and interactions with the tissue, and the strength and frequency of AMF [27]. The combined effects of these parameters affect heat generation and temperature profiles in tissue during the MNP-based hyperthermia therapy. The important parameters are MNP material and size, i.e., the material must have susceptibility to an external AMF. Commonly used MNP materials in MNPH applications are iron oxides and

their spinal ferrite of different chemical combinations with other magnetic materials [50] [59]. Different authors utilize different combinations of materials to make these ferrites more compatible to have the required magnetic properties, as shown in Table 1.3. These ferrites are expressed by $M(Fe_xO_y)$, where 'M' denotes the other metal cation (such as cobalt, manganese, Zinc, nickel, and Fe), and 'x' and 'y' are the valance variables. Prasad et al. [60] synthesized particles of manganese (Mn) as a metal cation and iron oxide as a base and proved them to be an excellent candidate for causing cell death in the *In Vitro* study. Similarly, Yoa et al. [61] developed Gd-substituted zinc ferrite with co-precipitation synthesis protocol with high heat generation and low cytotoxicity, details can be found in Table 1.3.

Table 1.3: MNP materials used in the *In Vitro* studies for MNPH.

Authors	Material	Synthesis method	Coating	Particle size (nm)	Hyperthermia parameters			Medium	Remarks
					Field strength,	Frequency, *f* (kHz)	SAR (W/g)		
Prasad et al. [60]	γ-$Mn_{0.2}Fe_{1.8}O_3$	Thermal decomposition	Acrypol	5-28	11.9	425	22.8	Hela cell	Cell death was noticed
Samanta et al. [62]	Fe_3O_4	Co precipitation	Bovine serum albumin (BSA)	28	6.3	400	36	Hela cell	BSA-coated MNPs show high thermal ablation, with no cytotoxicity observed
Yao et al. [61]	$ZnGd_{0.02}Fe_{1.98}O_4$	Co precipitation	PEG (poly-Ethylene glycol	20-30	6.5	60	-	Human vascular endothelial cells	High heat generation ability, as well as low cytotoxicity observed
Martin et al. [63]	γ-Fe_2O_3	Massart method	silica	5	15.9	100	-	A549 cells, HeLa cells, and HepG2 cells	Efficient cell uptake and biocompatibility with less interference with tissue morphology.
Le renard et al. [64]	γ-Fe_2O_3	Sol-gel	silica	5-10	9.54	141	20	Hydrogel	Excellent syringeability and superparamagnetic behavior

Ferrites are extensively studied because of their superior magnetic properties and higher biocompatibility in the cellular environment for hyperthermia application [22] [62] [63]. In the current hypothesis, three different spinal ferrites, i.e., manganese ferrite ($MnFe_2O_4$), cobalt ferrite ($CoFe_2O_4$), and magnetite (Fe_3O_4), have been considered to estimate MNP size-dependent SLP. It is notable that most of the studies do not consider the effect of MNP size variation on magnetic properties (magnetic anisotropy and magnetization) for SLP calculation [65] [56]. However, different authors in experimental studies have demonstrated the effect of particle size variation on magnetic anisotropy and domain magnetization [41][42] [66].

1.5.2 The studies on MNPH (experimental & theoretical).

The first case of MNPH was reported in 1957 when Gilchrist et al. used it to treat lymphatic metastasis [67]. Since the distribution of the concentration of MNP in the targeted tissue volume is an important factor for the heat dissipation during MNPH. Thus, various experimental as well as theoretical studies have been conducted to investigate the effects of the dispersion of MNP on the MNPH after its delivery to the targeted tissue. Salloum et al. [33] have shown that the dispersion pattern of MNPs after intratumoral injection mainly depends on the tissue structure and the infusion rate of MNPs. Based on the MNP dispersion pattern, SAR measurements were also conducted by the same group [33]. They found that the SAR distribution in the tissue is highly affected by the MNP distribution. SAR measurements revealed that the value of SAR is higher where the MNP concentration is higher.

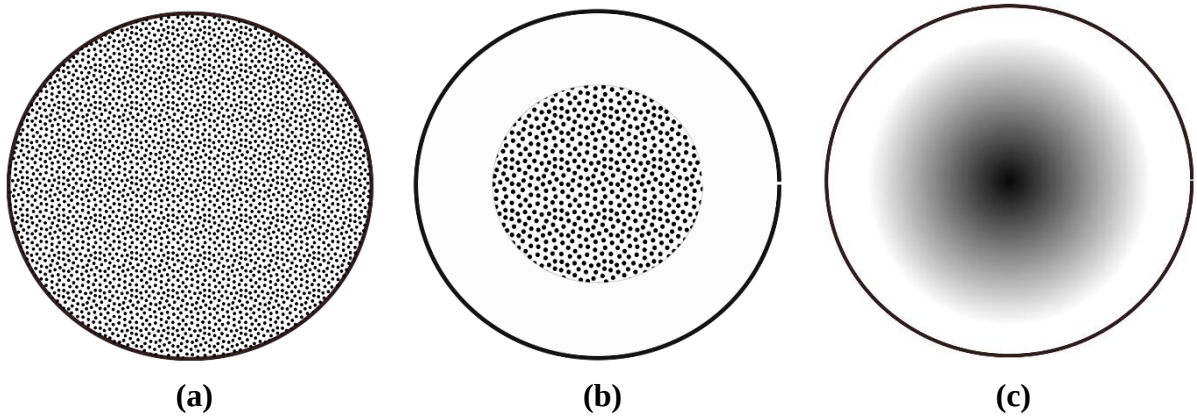

Figure 1.3. Schematic of the different nanoparticle distribution methodologies: (a) nanoparticles having uniform distribution, (b) concentrated distribution, and **(c)** Gaussian distribution.

The study conducted by Attaluri et al. [48] on prostatic tumors in mice found that redistribution of MNPs takes place during the heating, resulting in a greater spatial spread of MNPs. LeBrun

et al. [68] investigated that repeatable MNP dispersion patterns can be achieved by controlling the MNP infusion rate. They concluded that with a slow MNP infusion rate, a controllable MNP dispersion pattern could be achieved, whereas with a higher infusion rate, the nonuniformity in the MNP dispersion pattern increases.

Thus, based on the finding of the MNP distribution after its delivery to the targeted tissue, many theoretical studies also modeled the MNP distributions in the tissue for MNPH simulations. In most of the computational analyses, the MNP distributions are considered uniform or uniformly varying with respect to space [60] [69] [79]. Some of the commonly used MNP distributions in the tissue for MNPH study are shown in Figure 1.3. Figure 1.3 (a) represents uniform MNP distribution in the spherical tumor tissue. Figure 1.3 (b) represents MNP uniform MNP spread concentrated only in 40% of the tumor volume, Attaluri et al. [71]. Figure 1.3 (c) represents Gaussian (uniformly varying) distribution in tumor tissue. Furthermore, Kandala et al. [72] considered all three types of MNP distribution, i.e., Uniform distribution in the complete tumor, uniformly concentrated, and Gaussian distribution in tumor models, as shown in Figure 1.3. Among different MNP distribution methods, the Gaussian distribution is considered closer to the experimentally predicted MNP concentration for the soft tissue with a low MNP infusion rate [46]. However, in the experimental investigation (In-Vitro, In-Vivo), the MNP spread is not necessarily as per the theoretical description shown in Figure 1.3.

Table 1.4: Numerical studies for magnetic nanoparticle hyperthermia

Author	**Geometric model**	**Solution Method**	**Power Source term (Q_s)**	**MNP dose, distribution, and injection sites**	**Field parameters**		**Key point**
					H_0 (kA/m)	**f (kHz)**	
Kaiming Shen [73]	Spherical tissue	Finite element method @ COMSOL software	Rosensw-eig's model	1.9 mg/cm^3, uniform concentrated multipoint	8	100	Effective treatment tumor volume increases with a multi-point injection strategy.
Golneshan AA & Lahonian [49]	Concentric cylinders	Lattice Boltzmann model (LBM)	Gaussian SAR	NA, single site	15.9	300	LBM applied for the curved boundary.
Soetaert et al. [74]	Spherical tumor (dia=1.24cm)	LBM,	Experimental fitted SAR	5 mg/cm^3, Gaussian as per	4-94	150	The influence of amplitude modulation was tested for an

				experiment at a single site			inhomogeneous spread of MNPs.
M. Salloum et al. [75]	Irregular geometry	Derivative-free Nelder Mead Simplex method	Experimental Gaussian SAR	NA	45.51	434	Optimization algorithm for heating with multiple injections with the concept of T90, T50 and T10.
Giordano MA et al. [54]	Spherical shell tissue	Green's function solution equation	Rosensweig's model	105 mg/cm^3, uniform, single	6.5	500	Free-space Green's functions were developed for the bioheat differential operator.
Yundong Tang et al. [55]	Spherical tissue	Finite element method	Rosensweig's model	NA, Concentrated, multipoint	6.3	300	The effects of the number of intratumoral injections, injection doses and concentration were analyzed for efficacy.
Gurmeet et al. [76]	Cubical tissue	Finite volume method	Rosensweig's model	5 mg/cm^3, Gaussian, single as well as multipoint	10	100	Multi-site injection strategy performs better than single-site injection strategy

Attluri et al. [77] found that the shape of the ferrofluid spread inside the mice was quite irregular, even at the low infusion rate. A similar outcome was also observed by Hilger et al. [78] in the *In-Vivo* study, which found this irregular spread of magnetic material is caused by the high interstitial pressure in the tumor region [79]. The irregular MNP distribution leads to uneven temperature distribution and unwanted tissue thermal damage in the healthy tissue during MNPH. This heterogeneous heat generation in the tumor may lead to an inefficient therapeutic effect [80].

The spillover or diffusion of MNPs in healthy tissue may also result in their inadvertent heating. Thus, many strategies have been proposed to make MNP distribution in arbitrarily shaped tumor tissue more uniform [81][82]. Multi-injection strategy for MNP delivery has promising

results in producing more uniform temperature elevation in the targeted tissue domain [46] [73]. Boroon et al. used an inverse method-based algorithm to predict the number and location of injection sites required to obtain uniformity in tumor temperature profiles [46]. Salloum et al. [46] have devised an optimization algorithm to estimate optimum temperature profiles obtained with multi-site MNP injections in irregularly shaped tumors. Golneshan & Lahonian shows the effects of using multiple intratumoral injections instead of just one [46]. Singh et al. have reported that the thermal effects of MNPH can be enhanced with the use of multiple MNP injections [76]. They have shown that multiple injection sites result in a more uniform temperature profile within the tumor as compared to the single-site injection strategy. Similarly, Tang et al. [81] propose methods to optimize temperature distribution within tissues by considering MNP injection dose and injection site location. Results show that multiple intratumoral injection sites enhance the uniformity in MNP spread, thereby reducing the chances of heat spot formation. However, studies reveal that even for these multi-point injection strategies, MNP dose optimization has not been extensively investigated.

Furthermore, most of the theoretical (computational) studies discussed in the previous paragraphs considered simple tumor models. The details of some of the theoretical (theoretical and numerical investigations) [49][54] [74] [83] works are also illustrated in Table 1.4. It can be pointed out from these studies that most studies on MNPH consider regular geometric models in which cylindrical or spherical-shaped tumor geometries have been considered instead of real-shaped tumors. Research studies done by Tang et al. [82] and Dahagin et al.[84] consider the arbitrarily shaped tumors but limited to the computationally modified shaped geometries rather than real patient-specific tumors. Regarding realistic tumor models, there are limited computational studies that have been conducted based on the tumor models reconstructed from patient-specific DICOM images (Digital Imaging and Communications in Medicine) for MNPH [85], [86]. Few feasibility studies of microwave, RFA (radiofrequency wave), and ultrasound waves thermal therapies based on DICOM data have been reported [87], [88]. So further research is necessary to explore the feasibility of DICOM data usage to enhance the modelling accuracy in the MNPH application.

In MNPH, the rate of AMF induction heating largely depends upon the MNP mass or concentration inside the tumor region. From Table 1.5, it can be noted that different investigators have used different MNP doses ($\mathrm{mg/cm^3}$) or (mg/kg) of tumor tissue for their *In-vivo* investigation on MNPH. However, limited studies have been conducted on the optimal MNP dose ($\mathrm{mg/cm^3}$) or (mg/kg) of tumor tissue) required for standard clinical MNPH treatment.

Table 1.5: *In vivo* studies of biologically targeted magnetic hyperthermia.

Reference	Particle used	Hyperthermia parameters			Quantity of Fe delivered	Target	Summary of Results
		Field strength, H_0 (kA/m)	Frequency, f (kHz)	$H_0 \times f$ (A/m•s)			
Hilger et al. [89]	Magnetite MNP	1.2–6.5	400	4.8×10^8-2.6×10^9	28 mg/kg	breast tissue, and mice bearing human adeno-carcinomas	Tumor shrinkage after heating
Hilger et al. [78]	Magnetite particle	6.5	400	2.6×10^9	40-180 mg/kg	Human adeno-carcinomas in mice	Coagulation necrosis in treated tumor cells
Maier-Hauff et al. [90]	Aminosilane coated iron oxide	2.5–18	100	$2.5\text{-}18 \times 10^8$	50-150 mg/kg	Human brain tumor	It can be safely applied to glioblastoma multiform patients
DeNardo et al. [91]	Nanomag-D-Spio 20-nm iron oxide MNP	56-113	153	$8.5\text{-}17.2 \times 10^9$	150 mg/kg	Breast cancer cells in mice	Tumor growth delay
Huang et al.[92]	Magnetite MNP	38	980	37.2×10^9	5100 mg/kg	Squamous Cell Carcinoma	Durable ablation of tumors in 84% of hyperthermia group
Balivada et al. [93]	Fe/Fe_3O_4 nanoparticle	5	366	1.83×10^9	13.30 mg/kg	Breast cancer	Tumor size reduced after AMF exposure.

In Vivo studies done by Hlger et al. [89] [94] shed light on material dosage in breast tumor cells induced in the mice whose details are given in Table 1.4. Clinical trials done by Maier Hauff et al.[95], in which upto 31.36 $(\text{mg of Fe}/\text{cm}^3\ of\ tumor)$ of MNP is intrtumorally injected into gliblastoma patients. Similarly Huang et al. [92] used 5100 (mg/kg) in a mouse model which is around 100 times more than the approved recommended MNP dose, i.e., 510 mg/kg of tumor [50]. Balivada et al. [92] used 13.30 mg/kg of nanoparticle infused in the breast cancer cells and noticed significant suppression in tumor growth. So, in the *In Vivo* studies, including

first-phase clinical studies, there is an ambiguity in using MNP doses [89][92]. In general, as the MNPs are administered to the biological environment, it leads to some intracellular toxicity [50]. So, to achieve the desired heating and safe infusion of MNP with minimum toxicity of any form, the material dose needs to be optimized for specific tumors of different shapes and sizes.

It is noticed from the literature that tumor size-dependent MNP dose studies are rare in the theoretical as well as experimental hyperthermia. The vast majority of studies (numerical, *In Vivo,* and *In Vitro*) employ a constant MNP dose with respect to tumor size. So, more research is needed pertaining to the tumor size-dependent MNP dose for the optimum therapeutic efficacy of magnetic hyperthermia.

Apart from the MNP dose, distribution, and injection sites, the blood vessels and arteries in the vicinity of the tumor region also play an important role in the therapeutic outcome of MNPH. These arteries could work as a major heat sink during MNPH if they cross the tumor boundary. However, limited studies have been done to investigate the effects of major blood vessels on MNPH [96][97]. The effects of capillaries and blood vessels on MNPH have not been thoroughly investigated. So, the exact size and location of any artery or vessel near the heated zone need to be precisely identified. The CT-MRI images have been used to locate such structures in hyperthermia therapies to assess the post-treatment efficacy [96]. The present research has been extended to develop the DICOM data-based (of real patients) tumor models to analyze the therapeutic effects of MNPH. This extension includes the effect of blood flow through an artery partially engulfed in the tumor region while using multi-point injection sites for MNP distribution.

1.6 Research Gaps in the Literature

- The estimation of SLP is still associated with many assumptions, and further studies are required to reduce the error associated with the theoretical SPL estimation of MNP.
- Further studies are required to optimize the therapeutic effects of MNPH.
- Comparison of different MNP systems for MNPH applications is limited.
- Effects of environmental conditions (air velocity, humidity, etc.) on MNPH have not been investigated thoroughly.
- The effect of tumor position with respect to the skin during MNPH is not reported
- The existing computational investigations for MNPH are limited to the regular geometrical shapes of the tumor.

- There is scarce information on using DICOM data-based physical tumor modeling studies with MNPH.
- Limited studies have been done to optimize the MNP dose for a specific size and shape of the tumor.
- The effect of blood vessels in the vicinity of the tumor on MNPH has not been analyzed extensively.

1.7 Motivation and model of the study:

In the modern era, cancer or tumor has become the largest cause of mortality among all diseases due to its incurability to some extent. Conventional treatments, like surgery, radiation therapy, and chemotherapy, are invasiveness and have several harmful aftereffects. Therefore, society has always needed a minimally invasive treatment that doesn't have the side effects. One such minimally invasive or non-invasive cancer treatment method is hyperthermia. MNPH is one of the emerging cancer treatment hyperthermia methodologies. However, in magnetic nanoparticles hyperthermia (MNPH), the challenges of heterogeneous distribution of MNPs inside the tumor and an unequal distribution of heat distribution still exist. It is necessary to optimize additional factors, including AMF frequency, strength, and MNP dose, making it a topic for interdisciplinary research. Numerical simulation and experimentation are used to study both theoretical and practical aspects. The goal is to understand how parameters such as MNP distribution, tumor shape and size, and tumor vasculature affect homogeneous heat dispersion through simulation. The whole work could benefit the preclinical studies to select a potential MNP material, its dose (mg of MNP/tissue volume cm^3), and injection location for arbitrarily shaped tumors to have higher therapeutic efficacy during MNPH. The assumptions and simplifications associated with the mathematical model may be further reduced in future studies by incorporating more realistic thermo-physical properties of tumor tissue.

1.8 Research objective:

- Application of different MNP systems for optimum thermal therapy.
- To study the temperature evaluation by the different MNP distributions by numerical simulation.
- To investigate the therapeutic effects of different injection strategies.

- To investigate the effects of thermal dose, MNP distribution, and magnetic parameters on therapeutic efficacy using numerical and in-vitro studies.
- Experimental investigation of MNPs-based hyperthermia (thermotherapy).

1.9 Outline of work/ thesis organization.

Chapter 1: This chapter includes a brief description of cancer, its types, and its treatment methodologies. The heat-based cancer treatment methodology called hyperthermia and different hyperthermia applicators have also been briefly discussed in this chapter. A detailed description of magnetic nanoparticle hyperthermia (MNPH) is included in this chapter. The current PhD thesis is focused on the MNPH, thus a detailed literature survey on MNPH covering different aspects of this therapy is presented in this chapter. Through the literature survey, research gaps and objectives of the works have been established. The details of the investigated studies under this thesis is included in the next chapters.

Chapter 2: This chapter contains the details of modifications for the calculation of the heat generation by magnetic nanoparticles (MNP) during MNPH. A publication reporting the success in solving, modifying, validating, and applying the Rosensweig approach for three magnetic nanoparticle systems. The modification is in the form of correlations for magnetization (M_S) and the anisotropy energy based on the previously reported experimental data. This provides a more accurate prediction of specific loss power (SLP) dependence on the particle's size and its respective magnetization properties. On the other hand, an In-vitro agar gel-based experimental investigation was also performed to compare the experimental results with theoretical SLP calculations.

Chapter 3: In the second study, a 3D tumor model is considered to analyze the thermoregulatory response of skin and other ambient clinical conditions during magnetic nanoparticle hyperthermia (MNPH). In this work, the depth of the superficial tumor is changed with respect to the skin (top surface). Results show that a critical depth exists, which is nearly half of the tumor size, up to which the MNPH is influenced by the position of the tumor. Similarly, the effects of the ambient conditions during this thermotherapy on thermal dosimetry also cease beyond this critical depth.

Chapter 4: In the third study, the computational work is extended toward the realistic breast tumor tissue. Instead of hypothetical geometry, the physical tumor models are constructed from patient-specific DICOM images (Digital Imaging and Communications in Medicine) for

MNPH application. In this work, the effects of tumor shape and MNP injection strategies on the MNP dose (mg of MNP/tissue volume cm^3) have been investigated. The outcome shows that the MNP dose (mg/cm^3) should be reduced as the size of tumor volume (breast models) increases.

Chapter 5: Further, the fourth study includes the effect of blood flow through an artery partially engulfed in the tumor region on the MNPH. The tumor model, includes the artery, constructed using 3D slicer software from DICOM data. It aims to find the impact of blood flow on the amount of thermal dose required for an optimal therapeutic effect during hyperthermia. It is observed that the arterial blood carries immense heat during hyperthermia and leaves a significant percentage of undamaged tumor tissue.

Chapter 6: We summarize our results and suggest possibilities for future work.

CHAPTER 2

The SLP Estimation of the Nanoparticle Systems Through Analytical and Experimental Investigation

2.1 Introduction

In this chapter, the power dissipation of magnetic nanoparticles (MNPs) in the magnetic field is numerically as well as experimentally investigated. The major portion of this chapter is a theoretical investigation of SLP and the influence of the MNP's size-dependent magnetic properties on the induced dissipated heating power or specific loss power (SLP). Some experimental investigation of MNP heating inside the agar gel, along with validation with the computational simulation, is also reported in this chapter. As discussed in the introduction, heat generation by the MNP during MNPH depends upon the size and other material properties. The key parameters for MNP heating in MNPH are MNP properties, size, its materials, and magnetic field parameters (amplitude and frequency). Thus, the chapter includes theoretical investigations about the effects of these parameters on heat generation during MNPH.

The theoretical-based numerical investigation considers three different MNP systems ($MnFe_2O_4$, $CoFe_2O_4$, and Fe_3O_4) with an aim to develop a phenomenal model to understand the effect of MNP size distribution on their magnetic properties in magnetic hyperthermia performance. In the present study, in addition to the Fe_3O_4, we also used $MnFe_2O_4$ and $CoFe_2O_4$ nanoparticle, to understand how the magnetic properties of these three different nanoparticles affect their hyperthermia performance. Thus, in this work, we have tried to compare the heating efficiencies of these three systems, keeping the same particle size increase. Based on MNP size variations, how the magnetic properties of these particles get changed.

The focus of this work is to correctly predict two major size-dependent magnetic properties, i.e., magnetic anisotropy and saturation magnetization for SLP estimation. It should be noted that in most of the theoretical works, values of these properties are considered as constant for the estimation of SLP [65], [98]. The magnetic anisotropic energy and its types are influenced by many parameters. The primary factors, such as particle shape, size, surface, blocking temperature, etc., influence the magnitude of anisotropy energy. This effect is observed in experimental as well as theoretical studies [45], [66], [99]. Another key magnetic property, the saturation magnetization (M_s), is also highly influenced by MNP size. Thereafter, the size

dependent experimental data are used to develop empirical relations of these magnetic properties for the spherical shape MNP. Using M_s data from various experimental studies, fitting curves have been generated to develop the empirical relations for the considered MNP systems (materials). Along with this, the size-dependent empirical relations were compared with available analytical relations [100] for the magnetization parameter. For the calculation of specific loss power (SLP) of the considered nanoparticle systems these size-dependent magnetization (M_S) and the anisotropy energy are used.in SLP estimation model. This inclusion enhances the theoretical prediction of SLP for MNPH.

In the second portion of this chapter, an *In-vitro* investigation is carried out for MNP heat generation inside the agar gel phantom. This replicates the biological tissue for MNPH. Additionally, the experimental results have been compared with the numerical results. In the experimental work, magnetite (Fe_3O_4) magnetic particle-based MNP fluid is prepared and injected to the agar gel samples. Three samples of different MNP concentrations are prepared for experimental investigation. The heating values, i.e., SLP by exposure to an alternating magnetic field (AMF) for these samples, are examined by NAN201003 Magnetherm Applicator of Nanotherics company. Further, the physical geometric models of these agar gel samples have been developed in COMSOL software. The SLP results generated by the COMSOL software are compared with experimental results to verify the applicability of the numerical results for MNPH application.

2.2 Materials and Methods:

2.2.1 Heat calculation of the MNP under AMF:

The focus of the present study is to enhance the accuracy of the theoretical prediction in SLP heat generation by nanoparticle systems of $MnFe_2O_4$, $CoFe_2O_4$, and Fe_3O_4 for MNPH therapy. These materials can be been used for MNPH in the superparamagnetic size range. A ferromagnetic substance becomes magnetized when it interacts with a magnetic field because the direction of its magnetic moment vector aligns with the field direction. If the nature of the applied field is alternative, the same magnetism is induced inside the material, even if the material is at the nanoscale. As a result, a kind of vector movement gets started in every atom having an alternative nature, which generates heat inside the ferromagnetic material. Key parameters that have a significant impact on the amount of heat dissipation from MNPs are related to their intrinsic properties. Among these, the domain magnetization and magnetic anisotropy of MNPs are important and are influenced by the material type, size, and shape of

MNPs. The various factors affecting these parameters have been discussed in the following sections.

2.2.2 Induced mechanisms during the application of magnetic field to nanoparticles.

The amount of heat generated by ferromagnetic materials in the AC magnetic field depends on different magnetization mechanisms. These are eddy current, hysteresis, Néel and Brownian relaxation mechanism, and frictional losses in viscous media. Among these, the main attributed mechanisms for heat generation are hysteresis and relaxation losses induced in the magnetic materials. The hysteresis mechanism develops thermal energy due to the irreversible magnetization and shifting of the domain walls in multi-domain particles [101]. However, the hysteresis loss mechanism predominantly occurs when the size of MNP is 100 nm or above. [102][103]. For hyperthermia application (MNPH), the size of MNP is usually not chosen above 30 nm due to stability issues associated with bigger particles [104]. The heat generation by the MNP having a size less than 30 nm is primarily through Neel and Brownian relaxation mechanisms for single magnetic domain MNP [27]. These relaxation mechanisms dominate over each other depending upon the time period of relaxation.

The heat generation rate, Q_s ($\mathrm{W/m^3}$) by MNPs, as proposed by Rosensweig [31], for single domain MNPs, is given by Eq. (2.1) below:

$$Q_s = \mu_0 \, \pi \, \chi'' f \, H_0^2 = \pi \mu_0 \chi_0 H_0^2 \frac{2 \, \pi \, f \, \tau}{1 + (2 \, \pi \, f \, \tau)^2} \qquad 2.1$$

Where, μ_0 is the free space permeability, χ_0 is static susceptibility, H_0 and f is the magnetic field amplitude and frequency, respectively. The initial attempt time or relaxation time (τ) comprises two different times, τ_B and τ_N, the Neel and Brownian relaxation loss times, respectively, which depend upon the particle's magnetic core size and hydrodynamic size. The relations for these relaxation losses have been discussed by Rosensweig [31], which are expressed in Eqs. (2.2) to (2.4) as:

$$\frac{1}{\tau} = \frac{1}{\tau_B} + \frac{1}{\tau_N} \qquad (2.2)$$

$$\tau_B = \frac{3\eta V_H}{K_B T} \qquad (2.3)$$

$$\tau_N = \frac{\sqrt{\pi}}{2} \tau_0 \frac{exp\Gamma}{\sqrt{\Gamma}} \qquad (2.4)$$

where $\Gamma = k_{eff} . V_H/(K_B T)$, with k_{eff} as the anisotropy constant. V_H denotes the hydrodynamic particle volume, K_B is the Boltzmann's constant (J/K), η is the dynamic viscosity of fluid carrying MNPs, and T denotes the absolute temperature (K).

2.2.3 The effect of magnetic anisotropy energy (MAE) and blocking temperature of MNP on induction heating.

In the above expression $(k_{eff}.V_H)$ is known as the magnetic anisotropy energy (MAE), which is sensitive to the magnetic particle size. It is the energy barrier against the spontaneous moment reversal of particles from one direction to another. On the other hand, the term $K_B.T$ denotes the thermal energy that opposes the anisotropic magnetic energy in a magnetic material. This parameter is affected by the particle temperature, which decides the state of the magnetic particles, i.e. paramagnetic or superparamagnetic. The anisotropy energy value is influenced by the geometrical and structural properties [42] of the nanoparticle, which is given below in Eq. (2.5).

$$MAE = k_{eff}.Vol^m = E_{shape} + E_{surface} + E_{ME} + E_{MC} \qquad 2.5$$

where, E_{shape} is shape anisotropy, $E_{surface}$, is the anisotropy due to asymmetric surface, E_{ME} is magnetoelastic anisotropy due to external stresses and E_{MC} is the magneto-crystalline (cubic) anisotropy energy, which arises due to the coupling of the magnetization to the crystal lattice.

The shape of a nano-magnet considerably changes its magnetic properties, such as anisotropy, hysteresis, remanence, susceptibility, and coercivity. E_{shape} increases with the increase in the axial ratio of the geometry of the particle. Also, the area of the hysteresis loop increases due to this elongated shape as a result of enlarged magneto-mechanical torque [32]. However, for the symmetrically shaped nanoparticles, it's contribution to effective anisotropy gets minimized, hence becoming negligence for the spherical-shaped particle [100].

The surface magneto-crystalline anisotropy $(E_{surface})$ is induced in a magnetic material when its surface symmetry is disturbed, which affects the orbital motion of the electrons inside it. This anisotropy dominates only in nanoparticle systems with a high surface/volume ratio, such as ultrathin magnetic films or small nanoparticles [100].

The effect of stress is to introduce additional anisotropy called magnetoelastic (*ME*) in the magnetic material by changing its physical dimensions, which results in a change in its

magnetization orientation. This change in the direction of magnetization is due to the external field and temperature. So, applied stress on nanoscale magnetic particles changes the reversal characteristics of magnetization. However, the magnetoelastic (stress) anisotropy can be estimated as negligible because of the high Young's modulus of ferrites as for Co (150 GPa), Fe_2O_3 (208 GPa), and $MnFe_2O_4$ (121) discussed in different studies [105], [106], [107][31].

Lastly, the uniaxial magnetocrystalline anisotropy E_{MC} induces when the spin-orbital coupling is clubbed with crystal field interaction. Also, its magnitude depends upon the ratio of spin-orbital coupling and crystal field energy. So, for the spherical-shaped nanoparticles, the uniaxial or cubic (K_u) anisotropy has been found to be the major contributor in the calculation of effective anisotropy constant, i.e., K_{eff}. Therefore, its value for the spherical nanoparticle systems is evaluated from the stoner-Wohlfarth relation [100] given below in Eq. (2.6)

$$\mathrm{k_{eff}} = \frac{25K_B.T_B}{V_{NP}} \qquad 2.6$$

Where, K_B is the Boltzmann constant (1.38×10^{-23} J/K), T_B is the blocking temperature, and V_{NP}, is the volume of a nanoparticle. Furthermore, the anisotropy energy has a dependency on the temperature and particle diameter. The parameter blocking temperature is the threshold point at which the SLP and magnetic anisotropy values attain maximum. It is a temperature at which the magnetization vector rotates freely without an external magnetic field is termed as blocking temperature (T_B). This T_B generally depends on the particle diameter and other factors [108]. For the magnetic field value upto 100 Oe, the blocking temperature remains independent of the applied field, and beyond this value, it decreases as the magnetic field increases [109][36]. The blocking temperature of the nanoparticles decreases with increasing magnetic field strength. Also, the larger-sized magnetic particle is blocked at a higher temperature.

Table 2.1: The blocking temperature (K) variation with nanoparticle diameter extracted from experimental studies.

Size (nm)	Temperature (˚K)		
	$CoFe_2O_4$	$MnFe_2O_4$	Fe_3O_4
8	260	110	125
10	322	140	137
12	370	180	152
15	420	225	175
20	470	275	215
25	510	305	235
30	565	338	265

So, the blocking temperature increases with particle size at a particular magnetic field value. In this context, the values of this parameter (blocking temperature) have been extracted from the various experimental studies[109][36][110] [111] with different mean particle diameters for considered MNP systems, as shown in Table 2.1. The variation in MNP size in this study also has been limited to 30 nm. Since upto this size of MNP, it behaves as a single-domain nanoparticle system, and the power generation is dominated by Neel and Brownian relaxation phenomena only [112]. This effect of the particle size on the blocking temperature (Table 2.1) is used to calculate the anisotropy energy (K_{eff}) using Eq. 2.6 , and the output of this equation is plotted for different materials, as shown in Figure 2.1.

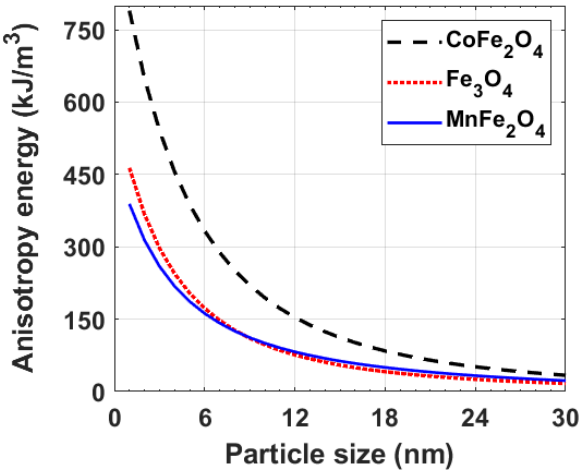

Figure 2.1. The magnetic anisotropy energy ($\mathbf{k_{eff}}$) as a function of the diameter of magnetic nanoparticles for different materials considered in the study.

It can be noted from Table 2.1 that the blocking temperature of the cobalt nanoparticle remains higher than that of the other two MNPs. Thus, its magnetic anisotropy value is also the highest among the materials considered (Figure 2.1). The value of anisotropy energy decreases as the nanoparticle diameter increases, which is also well documented in the experimental studies[35][42].

2.2.4 The effect of saturation magnetization of nanoparticles.

The susceptibility (χ_0) (Eq. 2.1), which is a function of magnetic field amplitude, can be determined from initial susceptibility (χ_i) with the help of the Langevin function as given in Eq. 2.7 below.

$$\chi_0 = \chi_i \frac{3}{\xi}\left(\cosh \xi - \frac{1}{\xi}\right) \qquad 2.7$$

The Langevin function equation is $M/M_{sat} = (\cosh\xi - 1/\xi)$ [37]. Where, M_{sat} is the saturation magnetization of ferrofluid and ξ is the Langevin function argument which is given by the following relation, $\xi = \mu_0 V_{NP} M_s H/K_B T$. In this relation M_s is the spontaneous or domain magnetization of the nanoparticle, and H is the magnetic field intensity. So, taking into account the above relations, the initial susceptibility (χ_i) can be derived as shown in Eq. 2.8.

$$\chi_i = \frac{M}{H} = \mu_0\, \phi\, \frac{M_s^2 V_{NP}}{3K_B T} \qquad 2.8$$

Where, $\phi = V_{MNP}/V_{sample}$ is the solid volume fraction for the dispersed nanoparticle having a volume (V_{MNP}) in matrix fluid of volume (V_{sample}) and M is the magnetization of the considered particle system. The susceptibility determined from the above relation as shown in Eq. 2.7, is used to calculate heat generation (Eq.2.1). Furthermore, the domain or saturation magnetization of a particular material is affected by the geometric as well as magnetic parameters of the applied field. However, the magnetization (M_S) of nanoparticle systems have a strong dependency on the size of the bulk material. There is enormous research related to the synthesis of magnetic nanoparticles demonstrating the variation in size and their effect on magnetic properties. Different authors in experimental studies have demonstrated the effect of particle size variation on magnetic anisotropy and magnetization [113][114][66][115][116] as given in Table 2.2. However, different materials behave in different ways in the variation of magnetic properties due to the variable shapes and sizes of the particles [32].

Most theoretical studies consider fixed values of domain magnetization for the calculation of SLP during hyperthermia applications. However, it is well demonstrated that saturation magnetization increases with increases in particle size [41] [66][117]. So, in this article, the critical relation between saturation magnetization and particle size is established using the experimental data reported by different studies. The estimation of M_S through the correlation curve established from the experimental data will enhance the accuracy of the estimation of SLP or heat generation calculations during magnetic hyperthermia for considered three nano materials. Table 2.2, enumerates the value of M_S at different sizes for three Nano-materials $MnFe_2O_4$, $CoFe_2O_4$, and Fe_3O_4 reported by different experimental studies. It should be noted from this table that different synthesis route induces different value magnetization (M_S) even on similar size of these nano materials. For the materials under consideration, i.e., $MnFe_2O_4$, $CoFe_2O_4$, and Fe_3O_4, the experimental values from Table 2.2 for M_S v/s particle size, have been plotted in Figure 2.2.

Table 2.2: The experimentally estimated values of saturation magnetization (M_S) considered in the current study.

Sr. no.	**Magnetic compound**	**Synthesis method**	**Size (nm)**	**M_S (emu/g)**	**References**
1	$MnFe_2O_4$	Co-precipitation	25	59.6	[38]
2	$MnFe_2O_4$	Reverse micelle	14	40	[118]
3	$MnFe_2O_4$	Polyol-mediated synthetic route	30	60	[119]
4	Mn Fe_2O_4	Co-precipitation	19	68	[57]
5	Mn Fe_2O_4	Co-precipitation	26	70	[120]
6	Mn Fe_2O_4	Emulsion and solvent	6 &18	50 &83	[121]
7	Mn Fe_2O_4	Electrochemical	20	75	[122]
8	Mn Fe_2O_4	Chemical oxidation	24, 14 & 13	65, 53 &, 45	[117]
9	Fe_3O_4	Co-precipitation	10.5	54	[57]
10	Fe_3O_4	Hydrothermal route	20	84	[123]
11	Fe_3O_4	Facile one-pot synthetic route	6.4	34	[124]
12	Fe_3O_4	Co-precipitation	12	92	[39]
13	Fe_3O_4	High-temperature hydrolysis	4.8	60	[125]
14	Fe_3O_4	Oxidation	22.4, 16.7 &, 15.4	81, 65 &, 53	[126]
15	$CoFe_2O_4$	Wet chemical	15-48	53-79	[115]
16	$CoFe_2O_4$	Non-aqueous solvothermal	4.5,6.4,11	36, 57, 79	[127]
17	$CoFe_2O_4$	Polyol method	5.5, 13.5, 13.9, 15.7	71.6, 70, 78.8, 70.4	[128]
18	$CoFe_2O_4$	High-temperature solution phase	6, 10, 15	55, 60, 64	[40]
19	$CoFe_2O_4$	Facile one-pot synthetic route	4.4	38	[124]
20	$CoFe_2O_4$	Co-precipitation	3.6, 5.3, 7	33, 37, 48	[129]

21	$CoFe_2O_4$	Chemical co-precipitation	10	57	[130]
22	$CoFe_2O_4$	Thermal decomposition	12, 16, 22	39, 52, 76	[111]

Using these data points, fitting curves (dotted curve) have been generated using the logarithmic fitting function, as shown in Figure 2.2 (a-c).

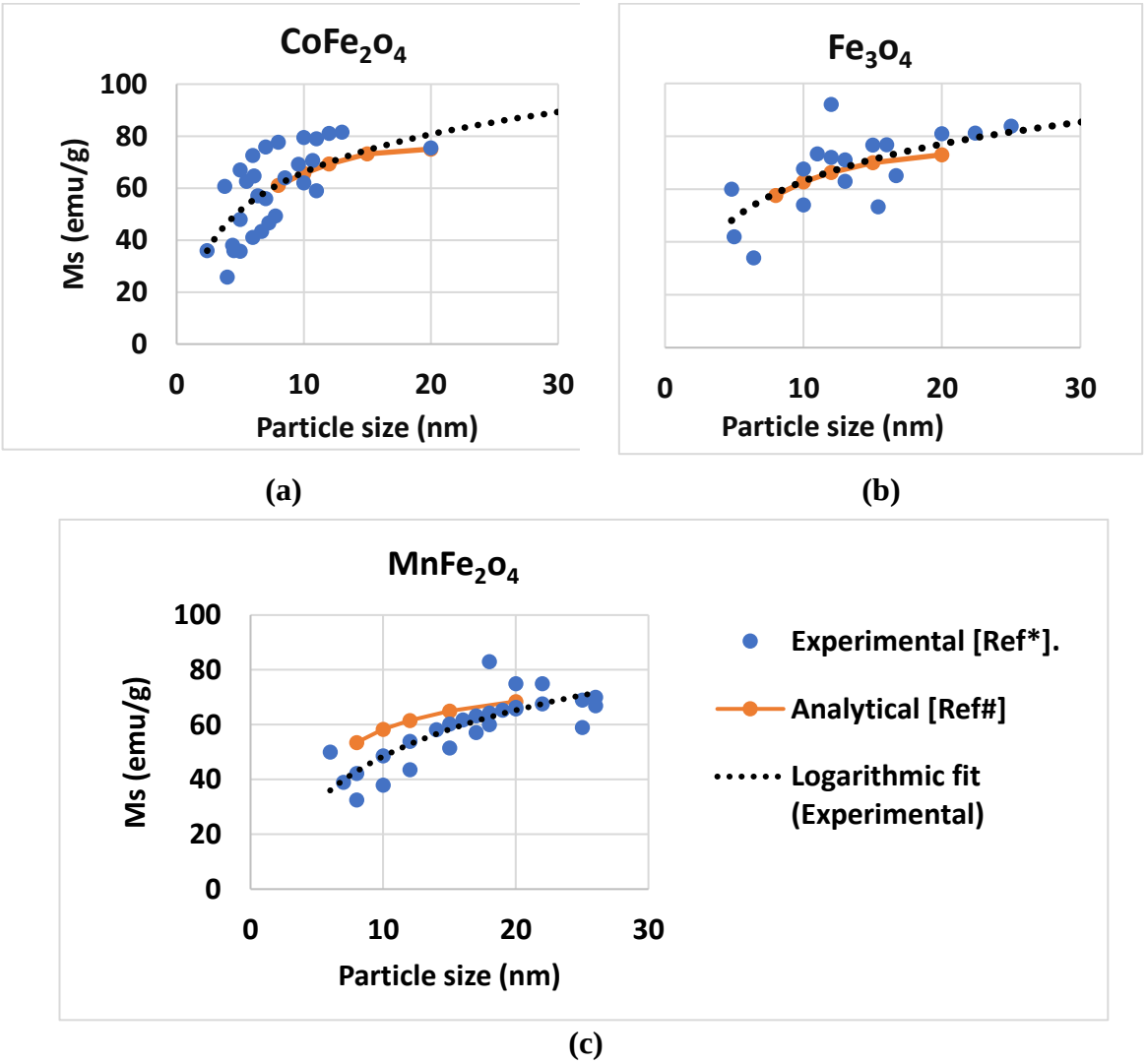

Figure 2.2. The saturation magnetization as a function of particle size from different experimental studies. Here in legend entry of Figure (c), the Ref*~ ([66],[40], [41], [57], [117], [119], [122], [123], [127], [129]), Ref# ~[41].

These curves predict the averaged-out value of domain magnetization (M_S) reported by different experimental studies for considered nanoparticle systems. These charts demonstrate how the experimental results are dispersed across a large range of M_S with particle size.

However, using these curves, averaging the value of M_S based on experimental findings generates a unique value of M_S at a specific size. In addition, a mathematical relation is given in Eq. 2.9 for the variation of M_S with respect to particle size, which has also been included in Figure 2.2.

$$M_S = M_S^{bulk} \times \left[1 - \left(\frac{NML}{D}\right)\right]^3 \qquad 2.9$$

where, M_S^{bulk} is the saturation magnetization of bulk materials, NML is the non-magnetic layer on nanoparticles, and D is the diameter of the particle. [100].

It is noticed that the fitted trend lines exhibit a good cohesion with the analytical curve atleast for cobalt and magnetite material, and a close relationship for Manganese ferrite MNPs, as shown in Figure 2.2. It is well known that the non-magnetic shell on the particle surface reduces the value of saturation magnetization and is called a dead layer. So, the thickness for this layer has been selected as 0.75 nm [100]. The bulk value for the saturation magnetization considered for the different materials are as follows, $M_S^{bulk} = 90, 80, and\ 86$ for cobalt, manganese, and magnetite respectively [131].

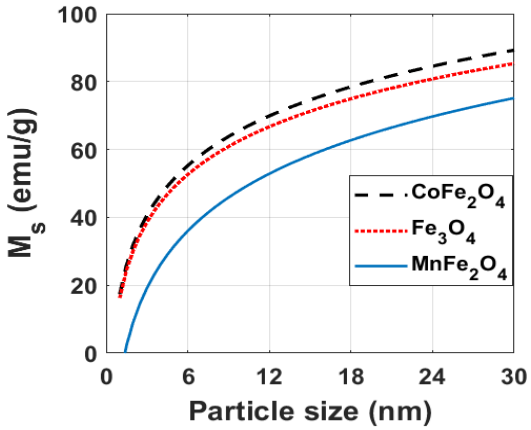

Figure 2.3. The saturation magnetization fitted with logarithmic curve fitting function as a function of particle size.

The correlations generated for ($MnFe_2O_4$, $CoFe_2O_4$, and Fe_3O_4) using experimental data for the M_S with respect to particle size are collected in Figure 2.3. It should be noted from these curves that for smaller nanoparticle sizes, the rate of change of the curve slope is quite high, i.e., the saturation magnetization increases rapidly with the increase in particle size. However, beyond the size of around 15 nm, the curves become asymptotic. Furthermore, the cobalt ferrites show

the highest magnetization, trailed by the magnetite particles, and the lowest values are for manganese ferrite nanoparticles.

2.3 Validation of the current protocol.

To establish the accuracy & validity of the correlation established in Figure 2.3, the heat generation using particle size-dependent saturation magnetization protocol is compared with the SLP values reported by some experimental studies. The calculation of SLP (W/g) from the power (Q_s) equation, is given as in Eq. 2.10:

$$SLP = \frac{Q_s}{\rho} \qquad 2.10$$

where, ρ (kg/m^3) is the mass density of the nanoparticle system. Q_s is the heat generation rate in W/m^3 by the MNPs. This, heat generation is experimentally measured by the calorimetric method using Eq. 2.11 [57][58].

$$SLP = C_p \frac{m_s}{m_{mnp}} \left(\frac{dT}{dt}\right) \qquad 2.11$$

where, C_p is the specific heat capacity of fluid in which MNPs are being suspended, for water = 4.186 J/(g.˚C), (*dT/dt*) is the slope of temperature versus time, m_s is the mass of suspension and m_{mnp} is the mass of magnetic material in the suspension. The physicochemical properties of the medium in which MNPs are present, such as viscosity, hydrophobicity, and dielectric constant, have an impact on the SLP or power generation. Here, water is considered as a suspension medium with a uniform distribution of magnetic nanoparticles and placed in an induction coil generating alternating magnetic field.

It should be noted that the value of SLP is calculated using a similar particle size, concentration, and AMF parameter (magnetic field amplitude and frequency) as reported in the experimental research in order to verify the validity of the current study. The results with particle size-dependent saturation magnetization (M_S) and anisotropy constant (K_{eff}) are in close agreement with the experimental values of SLP for considered nano-materials ($CoFe_2O_4$, Fe_3O_4, Mn Fe_2O_4) as shown in Figure 2.4 (a-c). However, the SLP value at a fixed (M_S) and (K_{eff}) shows large deviation from experimental values in the bar graph of Figure 2.4.

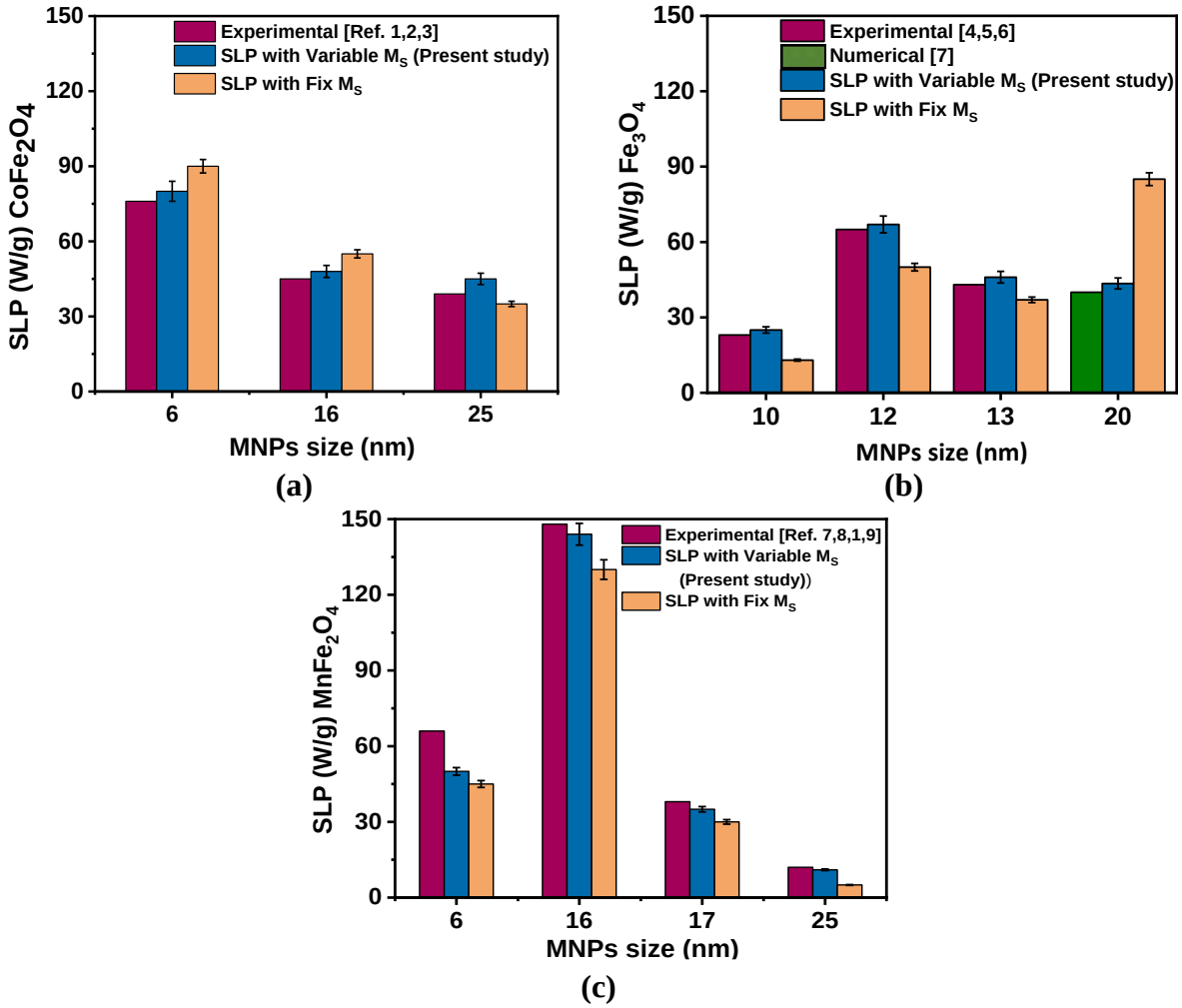

Figure 2.4. Comparison of Specific loss power estimated using variable $\boldsymbol{M_S}$ and fixed $\boldsymbol{M_S}$ with experimental studies, at different particle sizes. Figure (a) $CoFe_2O_4$, (Ref. 1,2,3 as [123][58][132]) (b) Fe_3O_4 (Ref. 4,5,6 as [133] [134] [123] [98]) (c) Mn Fe_2O_4 (Ref. 7,8,1,9 [[132][120] [130]]) MNP particle systems under the similar fluid suspension and magnetic parameters.

Consequently, it can be concluded that SLP predictions utilizing developed M_S correlation having good accuracy for a large range of particle sizes. The efforts to establish a relationship between M_S, K_{eff}, and the particle size reduces the error in the estimation of theoretical SLP predictions of ferrous nanoparticles for hyperthermia or other heating applications.

2.4 SLP calculation with different parametric values of AMF:

This section describes the SLP computation using the correlation developed in the previous section for a wide range of particle size and magnetic field parameters. The saturation magnetization and anisotropy energy values of the nanoparticle systems have a significant

impact on the heat produced by these systems. As discussed in the previous section, in most of the theoretical studies, authors consider a fixed value for these parameters for the calculation of SLP. However, particle magnetization and anisotropy are particle size and shape-dependent phenomena [116]. So, to minimize the error in SLP estimation, the present study incorporates the correlation developed in the current between magnetization & particle size. Using this parametric correlation, a study was done to analyze the effects of magnetic field parameters (Amplitude & frequency of AMF) and size on the SLP produced by the nanoparticle systems during their magnetic heating. The considered range of AMF parameters is within the safe limit of these parameters as prescribed for hyperthermia applications [50]. For efficient magnetic hyperthermia, a minimum dose of nano-material should induce sufficient therapeutic thermal dose in the targeted tissue volume. Usually, for the apoptosis of cancer cells, a minimum temperature of 43˚C should be achieved in the tissue during the therapy. Thus, heat generation during magnetic hyperthermia should be sufficient to achieve the required elevation with minimum amount of nanomaterials.

The heat generation (SLP) by MNPs depends upon magnetic field amplitudes and frequencies. With the increase in field frequency, the SLP generally increases up to a certain point for fixed amplitude. However, with the change in the amplitude, the heat generation MNP also changes. Thus, in the coming results, the effects of these parameters on SLP is reported. The size of nanoparticles is also altered during his parametric investigation. Again, the considered size is upto 30 nm. As explained earlier, heat generation occurs only through relaxation mechanisms for the considered size of MNP. The physical parameters for different materials used for calculation in the Rosenzweig heat generation model [31] are compiled in Table 2.3.

Table 2.3: Parameters used for the calculation of SLP for particle systems in the simulations.

Particle type	D (nm)	NML (nm)	ρ_{MNP} (kg/m^3)	$C_{p\,(MNP)}$ (J/(kg.K))	M_S (emu/g)	k_{eff} (kJ/m^3)
cobalt	0-30	0.5	5340	700	51-89	827-14
Magnetite	0-30	0.5	5180	670	48-85	463-5.5
Manganese	0-30	0.5	5240	800	15-75	388-5.3

Other parameters like μ_0, i.e., free space permeability is $4\pi\times10^{-7}$ T.m/A and η, the dynamic viscosity of fluid carrying MNPs is 0.001 N-s/m^2. ϕ is solid volume fraction based on the mass

of nanoparticles is similar to the experimental [132] and numerical studies [31] for all three materials.

2.4.1 Effect of variation in field frequency & particle size at fixed magnetic field amplitude

The heating power of the magnetic particles has a strong dependency on the applied magnetic field and frequency. The power or SLP is directly proportional to both of these parameters. However, a nanoparticle produces maximum heat/power at a particular size on a given frequency in an alternating magnetic field. And the condition on which the SLP $(P_S) = P_S(D, f)$ has its maximum value, i.e., $P_{S,max}$ is a resonant state for that particular particle size and magnetic field and frequency.

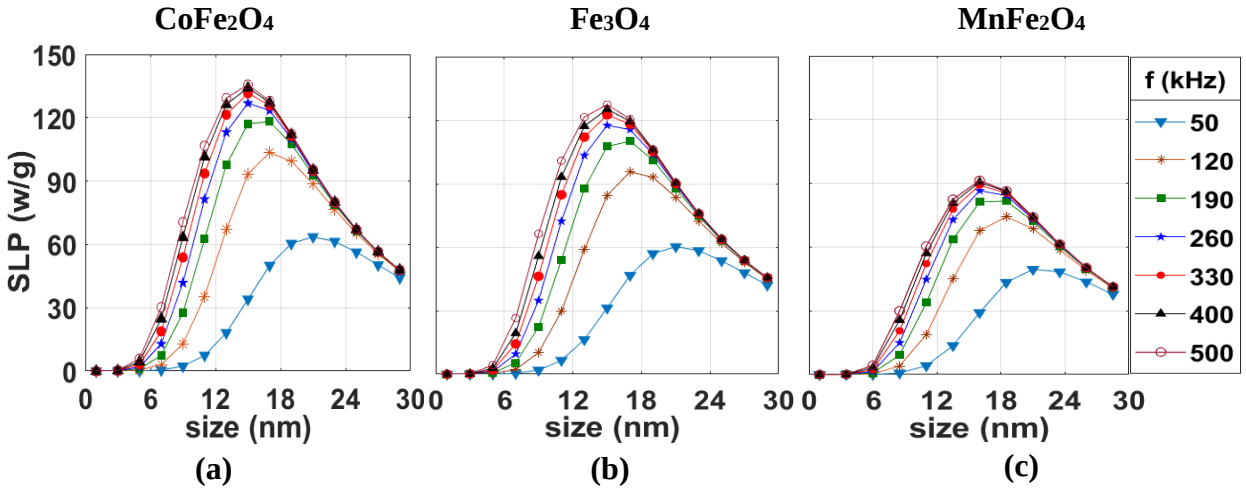

Figure 2.5. Dependence of dissipated power on particle size and magnetic field frequency (upto 500 kHz) at a field of 10 kA/m for all three considered particle system **(a)** $CoFe_2O_4$, **(b)** Fe_3O_4, and **(c)** $MnFe_2O_4$.

To observe this phenomenon, the frequency and particle size have been varied at a magnetic field amplitude of 10 kA/m. It can be noticed in Figure 2.5 (a-c) that every frequency curve (50-400 kHz) has a peak in its profile at a fixed particle size (D_O) for which a $P_{S,max}$ exist. Also, the curves synergistically follow each other and their respective D_O shift to smaller particle size as the frequency increases. For a frequency of 50 kHz, i.e., for the lower side first curve, the nano diameter (D_O) around 21 nm produces maximum SLP. And for a higher frequency of 500 kHz, the peak is around 14 nm. So, it can be concluded from these figures the D_O at which maximum SLP is calculated decreases with the field frequency increases. There is hardly any variation in heat generation for particle size below 4 nm and above 25 nm of size

as shown in Figure 2.5. (a-c), and the frequency curve converges at these limiting sizes of MNPs.

It should be noted from all the figures (Figure 2.5 (a-c)) that for different materials between the range of 4 nm to 25 nm, the SLP increases, attains a peak, and then decreases with the increase in the size of nanoparticles for all the frequencies. And this trend is similar in all the materials. With the increase in the field frequency, the SLP increases. However, the SLP particle size curves asymptotically close to each other after a frequency of 330kHz. The SLP curves are very close to each other for the last three values of frequencies i.e. 330kHz, 400kHz, and 500kHz for all the considered nano-materials. Thus, considering the frequency higher than 500 kHz will not enhance SLP at a field amplitude of 10kA/m. So, it can be concluded that for considered magnetic field parameters (amplitude & frequency) MNPs will produce maximum SLP at a fixed size of MNP. So, it is crucial to select a particular particle size and its respective frequency on which it delivers the maximum dissipated power before applying hyperthermia therapy.

2.4.2 Dependence of SLP on variable magnetic field with particle size distribution.

As discussed in the previous section, there is a saturation in SLP increment as the frequency increases, and beyond 500 kHz, a negligible change in SLP is noticed. So, keeping the frequency at that resonant constant value, i.e., at 400 kHz in Eq. 2.1, and making the SLP as a function of particle size and magnetic field, i.e., SLP (P_S)=$P_S(D, H_0)$, the variation in SLP has been analyzed in this section.

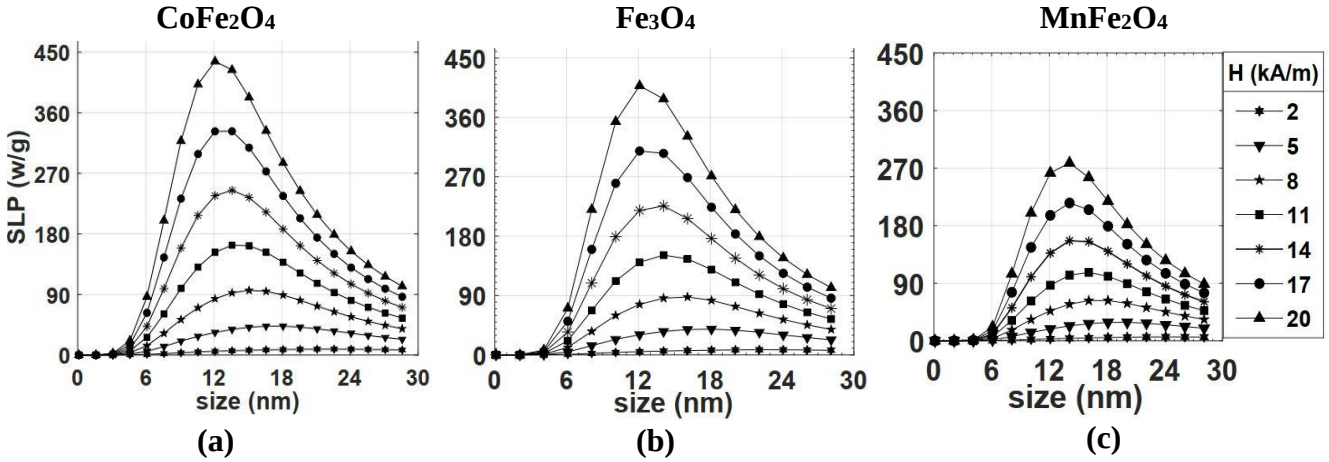

Figure 2.6. Dependence of dissipated power on the particle size distribution and magnetic field amplitude. Figures (a) (b), and (c) are plots of power dependency on variable fields upto 20 kA/m and at a field frequency of 500 kHz for $CoFe_2O_4$., Fe_3O_4, and $MnFe_2O_4$, respectively.

The maximum value of field amplitude considered for estimation of SLP is 20 kA/m. Like the effect of variable frequencies, the peak of every magnetic field curve shifts towards the lower particle size. Thus, an optimal value of particle size can be calculated for all the nano-materials from the maxima of the curves for different magnetic field values. Results show that the SLP increases with the increase in field amplitude Figure 2.6 (a-c) for all the considered materials. A significant difference in SLP (max) value is noticed for the particles of different materials under similar parameters of field variable particle size. It is interesting to note in Figure 2.6 that the maxima of SLP curves on the magnetic field versus particle size curves are shifting towards their smaller particle size. This size is considered the 'resonant' size of the MNP particles for that particular magnetic field value.

In addition, the same behavior of the peak shifting has been noticed for the frequency v/s size curves shown in Figure 2.5. So, to demonstrate this shift, the plot between 'resonant' size v/s variable amplitude and frequencies is shown in Figure 2.7 (a) and (b).

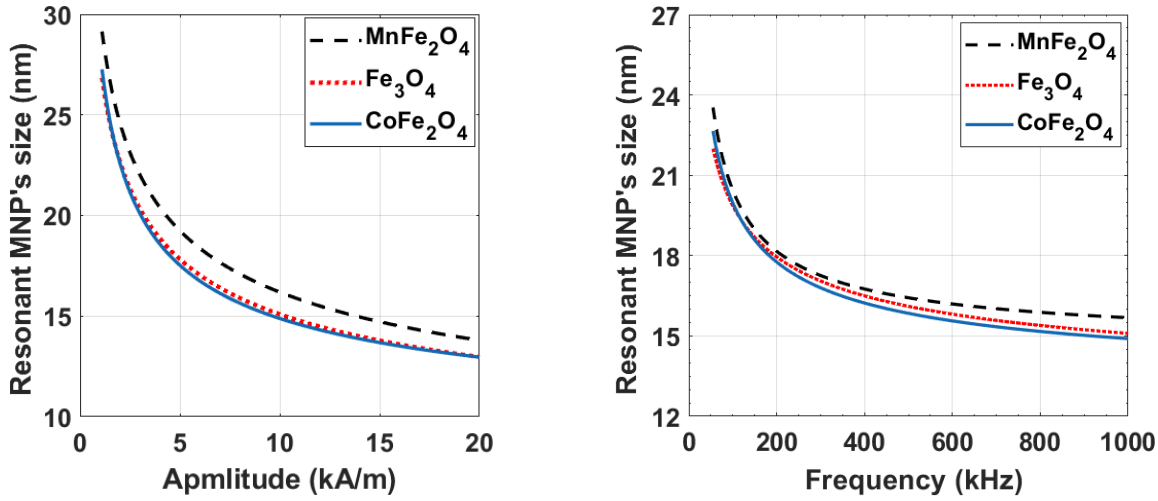

Figure 2.7. (a) Resonant particle size variation with the magnetic field at a frequency of 500 kHz **(b)** Resonant particles size variation with the magnetic field frequency at field amplitude of 10kA/m.

it should be noted from these curves that with the increase in the amplitude and frequency, the resonant particle size decreases. However, the resonant particle size for all three materials are of similar nature i.e., decreasing with the increase in amplitude and frequencies values at given specific conditions of exposure.

2.4.3 SLP values at resonant conditions for hyperthermia application

For the safe application of magnetic hyperthermia, there is a biological limit for maximum values of magnetic field parameters. This permissible limit is defined in terms of the multiplication of frequency & field amplitude ($f \times H_0$), and is recently addressed by Mag Force system tested on glioblastoma patients is 1.35×10^9 $\mathrm{A/m.s}$ [50]. However, S. Dutz and R. Hergt [135] have suggested this acceptable threshold limit ($f \times H_0$) to be upto 5×10^9 $\mathrm{A/m.s}$.

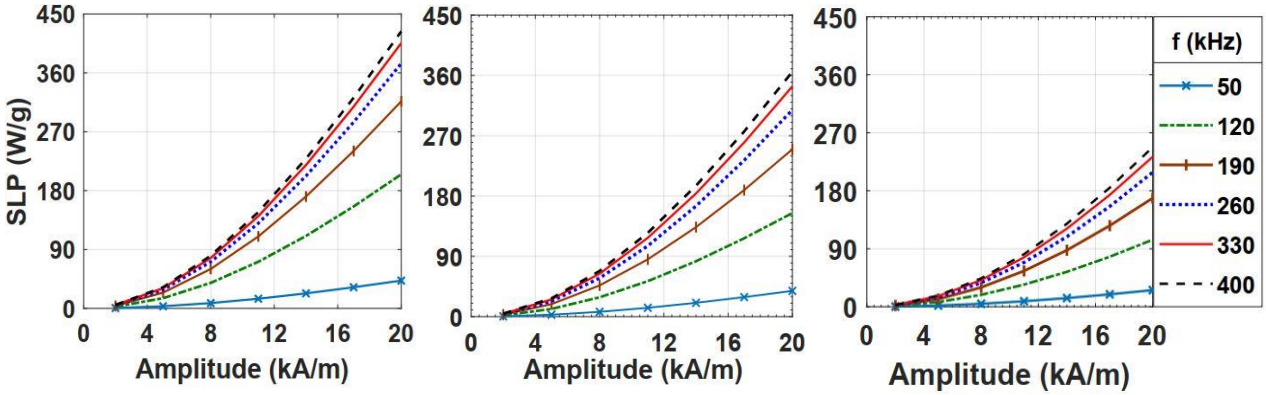

Figure 2.8. Specific heating power for a particle size of 12 nm while keeping the magnetic field and frequency as variables. Figures (a-c) show SLP for cobalt, magnetite, and manganese ferrite nanoparticles.

So, to obtain the maximum theoretical specific loss power, the considered value of field amplitude and frequency and their multiplication ($f \times H_0$) is under the permissible limit of AMF. The particle size of 12 nm is used to calculate SLP at different field amplitudes & frequencies. Figure 2.8 (a-c) shows the plots between SLP and amplitude at different frequencies for cobalt, magnetite, and manganese ferrite nanoparticles. So, by maintaining the field parameters exposer limit, SLP value for cobalt, magnetite, and manganese ferrite nanoparticles can be estimated from Figure 2.8. It is noticed from this figure that after a certain frequency, there is a saturation in SLP increment for a particular amplitude value. However, the heating continues to increase as the field amplitude increases at a particular frequency. So, for a specific particle size, the frequency can be fixed, and the amplitude can be varied as per the permissible biological limit in hyperthermia to gain a maximum specific heating power. Thus it is summarised that an appropriate choice of AMF parameters for a given MNP particle size can produce desired magnetic heat during hyperthermia therapy.

2.5 Experimental measurement of SLP for the MNP-induced agar gel phantom:

In this section, an experimental investigation as an *In Vitro* study is carried out to test the heating of nanoparticles inside the agar phantom for MNPH. The experiment in the current study is carried out using agar gel-based samples because their properties resemble to the tissue [136]. As agar gel has been considered as semisolid that contains a solid matrix and fluid (water) voids as exist in tissue [137]. The agar samples having colloids of MNP suspension have been heated using a hyperthermia applicator. The outcomes of this *In Vitro* study are also compared with numerical (computational) results, which increase the applicability of the simulated results for MNPH. So, this section briefly discusses the verification of the significant simulation results with experimental results of MNPH heating.

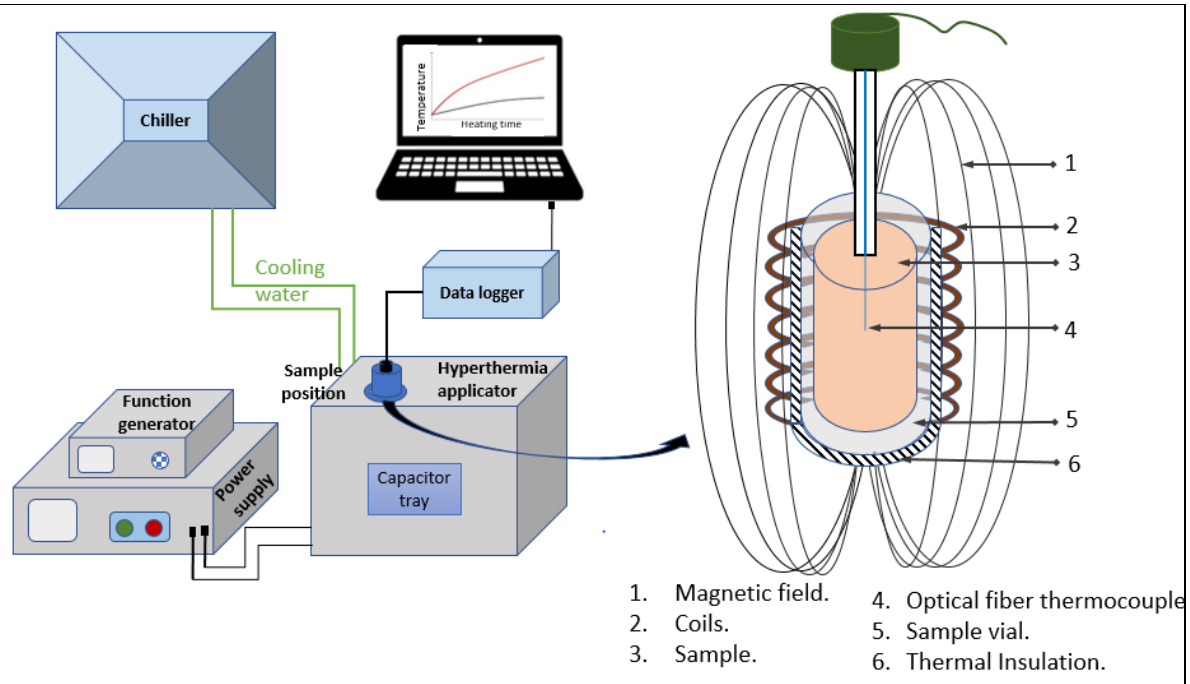

Figure. 2.9 Schematic diagram of the magnetic hyperthermia experimental setup for the magnetic heating and the temperature measurements of agar samples.

The experiments are conducted on a hyperthermia applicator (NAN201003 Magnetherm Applicator) of Nanotherics company (United Kingdom) having a water-cooled induction heating coil of 5 cm diameter. The arrangements of different components of the applicator are shown in the schematic diagram as shown in Figure 2.9. The highlighted portion of the sample position inside coil of the applicator has been shown on the right side of the Figure. 2.9.

In the experimental study, the cylindrical plastic vials (2 ml) of 1 cm diameter and 2 cm height to hold the gel samples are used. Three gel samples of volume 1.8, 1.6, and 1.4 ml (agar+water) are prepared with the agar concentration 0.5 g (agar powder)/ 100 ml (water). The samples were initially heated for 5 minutes in five repetitions in the microwave. The microwave operates at a power of 1.35 kW, which produces a flux intensity of 5 mW/cm^3, while operating at a frequency of 2.45 GHz. Different volumetric quantities of magnetic fluid (MF) having a concentration of 70 mg (MNP) / ml (water) are used to prepare the colloidal solution of samples (each 2 ml). This fluid contains magnetite (Fe_3O_4) nanoparticles of 8 nm particle size have a cubic shape with inverse spinel structures and were synthesized by the chemical co-precipitation method in our lab. Nanoparticles showed an 8 nm average size and were dispersed in water after a bilayer coating of oleic acid [138].

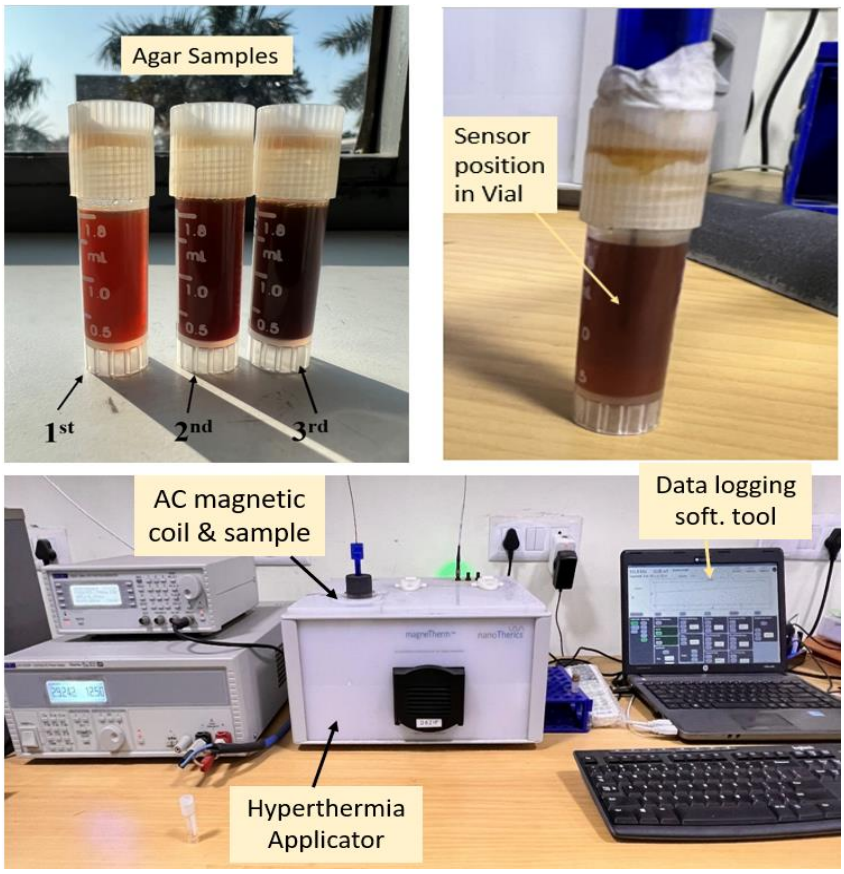

Figure 2.10. Agar gel samples and their heating with hyperthermia applicator (NAN201003 Magnetherm Applicator) along with the temperature monitoring using fiber-optics thermocouple.

The MNP fluid (0.2, 0.4, and 0.6 ml) was added to the agar samples during the liquid state to achieve a concentration of the three samples having concentrations of 7, 14, and 21 (mg of MNP)/(ml of gel) respectively as per the details given in Table 2.4. Then, the samples were homogenized in a water bath digital sonicator (LMUC-6) at a frequency of 40kHz and 150W power. This results in a uniform distribution of MNP in the agar solution. Colloids were allowed to solidify at room temperature, and MNP formed a colloidal suspension in an agar solution. Heating of samples were done with 935 kHz field frequency at a magnetic field strength of 10 mT using the hyperthermia applicator is shown in the Figure 2.10.

The vials were placed inside the magnetic coil in an engulfing cavity made of asbestos material to replicate the adiabatic boundary conditions. The outcome of heating in the form of time-temperature plots (blue dotted lines) has been observed for the considered samples as in Figure 2.11. The temperature profile of the center point (longitudinal and *x*-sectional) positioned inside the vial has been examined. It can be noted from Figure 2.11 that as the nanoparticle concentration in agar gel increases, more heat is produced, which is reflected in the temperature increment rate. Thus, gel with higher concentration achieves higher temperature elevation compared to gel with low MNP concentration.

In the experiment, the calculations for SLP from the MNP-gel samples were done using the initial slope method as given by the empirical relation given by Eq. 2.11. Other researchers are also using this method for the SLP calculation [1][2]. In this method, the temperature-time slope of the heating curve for initial 100 seconds, is linearly fitted to get the initial slope [139]. So, in the current study, the temperature-time slope for the first 100 seconds is used to calculate the SLP of MNP in different samples, the details of which are given in Table 2.4.

Further, the SLP calculations using the **Box-Lucas model** [3] has been added to compare the calculated SLP with the initial slope method. This model is based on the energy equation balanced for heat loss and gain during hyperthermia heating of the magnetic nanoparticle [4]. The formula used in this model, which is equivalent to the initial slope method, is given by the Eq. (2.12):

$$SLP = \frac{\rho}{x} C_p \Delta\theta_s \, k \qquad 2.12$$

Where, ρ is the density of the suspension media, which is 1 g/mL. x is the MNP concentration in the sample in mg/mL. The $\Delta\theta_s, and\ k$ are the constants, whose values have been extracted from $\Delta\theta$ Eq. (2.13) by curve fitting the temperature-time profile of heating using the box-Lucas model.

$$\Delta\theta = \Delta\theta_s(1 - e^{(k.t)} \qquad 2.13$$

The calculated SLP value from Box-Lucas model was found to be close to the SLP value calculated using the initial slope method, which can be found in the Table 2.4.

Table 2.4: Details of the sample prepared for MNPH.

Sample	MNP fluid (ml)	Gel+water (ml)	MNP Concentration (mg/ml)	SLP (W/g)	
				Initial-slope method	Box-Lucas model
1st	0.2	1.8	7	2.1	1.98
2nd	0.4	1.6	14	2.5	2.4
3rd	0.6	1.4	21	3.5	3.75

Furthermore, to correlate the temperature evolution through experimental analysis, simulations have been performed in the COMSOL software on the similar dimension geometric model of the vial for hyperthermia conditions. In addition, the same adiabatic thermal boundary conditions have been applied to the model for simulation. The heat source (Q_s) for the bioheat transfer in the vial model is calculated from the SLP obtained with initial slope method from the experimental study (Table 2.4).

Further, these time-temperature profiles of different MNP concentration samples have been plotted against the experimentally observed temperature profiles. It is noticed that the temperature profiles obtained from experimental as well as computaional are in good agreement and follow each other.

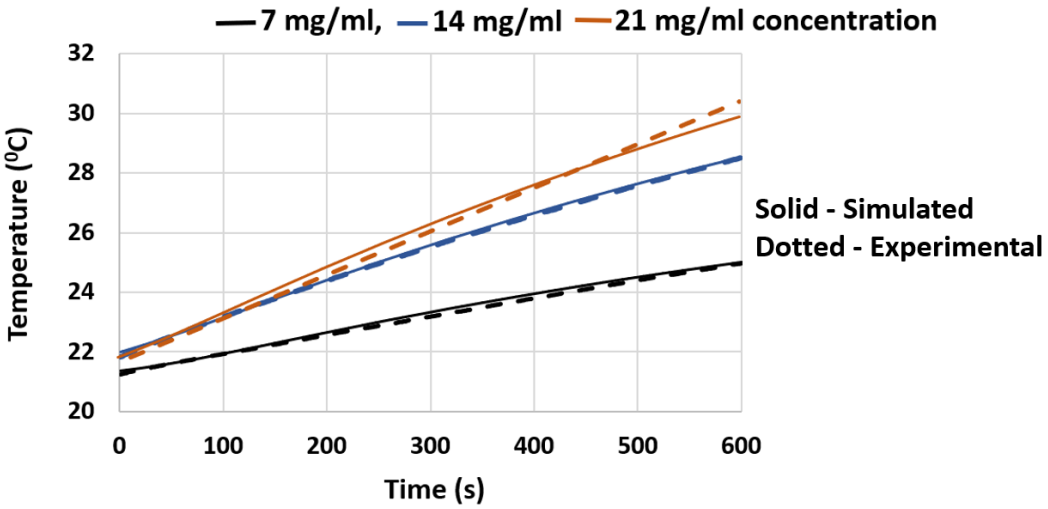

Figure 2.11. Comparison between the simulated and the experimental temperature profile for agar gel phantom with different MNP concentration.

The temperature has been obtained for the corresponding center point 'C' (as in the experiment), as shown in Figure 2.12. for the simulation.

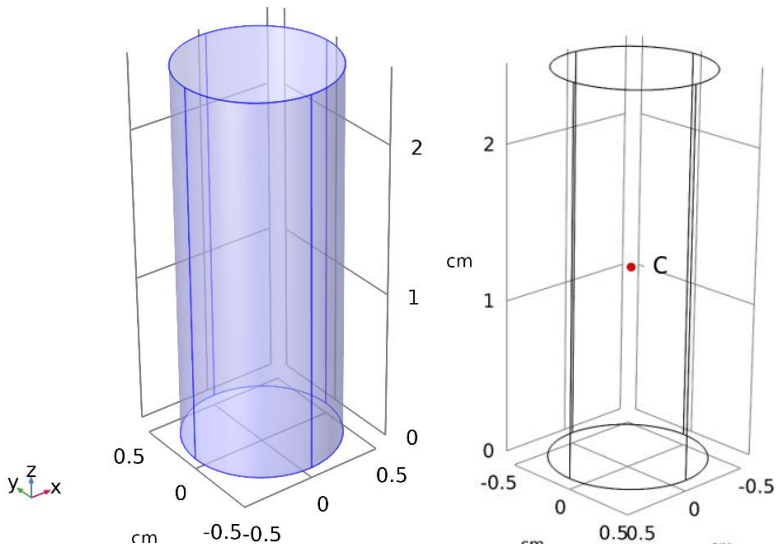

Figure 2.12. Vial as a geometry model formed for simulation in COMSOL

However, there are some differences in temperature profiles between these two protocols, as shown in Fig. 2.11 above. This is because of certain assumptions (isotropic tissue properties) applied to the bioheat model and the differences in the physiology of the agar phantom and the simulated model. Thus, the considered bio-heat model for the MNPH applications can be successfully applied to investigate and optimize different parameters of magnetic hyperthermia therapy. Though this In-Vitro application of magnetic hyperthermia has been successfully implemented in the current study.

There were some challenges we came across while executing the experiments. In brief, here is a list of the challenges pertaining to sample preparations and magnetic heating in MNPH:

- **Preparations of colloids**: Precisely controlling the concentration of nanoparticles, size, and their size distribution during the synthesis and subsequent dispersion in agar gel was difficult.
- **Synthesis of tailored MNPs**: For successful magnetic hyperthermia experiments, synthesis of MNP with desired magnetic properties, size, and size distribution are essential.
- **Optimum Field and Resonant Frequency**: Determining the resonant frequency with reference to MNP size that maximizes the effectiveness of Magnetic Fluid Hyperthermia within the safe limit of exposure to alternating magnetic field (AMF).
- **Thermal boundary conditions in samples**: Applying adiabatic boundary conditions to the gel samples is important to reach the steady state conditions while heating.
- **Thermometry measurement**: for successful magnetic hyperthermia experiments, monitoring of the temperature at multiple locations within the sample is required. This is employed with the fiber optics-based temperature sensor in the magnetic heating of the sample to measure the temperature.

2.6 Conclusion

The quantification and measurement of specific loss power in magnetic heating are usually done through theoretical and experimental methods. There is always an association of errors due to the approximations & assumptions in the empirical and analytical estimation of SLP during magnetic heating of nanoparticles. Thus, in this work, instead of including a fixed value of domain magnetization and anisotropy energy in the calculation of SLP, their particle size-dependency is incorporated in the analytical calculation of heat generation by MNPs ($CoFe_2O_4$, Fe_3O_4, and $MnFe_2O_4$). The anticipated SLPs are more accurate when MNP particle size-dependent magnetic characteristics are considered. The size-dependent saturation magnetization for cobalt, magnetite, and manganese ferrite nanoparticles correlation is developed using experimental results. The developed correlations & estimation of SLP of the considered material are expected to be advantageous for future theoretical as well as experimental studies of magnetic hyperthermia. On the other hand, *In Vitro* studies also build confidence levels of the simulation results for MNPH.

CHAPTER 3

Evaluation of Therapeutic Effects Due to Variation in the Position and Ambient Conditions on Superficial Tumor

3.1 Introduction

The numerical quantification and measurement of specific loss power (SLP) of different MNP systems in magnetic heating has been done in the previous chapter. The comparison of the computational results with experimental results reflects the applicability of the MNPH simulation for the analysis and the optimization of the parameters for magnetic hyperthermia. Thus, in this chapter MNPH is simulated in a three-dimensional (3D) tumor model. A qualitative analysis of the position of the tumor tissue beneath the body's outer skin is addressed for effective magnetic thermotherapy. In general, the tumor cells grow at randomized locations in any part of the human body. In cases of skin, lung, and breast cancers, the tumor cells grow beneath the skin surface and even sometimes these cells generate on the outer skin surface itself. The location of the tumor from the skin as well as ambient condition (and temperature and velocity) also play a crucial role in thermotherapy [140] [141]. Additionally, the environmental ambient temperature also affects the thermoregulation of human skin temperature [142]. Consequently, the variation in the heat transfer rate from the skin takes place. Moreover, various factors of the ambient conditions like relative humidity, airflow velocity, temperature variation, and other spatial inhomogeneity have considerable effects on the heat transfer from the human body [143].

In this chapter, the simulations are performed to elucidate the effects of tumor position and clinical environmental conditions (temperature, velocity of ambient air) on the therapeutic effects of magnetic nanoparticle hyperthermia (MNPH) in superficial tumor like breast tumor tissue. The position of the tumor tissue (of size 1.5 cm) within the 3D model as well as the heat transfer rate through the skin is altered to evaluate their effects on MNPH. Six different positions of tumor ranging from zero-depth to the tumor depth of 1.5 times the tumor size from the skin are considered. Similarly, three different heat transfer coefficients (h_c = 2.5, 5.5, 7.5 $\mathrm{W/m^2K}$) on the skin during thermotherapy are considered to simulate a wide range of clinical environmental conditions. The skin thermal responses are based on the in-vitro experimental work reported by Kurazumi et.al.[144] for natural convection of heat transfer under different ambient conditions as well as posturing conditions.

3.2 Physical tumor modal

A 3D tumor tissue surrounded by the healthy tissue as shown in Figure 3.1 is considered for investigations.

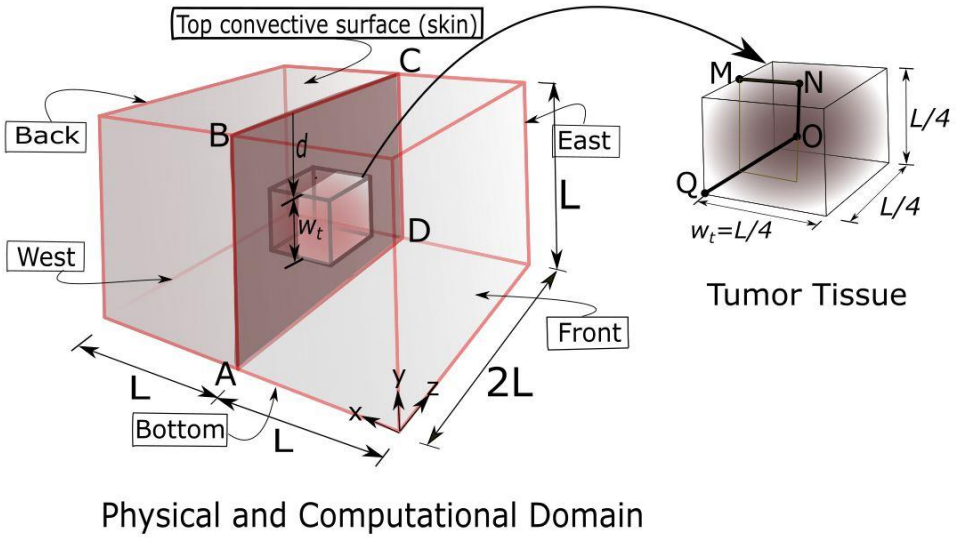

Figure 3.1: Schematic of the 3D physical model comprising the tumor and surrounding healthy tissues with the top convective surface (skin).

In this model, tumor tissue of cubical shape is embedded inside the healthy tissue. Though in most of the computational models, tumors are considered as spherical, spheroidal (elliptical) & irregular [145] [74], however, cubical-shaped tumors being simple & symmetric similar to a spherical, spheroidal-shaped tumor, still contains some features of tumor irregularity. These irregularities in shape are due the fact that the faces & corners of cubes having different distances from the centroid [76]. Another reason to select a simple tumor shape is due to this work is mainly devoted to estimate the effects of tumor location & skin environmental effects on MNPH therapeutic protocol instead of its shape effects. Though, the skin and deep tissues have a distinct physiological structure with their respective metabolic heat generation rate. However, the variation in the temperature gradient in the layers remains almost linear to maintain the core body temperature [146]. Thus, for simplification, tumor tissue is surrounded with homogeneous healthy tissue in the considered tumor model. As the breast's major portion constitutes mammary gland lobes, and 70-80 % of breast cancer develops in the mammary gland (ductal carcinoma and lobular carcinoma) [147]. So, the gland's physical parameters have been considered for healthy tissue properties in this work.

The size of the tumor model including the healthy tissue is of length L (6 cm) in the vertical (*y*) direction and '2L' in the horizontal (*x* and *z*) directions. The top convective surface (skin) of the model is exposed to ambient environmental conditions. The size of the tumor (cubical shape) is w_t = 1.5 cm (L/4) as shown in Figure 3.1. This size of tumor falls within the T1 Category of tumor (American Cancer Society) [147].

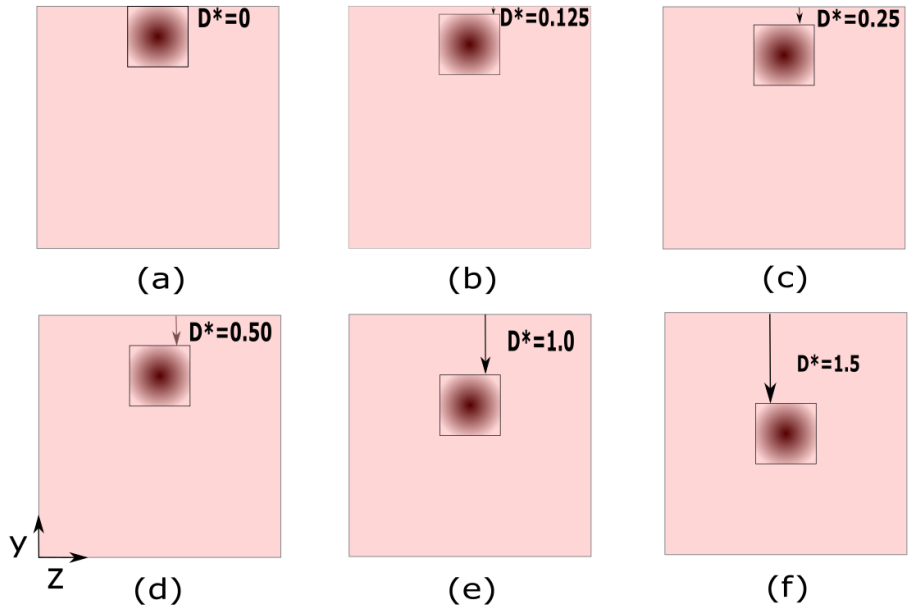

Figure 3.2: Tumor tissue positions from the top surface (skin) on plane ABCD. **(a)** tumor position at D*= **0, (b)** tumor position at D*= **0.125, (c)** tumor position at D*= **0.25, (d)** tumor position at D*= **0.5, (e)** tumor position at D*= **1.0,** and **(f)** tumor position at D*= **1.5**.

A parameter called tumor depth-size ratio as 'D*' (D* = d/w_t.) is used to describe the tumor position with respect to the skin (top convective surface). Where *d* is the depth of tumor from the skin surface and w_t is the tumor size, (Figure 3.2). Tumor tissue beneath the outer skin is centrally located with respect to the reference *x*-*z* plane. However, its position is altered in the vertical (*y*) direction by changing the depth 'D*' as shown in Figure 3.2 in a 2D plane passes through ABCD (Figure 3.1). Six different positions of D* for tumors, ranging from 0 to 1.5 with respect to the skin are considered (Figure 3.2). It should be noted from Figure 3.2 that, when D* is equal to zero, the tumor's top surface coincides with the skin surface. With the increase of D*, the position of the tumor incrementally moves downwards, towards the body core. The maximum tumor depth is considered as D*=1.5 (tumor center at 3 cm from top surface) in this study. This is to ascertain the association between tumor size and its depth for superficial tumor considered here. Generally, tumors are dichotomized at a distance of 5cm from the skin to feature as a superficial or deep-seated tumor [148].

During the therapeutic application of a MNPH applicator, heat is generated in tumor tissue, which dissipates and diffuses primarily through the vasculature, towards the healthy tissue surrounding the tumor. Some portion of this heat will escape from the skin (top surface). As discussed, the convective heat transfer through the skin depends upon the ambient condition as well as the orientation of this surface (horizontal, vertical, and inclined position). The convective heat loss from any surface is parametrized in terms of heat transfer coefficient (h_c) [144]. This coefficient depends upon various factors like air velocity, position, and posture of limbs as well as thermo-physical properties of air [149] [150] Both, theoretical and experimental studies have reported the effects of ambient conditions on convective heat transfer from the human mannequin [149][150][142]. The heat transfer coefficient (h_c) has been calculated from the empirical relations developed for natural and forced convection heat transfer. If the ambient air velocity is very low ($V \leq 0.2\,\mathrm{m/s}$) the heat transfer primarily occurs through natural convection [144][19]. So, the heat transfer prevails due to the temperature difference only. Kurazumi et.al. [149] developed the correlations of h_c, in natural convection that is given by, $h_c = 0.881 \times \Delta T^{0.368}$ for the spine position of human mannequin. In clinical conditions, ambient air is typically maintained at 18-24 ℃ and 40-65% relative humidity [151]. Thus, with negligible or zero air velocity and $\Delta T \approx 17\,℃$ (with skin temperature of 37 ℃ and ambient air temperature at 20 ℃) convective coefficient comes out to be approximately 2.50 $\mathrm{W/m^2℃}$ for the supine position. This value is evaluated using a correlation developed by Kurazumi et al.[149] for different positions of a human mannequin. Other important factor that affects the h_c, is the velocity of air. Due to the presence of air circulation systems, air condition systems, and fans installed in the hospital environments, the velocity of air is usually greater than zero. Thus, due to the greater velocity of air, the heat transfer from the skin during hyperthermia application becomes forced convection, instead of natural convection. The value of velocity draft in this relation is based upon the thermal sensation according to the ISO and ASHRAE (The American Society of Heating, Refrigerating, and Air Conditioning Engineers) standards, which include a wide range of air speed (0.1-0.8 m/s) and temperature (20-30 ℃) , exists in hospitals [3]. Thus, even in a controlled ambient environment, the variation of air properties, temperature, and velocity leads to a change in the convective heat transfer from the skin to the surrounding air. Kurazumi et.al [144] and Richard et. Al [150] have reported the correlations that describe the influence of air

velocity on convective heat transfer for human mannequin under different body postures. is given as:

$$h_c = 4.088 \times 6.592V^{1.715} \tag{3.1}$$

In present study, we consider clinical operative temperature range 23 to 25 ℃ and velocity of 0.375, and .455 m/s, which is based on human occupancy conditions in hospitals [2] [3]. So, the value of h_c is calculated based on the forced convection relation given above, which are 5 $\mathrm{W/m^2K}$. and 7.5 $\mathrm{W/m^2K}$ for MNPH simulation. This range of heat transfer coefficients accounts for a wide variety of ambient conditions commonly seen in therapeutic environments.

3.3 Mathematical model

Penne's bio-heat model [153] is used as a mathematical model for temperature evaluation in the tumor and the healthy tissue during the therapeutic application of MNPH. General Penne's bioheat equation including the external heat source term is given as,

$$\rho_t c_{pt} \frac{\partial T}{\partial t} = \nabla(k_t \nabla T) + \eta_b \rho_b c_{pb}(T_a - T) + Q_m + Q_s \tag{3.2}$$

where ρ and c_p refer to the density and specific heat of tissues (tumor and healthy) and blood having subscripts *t* and *b*, respectively. k_t is tissue's (tumor and healthy) thermal conductivity, η_b is the blood perfusion through the healthy as well as tumor tissue. Q_m is metabolic heat generation rate and Q_s is the external heat source term in $\mathrm{W/m^3}$.

The heat source term in Eq. (3.2) is Q_s, which acts as an external heat source in $\mathrm{W/m^3}$ and generates heat by MNP during MNPH. The reorientation of MNPs in the direction of the AC magnetic field leads to the generation of heat by Neel and Brownian relaxations, and hysteresis losses mechanisms. The heat generation (Q_s) by MNPs, for single domain MNPs [31] ,which depend upon the particle's magnetic core size hydrodynamic size, other parameters. The remaining details of heat generation are explained in the section 2.2.2 from Eq. (2.1 to 2.4) of the previous chapter 2. It is reported that the smaller-sized nanoparticles require a lesser magnetic moment for their rotation in the viscous cellular environment [154]. Thus, a particle size of 9.5×10^{-9} m radius of iron oxide (maghemite) nanoparticles ($\gamma - Fe_2O_3$) is considered in the present study. The energy or power generation is affected by the physicochemical parameters (i.e., viscosity, hydrophobicity, dielectric constant) of the medium surrounding the MNPs. The viscous environment leads to the development of protein corona, agglomeration,

and bondage to the cell membrane of MNPs. These factors hamper the Brownian rotation of particles, by developing anisotropy in dipolar interaction [155]. Thus, a considerable decrease (of about 50%) in SLP is noticed [43] when the MNPs are injected into a biological medium as compared to aqueous media. Thus, in this work modified SLP induced in the tissue is calculated by multiplying a correction factor α to the aqueous SLP, as given by Eq. (3.4):

$$(SLP)_{modified} = \alpha(SLP)_{aqueous} \tag{3.4}$$

where the value of α is considered as 0.55 [55], to calculate actual heat generation during MNPH. The thermophysical properties of tumor and healthy tissues, MNPs, and magnetic field parameters are given in Table 3.1.

Table 3.1: Thermo-physical properties of tumor and healthy tissue, MNP's, and magnetic field parameters.[76] [156].

Parameter	Value	Parameter	Value
$k_{t\ (tumor)}$	0.48 W/(m.K)	$C_{p\ (blood)}$	3617 J/(kg.K)
$k_{t\ (healthy)}$	0.33 W/(m.K)	$C_{p\ (MNP)}$	670 J/(kg.K)
$\eta_{b\ (healthy\ tissue)}$	0.0050 $m^3/(m^3.s)$	$C_{p\ (healthy\ tissue)}$	2960 J/(kg.K)
$\eta_{b\ (tumor)}$	0.011 $m^3/(m^3.s)$	H_0	10×10^3 and 12.5×10^3 A/m
ρ_{blood}	1050 kg/m^3	f	130×10^3 Hz
$\rho_{healthy\ tissue}$	1041 kg/m^3	η	0.001 N-s/m^2
ρ_{MNP}	5180 kg/m^3	h_c	2.5, 5, and 7.5 W/(m^2.K)
T_a	310 K	$\mathscr{K}$	9000 J/m^{-3}
μ_0	$4\pi\times10^{-7}$ T.m/A	$Q_{m\ (tumor)}$	13600 W/m^3
$Radius_{MNP}$	9.5×10^{-9} m	$Q_{m\ (healthy)}$	700 W/m^3
$\emptyset$	9.6525×10^{-4}	K_B	1.38×10^{-23} J/K

After the dispersion of MNPs inside the tumor region, the tumor tissue density and specific heat change significantly. These changed properties are evaluated by the relations given as [157],

$$\rho_c = (\emptyset \times \rho_{MNP}) + (1 - \emptyset) \times \rho_{ht} \tag{3.5}$$

$$C_{p,c} = \left(\emptyset \times C_{p,MNP}\right) + (1 - \emptyset) \times C_{p,ht} \tag{3.6}$$

Where ∅ denotes the volume fraction (ratio of the volume of MNPs and the tumor volume), subscripts *c*, *ht*, and *MNP* denote the combined, healthy tissue, and MNPs respectively.

3.3.1 Electromagnetic field parameters

For the safe application of MNPH, the amplitude and frequency of the induced magnetic field have a threshold tolerable limit of 35.8 A/m and 13.56 MHz respectively [50]. Thus, their product. i.e. of amplitude and frequency, for the threshold limit is $4.85\times10^{8}\ A/m.s$ [74]. Recently re-addressed by Mag Force system tested on glioblastoma patients, a tolerable limit of $1.35\times10^{9}\ A/m.s$ was observed. However, S. Dutz and R. Hergt [158] have suggested this acceptable threshold limit upto $5\times10^{9}\ A/m.s$. Considering this safety aspect, two heating powers (field amplitudes of 10 kA/m and 12.5 kA/m at constant field frequency of 130 kHz) have been used in the present study for simulation, which is well within the safe limit of magnetic field strength for therapeutic application of MNPH [50].

3.3.2 Boundary conditions (BC's) on tumor model

The boundary conditions are in line with the corresponding physical conditions on the respective surfaces of the tumor model. The top face of the geometric model is liberating heat by convection to the surrounding air as shown in Figure 3.1. The bottom surface of the tumor model is at the core body temperature, i.e., 37 ˚C. And the other four sides (east, west, front, and back as shown in Figure 1) are considered adiabatic since these surfaces are distant from the heated zone (selected size of healthy tissue domain is much greater than tumor size). Thus, heat transfer from these surfaces is negligible. The continuity of temperature field and conservation of energy is applied at the interface boundary between the tumor and healthy tissue. The mathematical form of all BC's corresponding to the considered physical model in Figure 3.1, are as follow,

On vertical walls (surfaces) of the tumor model

$$\left.\frac{\partial T(0,t)}{\partial x}\right|_{west} = \left.\frac{\partial T(0,t)}{\partial x}\right|_{east} = \left.\frac{\partial T(0,t)}{\partial z}\right|_{front} = \left.\frac{\partial T(0,t)}{\partial z}\right|_{back} = 0 \qquad (3.7)$$

Convective top surface (skin)

$$-k\left.\frac{\partial T(0,t)}{\partial y}\right|_{top} = h_c(T|_{top} - T_a) \qquad (3.8)$$

Bottom surface $$T|_{bottom} = T_c \quad (3.9)$$

The conservation of energy at the interface boundary between the tumor and healthy tissue is applied to obtain the interface boundary condition.

3.3.3 MNP distribution

MNP dose with a volume fraction of 5 mg MNP/cm^3 of tumor tissues is reported to be sufficient to produce a reasonable thermal effect [71], Therefore, considering 5 mg MNP/cm^3 of tumor tissues, a total of 16.87 mg of MNP mass being injected at the center of the tumor tissue. The distribution of MNPs in 3D tumor after injection is considered as Gaussian and is calculated by the Gaussian distribution function (Eq. (3.10)) [159], given as

$$mass(x,y,z) = \int_{\Delta V} \frac{1}{\sigma_x\,\sigma_y\,\sigma_z \times \sqrt{(2\pi)^3}} . exp\left[-\left\{\left(\frac{x-\bar{x}}{2\sigma_x}\right)^2 + \left(\frac{y-\bar{y}}{2\sigma_y}\right)^2 + \left(\frac{z-\bar{z}}{2\sigma_z}\right)^2\right\}\right] \quad (3.10)$$

where, $\bar{x}$, $\bar{y}$, $\bar{z}$ are the point of injection of MNP mass and $\sigma_x, \sigma_y, \sigma_z$ are the standard deviation along x, y, and z directions, respectively. The σ_x, σ_y, and σ_z are taken equal to 1.97 mm (13.13% size of tumor length). The considered value of σ is close to an experimentally obtained value 3σ = 5.92 mm, in 0.2% agarose concentration gel with MNP injection rate of 4 μl/min flow [33]. This injection rate in soft tissue (similar to 0.2% agarose concentration gel) produces a near-spherical shape of nano-fluid diffusion [33] .

3.3.4 Thermal dosimetry

The effect of heating the tissue is calculated in terms of thermal dosimetry (Thermal damage). Thermal damage to the tissue is calculated using the Arrhenius relation [160] given by:

$$\Omega(x,y,z,t) = \int_0^{\tau} A.\, e^{\frac{E_a}{RT(x,y,z,t)}} = ln\frac{C(0)}{C(\tau)} \quad (3.11)$$

where Ω denotes the non-dimensional thermal damage parameter, which is a natural log of the ratio of $C(0)$, percentage of undamaged tissue before heating starts, and $C(\tau)$, percentage of undamaged tissue after being heated for time 'τ'. It should be noted that, for a value of about Ω = 4.6, around 99 % of tissue gets damaged [160] In the present study, the value of Ω= 4.6

(corresponds to 99 % of tissue damage) is chosen as the threshold value for cell damage. In Eq. (3.11), 'A' denotes the collision frequency (frequency factor) of the molecules (1/s). 'E_a' is the energy ($\mathrm{J/mol}$) required to activate and excite the molecules to initiate the reaction required for tissue damage, 'R' is the universal gas constant ($\mathrm{J/(mol.\,K)}$), and T denotes the temperature (K). The values of E_a, A, and R considered in this study for cell death are 6.19×10^5 $\mathrm{J/mol}$, 2.84×10^{99} $\mathrm{s^{-1}}$, and 8.314 $\mathrm{J/(mol.\,K)}$, respectively [160].

Thermal dose based on the cumulative equivalent minutes, at a reference break-point temperature of 43 ˚C, and termed as CEM43 [161][162] is also used in this study to measure the effectiveness of MNPH. The expression for the calculation of CEM43 is given as,

$$CEM43 = \sum_{i=1}^{n} R_{CEM}{}^{(43^{\circ}C - T_i)}.\, t_i \tag{3.12}$$

where, R_{CEM} is a proportionality constant, whose value is 0.5 for $T_{tissue} > 43^{\circ}C$ and 0.25 for $T_{tissue} \leq 43^{\circ}C$ [160], T_i is the tissue temperature (˚C) at i^{th} time interval, t_i is time at T_i, and n, is the total number of time intervals. It is reported in the literature that the thermal isoeffect dose in the form of CEM43, is effective when a dose of 60 minutes or longer [163] is applied to the tissue. And, this effect is represented by $(CEM43)_{60}$.

These damage parameters are quantified in terms of volumetric percentage damage of tumor tissue relative to the tumor volume, which is given by the following equations,

$$C_{d\ volume}(\%) = \left(\frac{tissue\ volume\ having\ \Omega \geq 4.6}{Tumor\ volume}\right) \times 100 \tag{3.13}$$

$$CEM43_{60)\ volume}(\%) = \left(\frac{tissue\ volume\ having\ CEM43_{60}}{Tumor\ volume}\right) \times 100 \tag{3.14}$$

The thermal damage parameter, C_d , represents the tissue volume having the value of $\Omega \geq 4.6$, (Eq. (3.13)). The percentage volume of the tumor tissue having threshold value of thermal dosimetry parameters C_d and $(CEM43)_{60}$ is calculated using Eq. (3.13) and Eq. (3.14), respectively. Moreover, if the value of tumor tissue damage exceeds 90 % of the tumor volume, and healthy tissue damage is less than 10 % of the tumor volume then treatment is considered to be effective [159].

3.3.5 Perfusion model

The blood perfusion varies with the elevation in temperature [159]. In the present study, the first-order irreversible kinetic Arrhenius model of blood perfusion has been employed. The blood perfusion, η_b, is a linear function of the non-dimensional parameter, degree of microvascular stasis (MVS) [159], whose value depends upon non-dimensional thermal damage parameter Ω (Eq. 3.11). The value of MVS varies between 0 and 1.

$$MVS = 1 - e^{-\Omega} \tag{3.15}$$

The perfusion model is given by Eq. (3.16):

$$\eta_b = \begin{Bmatrix} \eta_{bi}\,(30 \times MVS + 1), & MVS \leq 0.02 \\ \eta_{bi}\,(-13 \times MVS + 1.86), & 0.02 \leq MVS \leq 0.08 \\ \eta_{bi}\,(-0.79 \times MVS + 0.884), & 0.08 \leq MVS \leq 0.97 \\ \eta_{bi}\,(-3.87 \times MVS + 3.87), & 0.97 \leq MVS \leq 1.0 \end{Bmatrix} \tag{3.16}$$

where, η_{bi} is the base blood perfusion of tissues (both healthy and tumor). However, this base perfusion is different for both tumor and healthy tissues. Breast tumors have a similar feature as the proximity to ambient conditions, the factor considered in this study. In this study, moderate blood perfusion is considered, which is 0.011 s^{-1} for the breast tumor tissue and 0.5 $\times 10^{-3}$ s^{-1} for the healthy tissue [156].

3.4 Computational methodology and validation

To apply this bio-heat equation over a computational domain, the finite volume method (FVM) has been considered as a solution methodology to discretise the equation. A domain, that is to be numerically studied using the FVM, must be divided into subdomain, called as finite volumes. All control volumes contain nodes, located at their centres. These nodes serve as the storage location of all parametric values for the respective control volumes. The nodes located on the east, west, north, and south, of the control volume are generally designated by E, W, N, and S, respectively. P stands for the node itself of the control volume under consideration. The boundaries separating a control volume from its neighbours located on its east, west, north, and south are denoted by, E, W, N, and S, respectively.

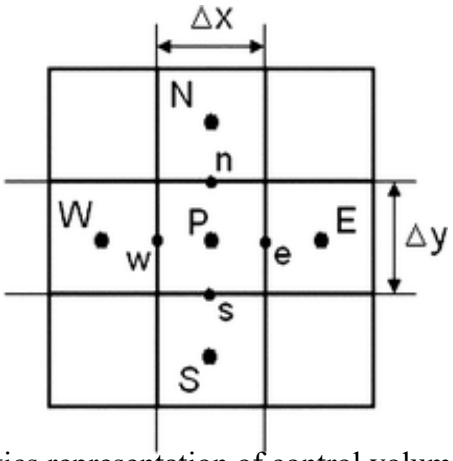

Figure 3.3: Schematics representation of control volume with its neighbor.

Distance between two consecutive nodes, along the x, and y direction, are given by Δx, and Δy, respectively. A control volume, along with its neighbours, are illustrated in Figure 3.3. To discretize a partial differential equation, it is integrated over the control volume dV. For a time-dependent equation, it is integrated over the time step dt, as well. Therefore, the transient two-dimensional Pennes bioheat equation, Eq. (3.17), in integral form, can be written as,

$$\int_t^{t+dt}\left(\iiint \rho_t c_{pt}\frac{\partial T}{\partial t}dV\right)dt = \int_t^{t+dt}\left\{\iiint \frac{\partial}{\partial x}\left(k_t\frac{\partial T}{\partial t}\right)+\frac{\partial}{\partial y}\left(k_t\frac{\partial T}{\partial t}\right)dV\right\}dt + \int_t^{t+dt}\left(\iiint \eta_b\rho_b c_{pb}(T_a-T)\,dV\right)dt + \int_t^{t+dt}\left(\iiint (Q_m+Q_s)\,dV\right)dt \quad (3.17)$$

Using implicit scheme and discretising the Eq. 3.17 with terms on right hand side of above equation and is integrated them over time step dt, we get:

$$\rho_t c_{pt}(T_a-T_P^0)dV = \left[k_t A_x\left(\frac{T_E-T_P}{\delta x_{EP}}\right)-k_t A_x\left(\frac{T_P-T_W}{\delta x_{PW}}\right)\right]\Delta t + \left[k_t A_y\left(\frac{T_N-T_P}{\delta y_{NP}}\right)-k_t A_y\left(\frac{T_P-T_S}{\delta y_{PS}}\right)\right]\Delta t + \left[\eta_b\rho_b c_{pb}(T_a-T_P)dV\right]\Delta t + [(Q_m+Q_s)dV]\Delta t \quad (3.18)$$

$$A_P T_P = A_E T_E + A_W T_W + A_N T_N + A_S T_S + A_P^0 T_P^0 + S \quad (3.19)$$

Where, $A_E = k_t A_x/\delta x_{EP}$, $A_W = k_t A_x/\delta x_{WP}$, $A_N = k_t A_y/\delta y_{NP}$, $A_S = k_t A_y/\delta y_{SP}$, $A_P = A_E + A_W + A_N + A_S$, $A_P^0 = (\rho_t c_{pt}\partial x\partial y)/\Delta t$, and $S = (Q_m + Q_s)\partial x\partial y$

Finally, the temperature (T_P) at central node point 'P' is calculated using a definite convergence criterian. Gauss-Seidel as an iterative solver is considered for the solution of the discretized form of above-mentioned equations.

To validate the computational methodology used in this study, a comparison of the spatial temperature profile is done with the experimental study. The in-vivo mice study performed by Attaluri et al. [48] demonstrated the temperature mapping of tumor region infused by different infusion rates and distributed volume of ferrofluid. And nearly bell-shaped spatial temperature distribution is noticed away from the injection site, dosed with 25.2 mg of nanoparticle under 3 kA/m and 190 kHz, magnetic field amplitude and frequency respectively. Heat generation and temperature evolution are mainly affected by the dose and distribution of MNP's and magnetic parameters applied. Thus, for comparative analysis similar MNP dose and magnetic field parameters are induced in the tumor model (Figure 3.1) with the depth position of the tumor at D*= 0.5.

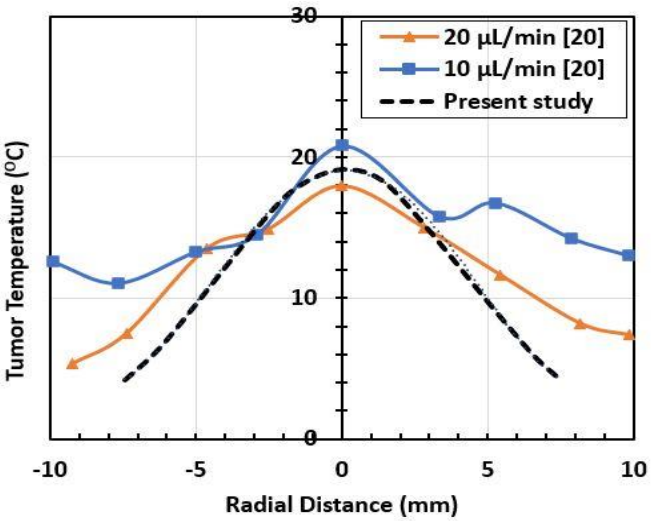

Figure 3.4: Comparison of the spatial temperature profile of tumor region between experimental [48] and the present study.

The comparison of the results of the present computational methodology with experimental study under similar dose and magnetic parameters is are shown in Figure 3.4. It should be noted that the temperature profile measured by a thermocouple in an experimental study [48] also vary with infusion rate (10 µL/min and, 20 µL/min) of MNP fluid to the tumor. In Figure 3.4, the radial distance (both sides) is started from the injection site and the temperature scale started from zero, is equivalent to the base temperature of 37 ˚C.

The distribution of MNP in the tissue is more heterogeneous in the experimental study, in comparison to the Gaussian distribution applied for the MNPs spread in the current study. Due to this a difference in temperature profile can be noticed in the experimental [48] and the present study. However, a close agreement can be seen in the overall curvature of temperature distribution. Thus, the current methodology for simulation of magnetic hyperthermia can be applied to evaluate the other findings pertaining to the magnetic hyperthermia application.

It is well understood that outcome of any computational physics is sensitive to the grid size used in the simulation. Thus, before fixing the gird size or numbers of discrete nodes for the simulation of MNPH, a computational grid refinement test has been conducted. We found at a grid size of $(168 \times 336 \times 336)$ the simulated results nearly become grid-independent. Thus, grid size $(168 \times 336 \times 336)$ is used to simulate MNPH in all the considered tumor models. All simulations are performed on MATLAB 2020b under an academic licensed number of 40604939, which has been run on Dell Precision Tower workstation 5820.

3.5 Results

The MNPH thermotherapy is induced in the tumor model as discussed in Figure 3.1. The duration of MNPH therapy is 1 hour so the simulation time for all the tumor models is 3600 seconds [164]. The temperature in the targeted tissues starts rising as soon as the MNPH applicator is induced. For the initial run, the top surface is maintained at the h_c value of 2.5 $\mathrm{W/m^2K}$ with both heating powers of 10 $\mathrm{kA/m}$ and 12.5 $\mathrm{kA/m}$ at 130 kHz . The transient behavior of temperature is shown in Figure 3.5, which shows the rise of the temperature during MNPH at three different locations on the tumors (center point, mid-point, and the end-point of diagonal OQ (Figure 3.1) with three different depths of the tumor. Three out of six tumor depth positions (D*) {0, 0.25, and 1.0} have been shown, to cover a wide range of tumor positions. It is seen from Figure 3.5 that the rise of temperature is very sharp during the initial duration of therapy. However, after 500 seconds, the time-temperature profile becomes asymptotic, due to equilibrium being achieved between the heat generation by MNPs and heat removal by tissue and vasculature out of this zone. It should be noted that maximum temperature is achieved at the tumor injection center point (O), for all tumor depths. This is due to the higher concentration of MNPs closer to this point [76].

Since the distribution of MNPs in the tissue is Gaussian, thus, the concentration of heat-generating MNPs and temperature reduces with distance from the point of injection and is

manifested in Figure 3.5. It should be noted from Figure 3.5, that, when the one surface of the tumor is directly exposed to the surrounding atmosphere, i.e., D*=0, the temperature elevation in the tumor is higher in comparison to the other tumors allocated at greater depth from the skin (D*>0).

Thus, the maximum temperature achieved is nearly 78 ˚C at the tumor center for 10 kA/m, for D*= 0. At two other locations (diagonal mid-point, diagonal endpoint) temperature for D*= 0 is 52 ˚C and 41.3 ˚C, respectively. For the higher heating amplitude, it is around 95 ˚C, 55 ˚C, and 43 ˚C for the considered three points on tumor diagonal respectively.

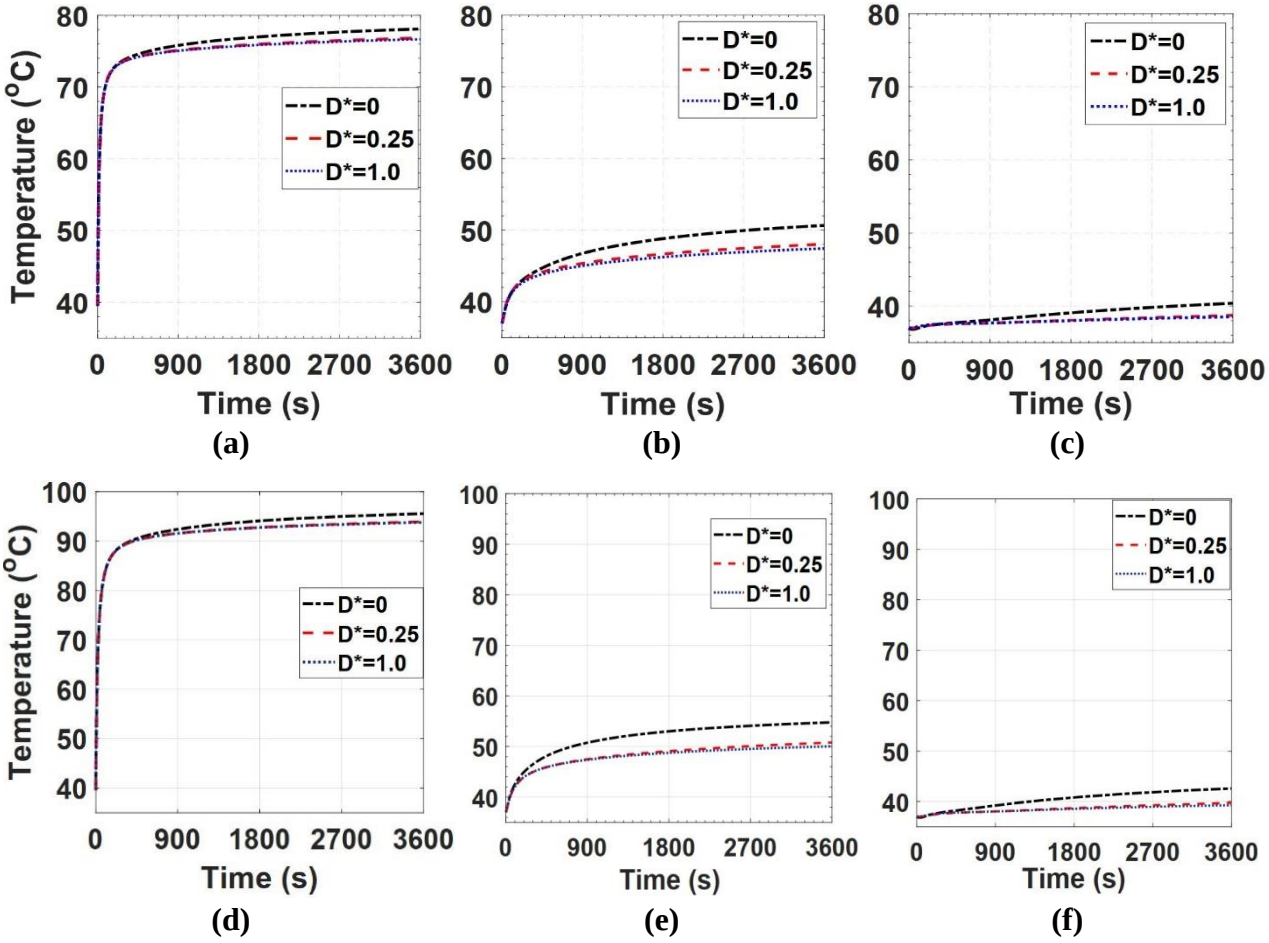

Figure 3.5: Temporal temperature distribution during MNPH for two heating conditions 10 kA/m Figure **(a), (b), (c),** and 12.5 kA/m (Figure **(d), (e), (f),** along with the tumor diagonal OQ at three points. Figure **(a, d)** Tumor center point **(b, e)** diagonal mid-point **(c, f)** diagonal endpoint.

For other tumor depth positions, D* {0.25, 1.0}, the temperature is lower than that at D*=0 at as shown in Figure 3.5. The reason for lower elevation in temperature for the tumors having D*>0, is the better thermal regulation induced by the perfusion through microvasculature,

when the tumor is surrounded by healthy tissue, i.e., at D* equals 0.25 and 1.0. Similar behavior is also observed, at the higher heating power (12.5 kA/m, 130 kHz).

3.5.1 Spatial temperature distribution

The steady-state spatial distribution of the temperature in the form of isotherms on the plane ABCD (Figure 3.1) for all the considered depths of the tumor with a heating power of (10 kA/m, 130 kHz and heat transfer coefficient (h_c) of 2.5 W/m^{2}K) is shown in Figure 3.6. In this Figure, the central square-shaped tumor tissue is surrounded by healthy tissue.

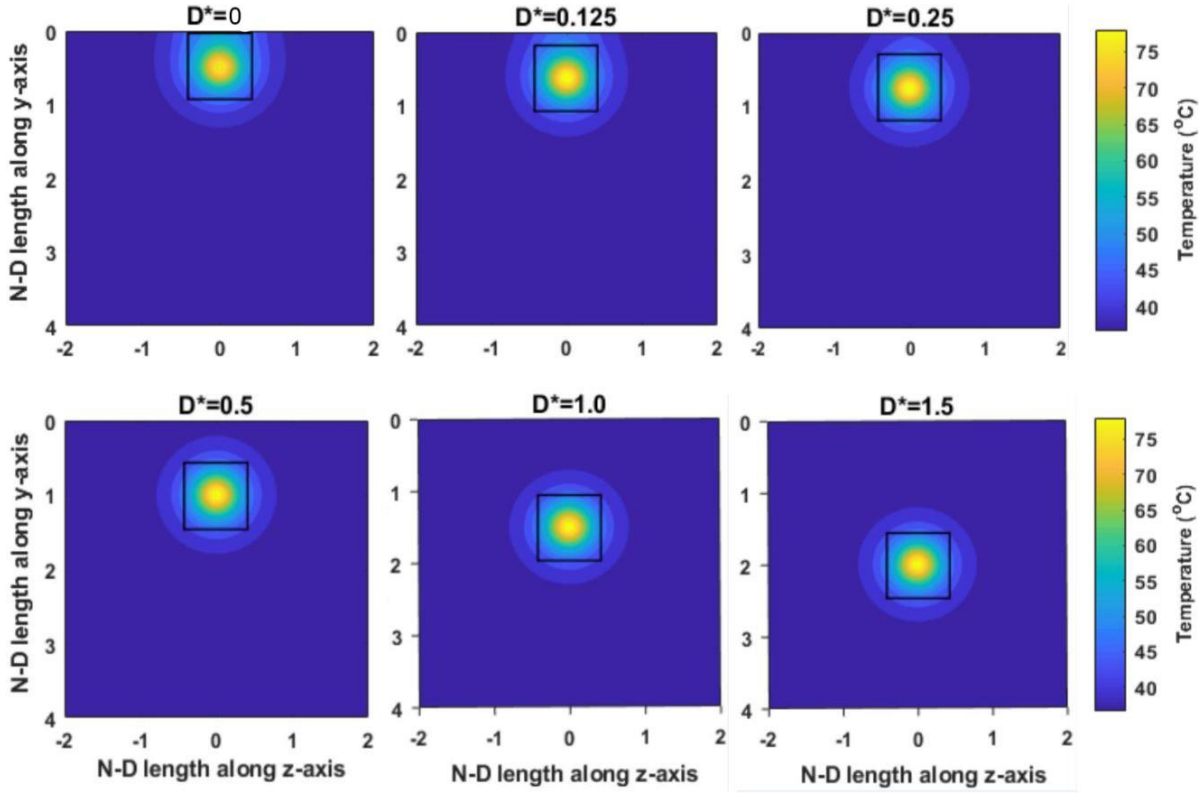

Figure 3.6: Comparison of temperature isotherms for the different tumor depths during MNPH along a central ABCD plane passes through tumor centroid at a heating power of 10 kA/m at 130 kHz. The Figure title inscribed as D* starting from 0 to 1.5 represents the tumor depth position in *y*-direction.

The lengths along the horizontal (*z*-axis) and vertical axis (*y*-axis) in these isotherms are represented in the form of a non-dimensional size (L/w_t). It should be noted from this figure that, the temperature distribution inside the tumors is in accordance with the MNP distribution pattern (Gaussian). The temperature contour is symmetric around the tumor tissue for the tumor depth $D^* \geq 0.5$, however, is asymmetric for the tumor depth less than 0.5. Again, following

the previous figure, the maximum temperature is observed at the centroid of tumor tissue, which is also the MNP injection point in the tumors, and decreases as we proceed towards the tumor boundary. Similar behavior in isotherms is also observed with higher heating power (12.5 kA/m, 130 kHz). However, the isotherms for higher heating power are not repeated for the sake of brevity.

The detailed description of the spatial variation of temperature in the tumor model at two different heating conditions is shown in Figure 3.7. The six considered tumor depth locations (D*) from 0 to 1.5 are inscribed as a legend in this figure.

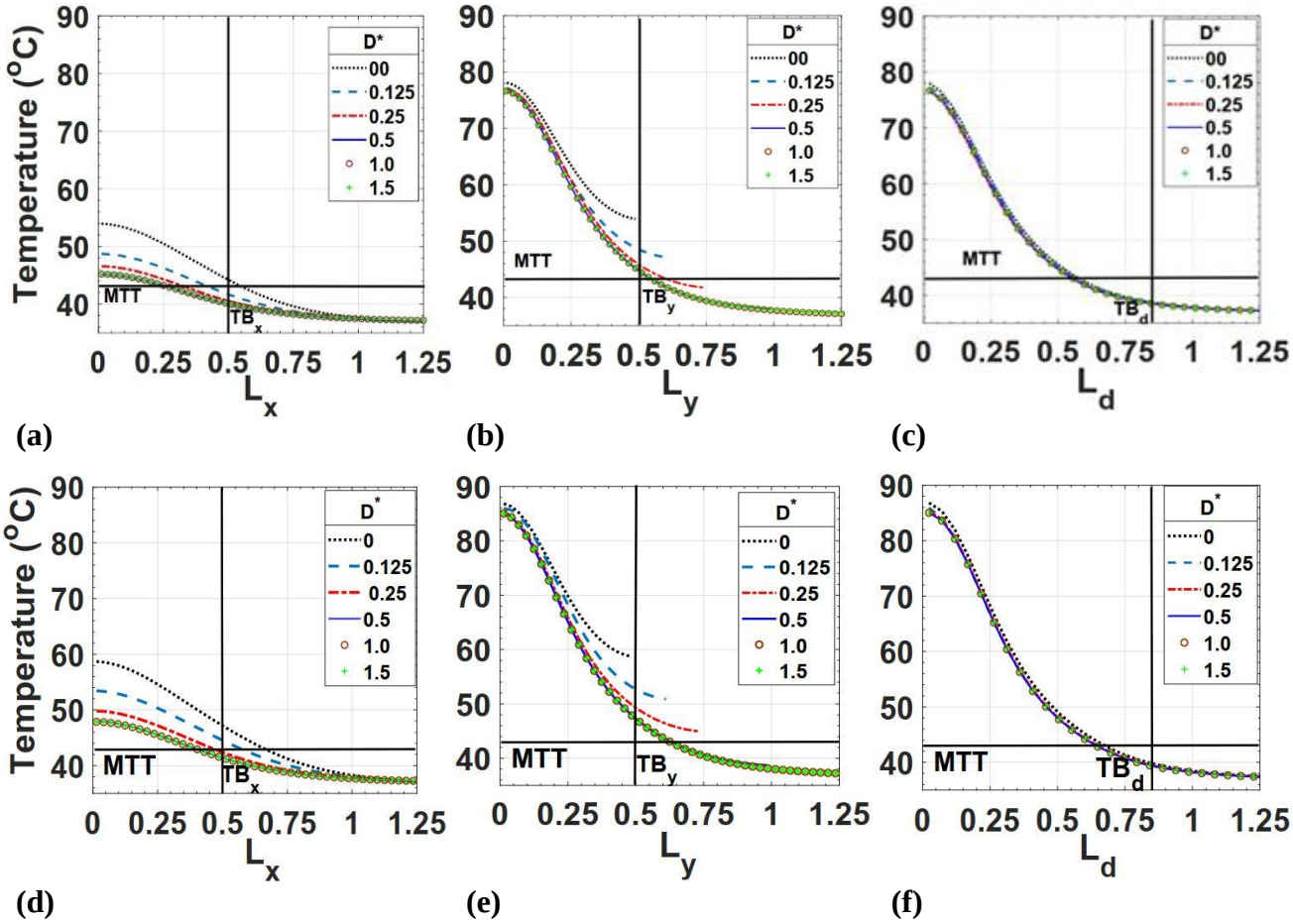

Figure 3.7: Comparison of spatial temperature profile for different depths of the tumor along three lines at two field amplitudes of 10 kA/m (Figure **a, b, c**) and 12 kA/m (Figure **d, e, f**). Tumor top surface line (NM) along the *x*-axis in Figure **(a, d)**, vertical centerline (ON) towards top surface along the *y*-axis Figure (**b, d**). tumor diagonal line (OQ) by Figure (**c, f**), for a convection coefficient (h_c) of 2.5 W/m^{2}K.

Here MTT denotes minimum therapeutic temperature (43°C), and, TB_x (OR), TB_y (ON) and TB_d (OQ) stand for the tumor boundary in the *x*-direction, *y*-direction, and along with tumor diagonal, respectively, from the center i.e., point of injection of the tumor as shown in Figure

3.1 in the tumor tissue. Here, in Figure 3.7 tissue temperature is plotted on the ordinate, and a non-dimensional (N-D) tissue length ($L_{ND} = \mathrm{L}/w_t$) scale with zero as the center of the tumor model is used for labeling the abscissa. This N-D scale as represented by L_X, L_Y, and L_d, is the length scale along *x*, *y*, and diagonal directions respectively. Since the temperature profile become asymptotic to approximately 37 ˚C beyond L_{ND}=1. Thus, the value of L_{ND} in all the plots in this figure is restricted to 1.25 i.e., L=1.875 cm. Figure 3.7 (a), and Figure 3.7 (d) shows the temperature plot along a centerline on the top surface of the tumor as shown by line (NM) in the tumor tissue (Figure 1) for lower (10 kA/m) and higher heating (12.5 kA/m), respectively.

It is observed from this plot that, when the tumor is at D*= 0, the temperature on the tumor top surface is quite high in comparison to other tumors depths for both heating conditions. As the tumor depth increases the temperature gradually decreases on this surface. Furthermore, on this surface, for superficial tumors with negligible or zero healthy tissue depth (D*= 0) temperature is well above minimum therapeutic temperature (MTT) up to the boundary of the tumor. However, with an increase in depth (D*>0), the temperature drops below MTT, before reaching the tumor boundary for lower field amplitude. It is also observed from the plots (Figure 3.7 (a, d)) that for the last three tumor positions i.e., D*= 0.5, 1.0, and 1.5, the temperature curves are very close to each other.

Thus, after a certain depth, the upper surface temperature of the tumor becomes independent of the tumor depth position. Figure 3.7 (b) and Figure 3.7 (e) show temperature along the vertical centerline (ON) as described in Figure 1, with different tumor depths for lower and higher heating conditions, respectively. The length of the tissue (tumor + healthy) along this line (ON) keeps on increasing as the tumor moves towards greater depths. Again, along this line, a reasonable variation in temperature is observed as the depth of the tumor increases. However, for all the cases, the temperature profile remains above the MTT upto the tumor boundary i.e., TB_y. There is no significant difference between the temperature profiles (Figure 3.7 (c) and (f)) along the diagonal line (OQ) (*Figure 3.1*) observed with the variation in the depth of tumor for both heating conditions. From Figure 3.7 (c and f), it is also observed that temperature inside the tumor region for all tumor positions along the tumor diagonal (OQ), the temperature drops below MTT, before reaching the tumor boundary. This is because the far end of the tumor along this diagonal does not receive sufficient heat from MNPH.

Thus, heat generation by MNPs with a considered distribution pattern is not able to maintain the temperature above the MTT near this extreme end of the tumor along the diagonal. The detailed description of the temperature profile induced due to MNPH in the tumor mass shows that temperature is nonhomogeneous in the 3D tumor volume or mass. One more observation inferred from this plot (Figure 3.7) is that the temperature profile is higher especially in the upper half of the tumor tissue for the superficial tumors in comparison to tumors located at higher depth ((D*>0.25).

3.5.2 Effect of variation in the convection coefficient on the temperature profile

In the previous results, temperature profiles are shown (Figure 3.7) for MNPH simulation with a lower value of heat transfer coefficient (h_c =2.5 W/m^{2}K).

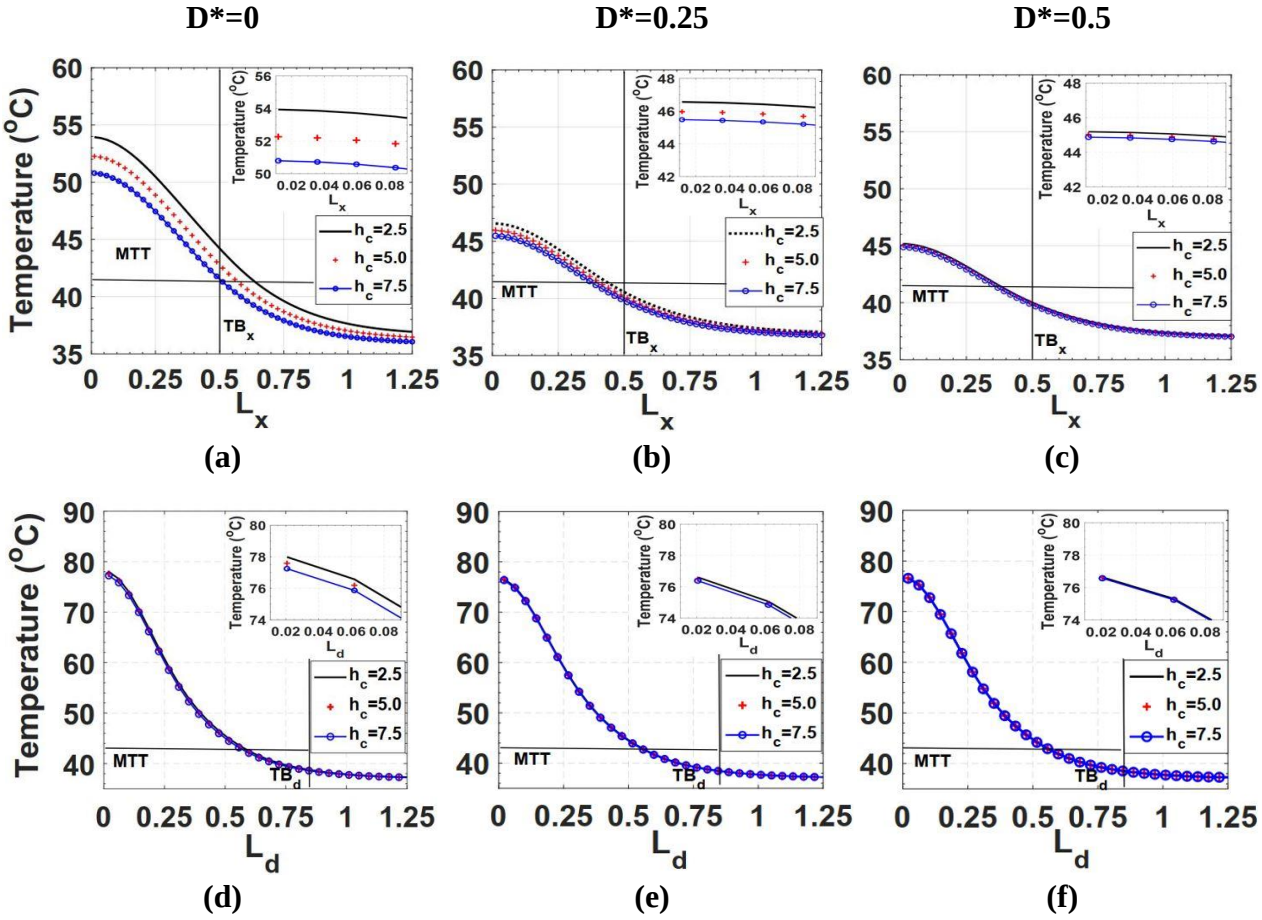

Figure 3.8: Comparison of the effect of convection coefficient, h_c {2.5, 5.0 and, 7.5 W/m^{2}K}, on spatial temperature profile in the tumor model for three depths, D*{0, 0.25, 0.5 (column-wise)} of tumor at a field amplitude of 10 kA/m. Temperature profile, **(a)** to **(c)** along the top surface line (NM), **(d)** to **(f)** along the tumor diagonal line (OQ).

However, under different circumstances, as the air velocity in the therapeutic environment increases, the heat transfer from the skin is also enhanced. Thereafter, different convective conditions (h_c){ 2.5, 5.0, and 7.5 W/m^2K} on the upper surface (skin) are applied to evaluate their effect on MNPH. Again, the temperature profile with different convective conditions on the skin is plotted along NM and OQ lines, as discussed in Figure 3.7.

These spatial temperature profiles have been plotted only for three tumor depth locations D*{0, 0.25, and 0.5} for lower (10 kA/m) and higher heating (12.5 kA/m) (Figure 3.8, and Figure 3.9, respectively). The tumor depth positions beyond 0.5, are not considered in these plots since the temperature profile beyond this depth nearly coincides with the temperature profiles of consecutive depths position of D*= 0.5. It is evident from these plots that the temperature profile gets affected by the variation of the heat transfer coefficient on the skin.

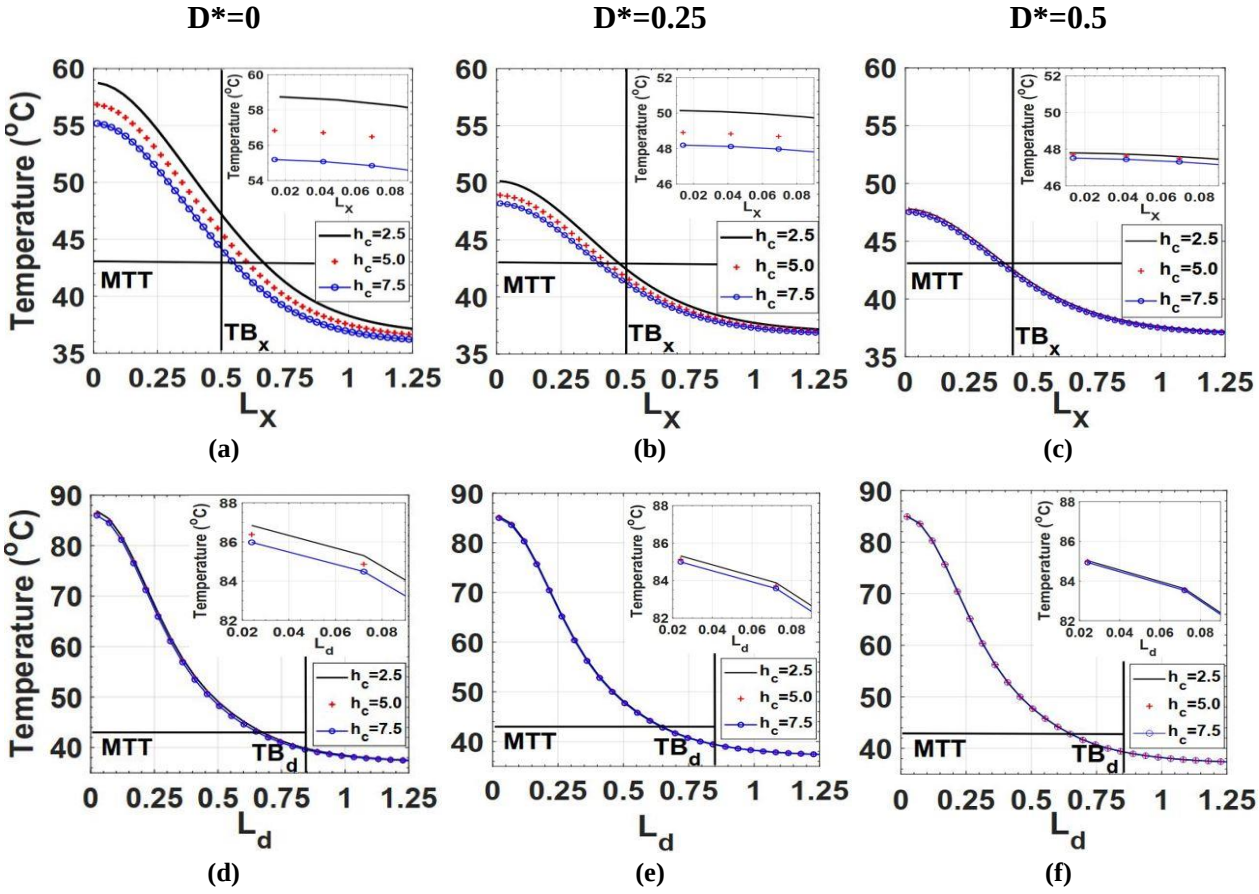

Figure 3.9: Comparison of the effect of convection coefficient, h_c{2.5, 5.0 and, 7.5 W/m^2K}, on spatial temperature profile in the tumor model for three depths, D {0.0, 0.25, 0.5 (column-wise)} of tumor at a field amplitude of 12.5 kA/m. Temperature profile, (a) to (c) along the top surface line (MN), (d) to (f) along the tumor diagonal line (OQ).

This effect is predominant on the upper half of the tumor (Figure 3.8 (a), (b), and (c), as well as Figure 3.9 (a), (b), and (c), especially for the tumors that are very close to the skin (D*≤

0.25) for both the heating conditions. As in Figure 3.7 (c), and Figure 3.7 (f) the diagonal line (OQ) temperature is marginally distinguishable for all considered tumor positions. And the same behavior prevails with different convection coefficient values for different tumor depth positions as shown in Figure 3.8 (d - f) and Figure 3.9 (d - f) and is nearly independent skin effect. Moreover, as the tumor depth increases to D* = 0.5 temperature profiles attain equivalency to others as shown in Figure 3.8 (c & f) and Figure 3.9 (c & f), respectively.

Thus, as the depth of the tumor is increased, the skin effects are weakened, and after the tumor depth of 0.5, the temperature profile nearly becomes independent of skin exposed conditions. However, with an increase in the heat transfer coefficient (h_c), the temperature of the top portion of the tumor is substantially reduced for superficial tumors (D*<0.5). This results in a higher tumor volume of superficial tumors that remains below the MTT i.e., 43℃. Thus, the increase of heat transfer coefficient significantly affects the therapeutic effect, especially for superficial tumors. A detailed quantitative description of the therapeutic effects of MNPH due to the variation of tumor depth and skin ambient conditions in terms of thermal dosimetry is provided in the following section.

3.5.3 Thermal dosimetry during MNPH

The treatment efficacy is quantified in terms of two thermal damage parameters C_d and $(CEM43)_{60}$ as discussed in section 2.2.4. The values of C_d and $(CEM43)_{60}$, for different positions of the tumors and with different heat transfer coefficients under both the heating conditions are given in Table 3.2 and Table 3.3, respectively. It should be noted from these Tables that the volumetric thermal damage in terms of C_d and $(CEM43)_{60}$ for tumor tissue reduces with an increase of the depth of tumor as well as an increase of the heat transfer coefficient. The maximum damage (nearly 75% in terms of C_d and 73% in terms of $(CEM43)_{60}$) for 10 $\mathrm{kA/m}$ and (nearly 90% in terms of C_d and 89% in terms of $(CEM43)_{60}$) for 12.5 $\mathrm{kA/m}$ is induced to the tumor mass having one of its surfaces exposed to the environment (D*= 0) with a heat transfer coefficient of 2.5 $\mathrm{W/m^2K}$. The lower heat transfer rate due to the lower value of h_c, at the top surface leads to an accumulation of heat inside the tissue, and consequences in an increase in temperature.

This phenomenon is visible in Figure 3.7 (a, d), 8 (a), and 9 (a). Thus, the thermal dose induced to the targeted tumor zone is greater, which leads to greater thermal damage in the tissue

volume. Even for this position of the tumor, the thermal damage reduces with the increase in the heat transfer coefficient.

Table 3.2: Thermal damage (% C_d) in tumor due to MNPH, for the considered tumor depths with different convective heat transfer coefficients and field amplitudes at a frequency of 130 kHz.

	% volume of C_d in tumor region					
	h_c=2.5 W/m^2K		h_c=5 W/m^2K		h_c=7.5 W/m^2K	
Tumor Depth (D*)	H_0 (A/m) 10×10^3	H_0 (A/m) 12.5×10^3	H_0 (A/m) 10×10^3	H_0 (A/m) 12.5×10^3	H_0 (A/m) 10×10^3	H_0 (A/m) 12.5×10^3
0	74.95	90.31	70.17	87.91	65.92	85.06
0.125	65.38	84.63	62.11	81.88	59.71	79.29
0.25	60.32	79.83	59.01	77.89	57.80	76.48
0.5	59.12	77.10	58.70	76.68	58.37	76.37
1.0	59.38	77.20	59.31	77.17	59.26	77.08
1.5	59.45	77.20	59.45	77.30	59.45	77.15

This trend continues up to the tumor depth of D*= 0.5. However, the effects of skin environmental conditions on thermal dosimetry reduce with the increase in depth of the tumor.

Table 3.3: Thermal damage ($(\mathrm{CEM43})_{60}$) in tumors due to MNPH for the considered tumor depths with different convection coefficients and field amplitude at a frequency of 130 kHz.

	% volume of $(CEM43)_{60}$ in tumor region					
	h_c=2.5 W/m^2K		h_c=5 W/m^2K		h_c=7.5 W/m^2K	
Tumor Depth (D*)	H_0 (A/m) 10×10^3	H_0 (A/m) 12.5×10^3	H_0 (A/m) 10×10^3	H_0 (A/m) 12.5×10^3	H_0 (A/m) 10×10^3	H_0 (A/m) 12.5×10^3
0	73.22	89.37	68.17	86.74	63.96	83.74
0.125	63.26	83.16	60.18	80.29	57.72	77.67
0.25	58.35	78.07	57.04	76.30	55.89	74.86
0.5	57.16	75.70	56.78	75.18	56.45	74.73
1.0	57.36	75.80	57.30	75.55	57.25	75.70
1.5	57.40	75.82	57.40	75.60	57.40	75.77

Again, the reason behind this is the increase in heat transfer from the skin with a higher value of h_c. This higher value of the heat liberation from the skin reduces the temperature on the top portion of the tumor and leads to lower damage to the tumor volume.

It is evident from Table 3.2 that the thermal damage reduces from 75% with h_c=2.5 $\mathrm{W/m^2K}$ to nearly 66% with h_c=7.5 $\mathrm{W/m^2K}$ for the tumor exposed to the ambient (D*=0) at an amplitude of 10 $\mathrm{kA/m}$. Thus nearly 12% reduction in tumor volume damage occurs when the heat transfer coefficient increases from 2.5 $\mathrm{W/m^2K}$ to 7.5 $\mathrm{W/m^2K}$ for this case. However, around 5% reduction can be noticed for a higher heating category.

Beyond this depth of tumor, therapeutic effects are not influenced by the skin conditions. It should also be noted from these Tables that the volumetric thermal damage reduces quickly as the depth of tumor increases from D*= 0. This behavior of the reduction of thermal damage with the depth of the tumor is observed even for a higher heat transfer coefficient. With the increase in tumor depth, the thickness of healthy tissue above the heating zone increases, which enhances the perfusion through the vasculature. The heat transfer through perfusion also increases with the increase in the temperature of the tissue results in lower heat accumulation near the top portion of the tumor for deep tumors. Experimental results have also shown that heat transfer through tissue enhances with the increase in the perfusion of the tissue [165].

This results in lower damage to the depth tumors in comparison to superficial tumors. So, it is concluded from these results that thermal damage to the targeted tumor volume is influenced by the location of the tumor. And the thermal losses through the skin are smaller than the losses through the tissue for all the considered heat transfer coefficients. Along with that, the therapeutic effect is also influenced by the ambient therapeutic conditions. However ambient conditions have greater effects on superficial tumors.

3.6 Discussion

The tumor cells generally grow at randomized locations in any part of the human body. In cases of skin cancer, lung cancer, and breast cancers, the tumor cells grow beneath the skin surface and even sometimes these cells generate on the outer skin surface itself. Therefore, the present work investigates the therapeutic effect of the MNPH treatment, when the tumor is positioned at different depths beneath the skin surface. Also, the thermoregulatory response of the magnetically heated tumor tissue under the effect of variable ambient (surrounding) conditions has not been investigated so far. So, the effects of both these factors (position of the tumor as

well as skin heat transfer characteristic) on 3D tumor models (representing a T1 type tumor) are investigated by simulating the MNPH. Impacts of these factors on temporal and spatial variation in the temperature and thermal dosimetry have been examined. It should be noted that results generated in this work depend on the applicability and assumptions of mathematical models (Penne's bio-heat model & Rosensweig's model for heat generation from MNP). Even though both the models have their limitations [166] [167], still these models are routinely used in much computational work for their simplicity & having reasonable accuracy [56]. Moreover, incorporation of parameters (h_c, correction factor α in SLP, MNP distribution parameter σ) from the experimental works enhance the accuracy of the computational results. Thus, within this framework, from the results, it is observed that temperature elevation during MNPH is not homogeneous in the tumor volume. Especially for the superficial tumors, temperature elevation is greater in the upper region (nearer to skin) of the tumor volume in comparison to the lower portion of tumor volume. This is due to the fact that, when tumor has a greater thickness of healthy tissue above it, the thermo-regulation due to perfusion is better on this surface. Thus, for tumors located at greater depths, the temperature on their top surface is significantly less in comparison to tumors that are close to the skin. This reduced elevation of temperature in the tumor tissue for the deep-rooted tumor results in reduced damage of the tumor volume in terms of C_d and $(CEM43)_{60}$ (Table 3.2 and 3.3) under similar therapeutic conditions. Computational results of the considered tumor model show that the damaging effect due to MNPH becomes independent of the tumor depth after D*= 0.5. Similarly, a change in heat transfer rate from the skin by changing the ambient condition has greater effects on the therapeutic efficacy for superficial tumors (Table 3.2 and 3.3). However, as the depth of the tumor increased (D*>0.5) the skin effects become negligible (Table 3.2 and 3.3). Thus, deep-rooted tumors (D*>0.5) are not influenced by the environmental condition of the skin. However, superficial tumors (D*<0.5) are greatly influenced by the environmental conditions on the skin during MNPH. One more conclusion infers from this study that under similar magnetic field parameters and MNP dose, superficial tumors (D*<0.5) have higher therapeutic effects in terms of thermal dosimetry in comparison to deep-rooted tumors (D*>0.5). Again, the reason is well stated above. Though in this work effects of tumor location and skin environmental conditions on MNPH are demonstrated with the tumor model having a tumor size of 1.5 cm. However, further studies may require investigating the influence of other parameters like heterogeneous distributions of MNP in the tissue, other sizes of the tumor, and the effects of tissue physiology like multilayer tissue consideration or heterogeneity of tissue on the critical depth of the tumor.

3.7 Conclusions

The present chapter quantify the effect of the location of tumor beneath the skin as well as environmental conditions, on the therapeutic effects of MNPH. This investigation leads to the establishment of the relation between the depth of tumor and the therapeutic effects of MNPH. This study concludes that, up to the critical depth of tumor, about half of the tumor size, the therapeutic effects in terms of elevation of temperature and thermal dosimetry are susceptible to the change in therapeutic environment on the skin as well as the depth of the tumor. However, beyond these therapeutic effects of MNPH become independent of these two parameters.

CHAPTER 4

Computational Evaluation of Optimum MNP Dose using Realistic Breast Tumor Models.

4.1 Introduction

A numerical investigation for the estimation of thermal damage and spatial temperature distribution in magnetic hyperthermia has been done in the previous chapter. The observation from the computational study are that the tumor location beneath the skin and the influence of outer ambient conditions affect the therapeutic effects of hyperthermia. The tumor model for applying magnetic hyperthermia was a regular cubic-shaped tumor geometry. Moreover, it is noticed that most of the computational studies on MNPH restrict their simulation to simple 2D or 3D tumor geometries, such as spheres, cylinders, or elliptical shapes [76][168]. However, in the real case scenario, every tumor is of different size and shape and may require a specific MNP dose and injection sites for an optimum therapeutic effect during MNPH. So, in this chapter, the tumor models of different shapes and sizes, based on the patient-specific DICOM (Digital Imaging and Communication in Medicine) image data, have been used to construct the physical models [85], [86]. Through the MNPH simulations, the effects of tumor shape, size, and MNP injection strategies on the MNP dose (mg of MNP/tissue volume cm^3) for MNPH have been investigated.

It is noticed that, the heat dissipation and its spatial control is highly influenced by the nanoparticle injection location, dose, and distribution pattern [72] inside the tissue. Thus, a precise control of the MNP dose and its distribution in the localized targeted tissue is a key factor for the successful hyperthermia therapy. The heterogeneity in the heat and temperature distribution has been minimized by optimizing the MNP spread using multi-injections strategies for arbitrary shape tumors [22], [70], [76]. However, these computational studies are limited to their simulation in the regular three-dimensional or hypotheical tumor geometries [85][73]. Limited numerical studies have been conducted on the tumor model reconstructed from real patient-specific data for MNPH [85], [86]. However, feasibility studies of microwave, RFA (radiofrequency wave), and ultrasound waves thermal therapies based on DICOM data have been conducted [87], [88]. Therefore, in this work, MNPH has been applied on breast tumors models generated from patient-specific DICOM data using the CT (Computed tomographic) or MRI (Medical resonance imaging) scans. MNPH simulations are performed

on five breast tumor models, which fall into the tumor category ranging from T1 to T4 tumors (based on tumor size) [147].

Since the tumors exist in various shapes and sizes [145], [169], and to have successful treatment, heat energy must be confined only to the tumor region. This heat and its diffusion in the targeted tissue [9,21] depend upon the MNP amount, their spread, the physiology of the tissue, and, the injection strategy to induce the nanoparticle inside the tumor tissue [170]. In general, the injected mass of MNPs should increase as tumor volume increases to induce the required thermal dose. However, quantifying the optimum MNP mass for a specific tumor that is arbitrary in shape and size tumor is challenging. Therefore, the effects of tumor shape, size, and MNP injections on the MNP dose (mg of MNP/tissue volume cm^3) for magnetic nano-particle hyperthermia have been investigated in this study. In this work, a thermal damage criterion i.e., at least 90 % of the tumor volume and, less than 10% of healthy tissue volume should be under apoptosis [72], [171], is considered for calculating the required MNP dose. Additionally, both injection strategies (single as well as multi-points) are used to deliver the MNP dose to the tumor models. The simulations are done by using a fixed MNP dose of $5\ mg/(cm^3$ of tumor tissue) [72] as well as variable reducing dose [172] ranging from 5.5 to 2.8 mg MNP/ cm^3 to the tumor models.

For the shake of nomenclature, the fixed MNP dose is designated as constant dose *(CD),* and the variable MNP dose is called reduced dose *(RD)* in this work. The MNPH is simulated on these tumor modes using a finite element method in COMSOL software. The study indicates that as the tumor volume increases, the requirement of MNP dose (mg of MNP/tumor volume) decreases to achieve the required therapeutic effect. The MNP dose (mg/cm^3) almost drops by 50% if the tumor volume increases five times from the T1 to T4 type of the breast models.

4.2 Materials and methods

4.2.1 Physical tumor modal

The geometrical tumor models for breast tumors are reconstructed from the data of the public repository service, 'The Cancer Imaging Archive' (TCIA) [173], a part of the national cancer research (NCI), United States. The DCE_MRI DICOM images of breast cancer having different sizes (in terms of tumor volume) have been extracted from the archive. The geometrical breast models of various shapes and sizes are generated from these magnetic resonance images (MRI) using open-source 3d Slicer software, referred to as Brigham and Women's Hospital (BWH), Inc. [174]. This software is routinely used for medical image

informatics and analysis [175], [176]. A volume and region of interest (ROI) are obtained from pre and post-contrast MRI images by subtraction scaler volume mapping and volume rendering, as shown in Figure 4.1 (a-d).

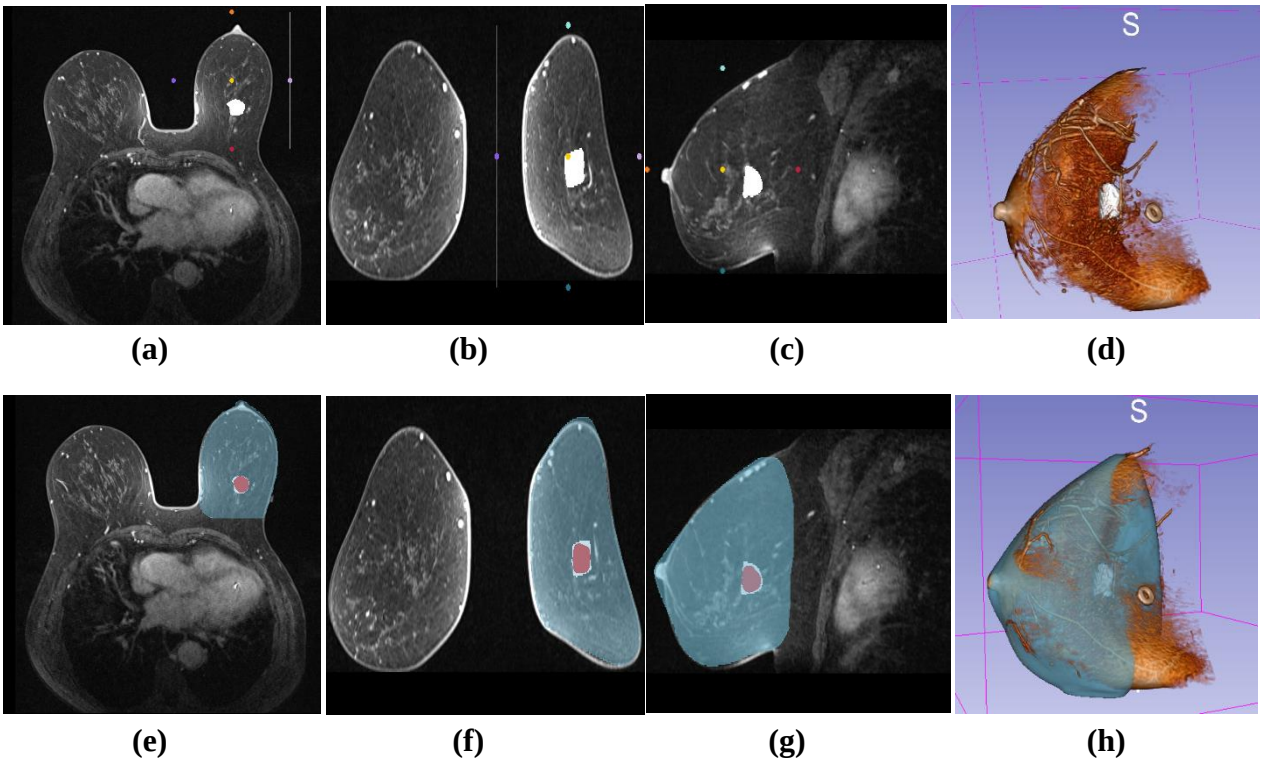

Figure 4.1: MRI images in 3D slicer in (a) Axial (b) Coronal (c) Sagittal, planes, and (d) ROI in 3D slicer. Figure (e-h) shows a manual segmentation of ROI through surface cut**.**

The ROI is further converted into a closed surface geometry with the help of the segment editor tool of the 3D Slicer. After that, the segments (3D tumor model) are exported to the COMSOL software in STL (stereo lithographic) file format. These models are simulated using COMSOL to apply the bioheat physics according to the sequence shown in Figure 4.2. The tumor model constitutes a homogeneous healthy tissue surrounding the tumor tissue. The breast's major portion comprises mammary gland lobes, and 70-80 % of breast cancer develops in the mammary gland (ductal carcinoma and lobular carcinoma) [177]. So, the thermo-physical parameters of the gland have been considered for healthy tissue properties.

A physical breast model is shown in Figure 4.3 ($\bar{a}$), corresponds to one of the extracted breast models with its thermal boundary conditions. Five tumor models of different sizes and shapes are shown in Figure 4.3 (a-e). The tumor size in the first model (Figure 4.3(a)) is around 3 cm^3, and the maximum tumor size is about 15 cm^3 for the 5^{th} model (Figure 4.3e).

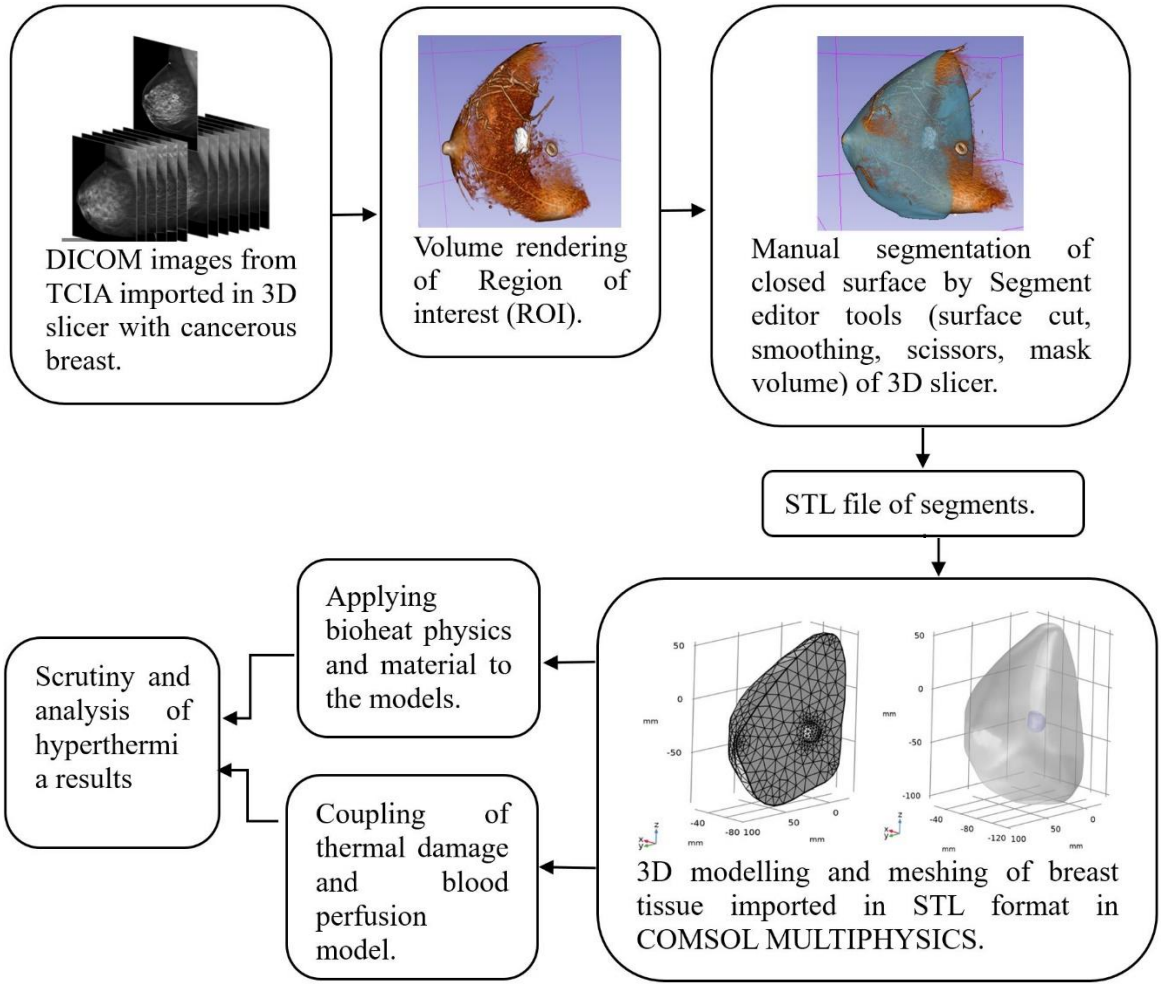

Figure 4.2: Procedural steps for tissue segmentation in 3D slicer, followed by the modelling of imported models in COMSOL software.

These models fall into the size category of T1-T4 according to the tumor-node-metastasis (TNM) breast cancer classification [147]. The size of these tumors are parameterized in terms of their volume and surface area. Table 4.1, enlists the volume and surface area of the tumor tissue as well as the healthy tissue of the tumor models considered in this study.

Table 4.1: Statistics of different tumor models extracted for hyperthermia application [173]

Models	**Tumor Tissue**			**Breast tissue**	
	Catagory	Volume (cm^3)	Surface Area (cm^2)	Volume (cm^3)	Surface Area (cm^2)
1st	T1	3.07	10.5	811	453
2nd	T2	5.92	16.6	1399	636
3rd	T3	8.56	21.9	957	478
4th	T3	12	27.9	1114	547
5th	T4	15	31.0	888	462

It should be noted from Table 4.1 that the volume of tumor tissue increases five times for the 5th model with respect to the 1st tumor model. However, the surface area of the 5th model is increased to nearly three times with respect to the smallest tumor. Furthermore, since the data is from different patients, thus the breast tissue size (volume & surface area) also varies for these models.

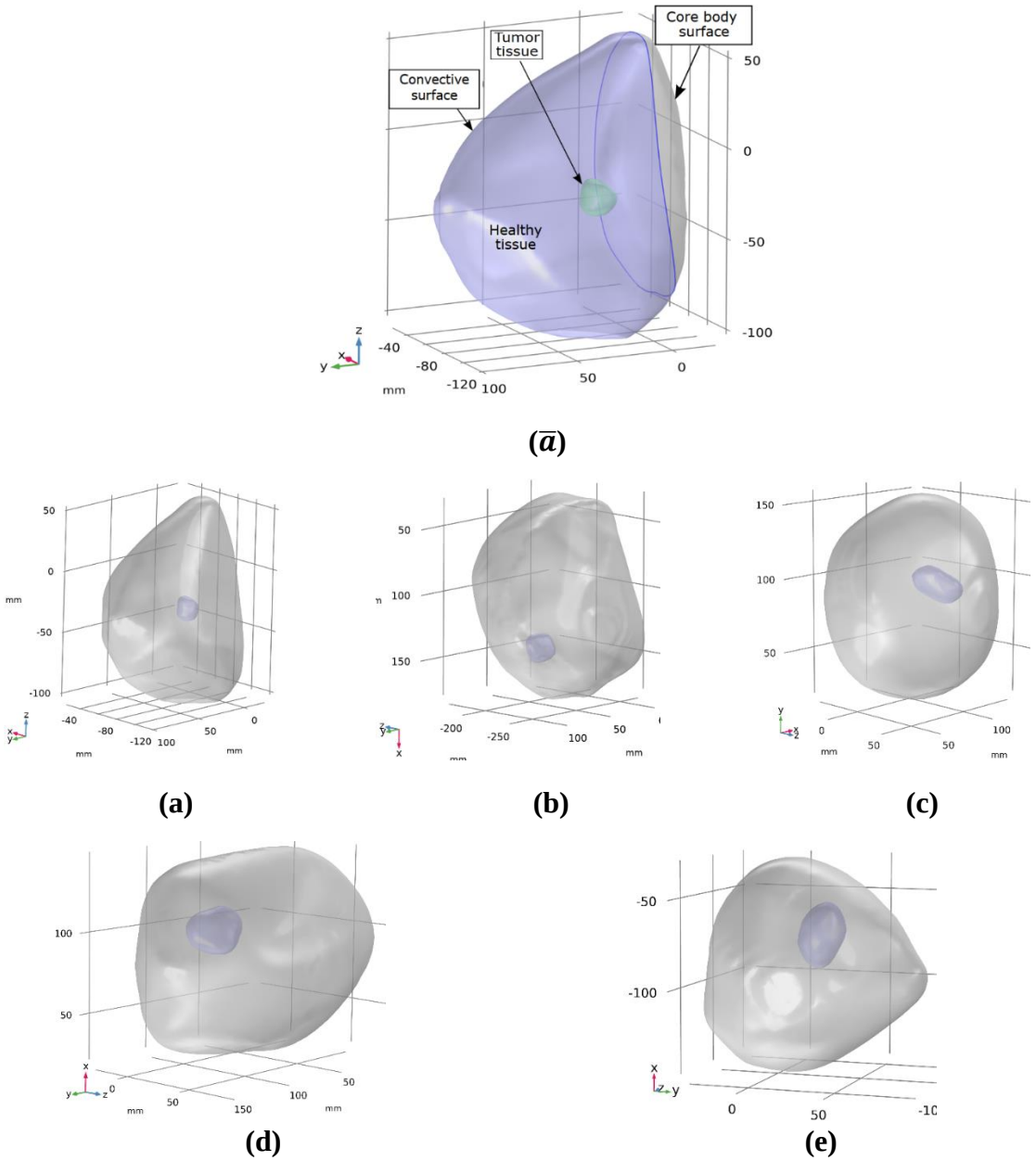

Figure 4.3: (*a*) Schematic of Breast physical model geometry, tumor region surrounded by healthy tissue, with its thermal boundaries. Developed physical models in COMSOL, imported in STL format from the segmentation editor of the 3D slicer shown by Figs. (a-e)

In this regard, Table 4.1 shows the statistics of these breast models with tumor and healthy tissue that comes under the T1-T4 breast cancer stages according to the tumor-node-metastasis (TNM) classification system for breast cancer staging [147].

4.2.2 Mathematical model

The MNH is simulated in all the tumor models discussed in the previous section. The temperature simulation in the tumor and the healthy tissue during MNH has been done using Penne's bio-heat model [153]. The general mathematical form of Penne's bioheat equation has been presented by Eq. (3.2) in the section 3.3 of previous chapter 3. The tissue and material properties considered in the present study have been provided in Table 4.2.

Table 4.2: Thermo-physical properties of tumor and healthy tissue included in the study for simulation [86][178][179].

Properties	**Tumor**	**Healthy region**	**Blood**
Density, ρ (kg/m^3)	1050	1041	1050
Thermal conductivity, k_t W/(m.K)	0.48	0.33	NA
Specific heat, c_p (J/(kg.K))	3770	2960	3617
Perfusion rate η_b (1/s)	0.011	0.005	NA
Metabolic heat, Q_m (W/m^3)	13600	700	NA

4.2.2.1 Heating power, and thermal damage criteria.

The heat source term Q_s in Eq. (3.2), is the power deposition in tissue dependent on the applied amplitude and frequency of alternating magnetic field (AMF). The remaining details of heat generation are explained in the section 2.2.2 from Eq. (2.1 to 2.4) of the previous chapter 2. When iron-based nanoparticles (MNP) are exposed to the AMF, a magnetically induced heat is generated and is termed specific loss power (SLP) [180]. The Q_s in W/m^3 is obtained by the product of SLP in (W/g) and MNP concentration or dose having unit (mg/cm^3) in the tissue. In the current study, a constant heating power (SLP) of 50 W/g corresponding to the field amplitude (H_0) of 10 kA/m and 150 kHz of frequency (f) has been considered. This value is calculated from the relation given for SLP calculation observed for BNF-Starch nanoparticles of size around 100 nm used by Attluri.et [71], [74], [181].

Here, the considered values of field frequency and amplitude in multiplication remain under the acceptable threshold limit, i.e., $4.85\times10^{8}\,\mathrm{A/m.s}$ for the safe application of MNH [74][158]. The heat distribution in the tissue is also affected by MNP distribution. Thus, the distribution of Q_s in the targeted tumor tissue will be different for single and multi-injection MNP distribution. The effect of heating in the tissues (tumor and healthy) has been calculated in terms of thermal dosimetry (Thermal damage). Thermal damage to the tissue is calculated using the Arrhenius relation that has been given by Eq. (3.11) in the section 3.3.4 of the previous chapter 3.

The thermal damage parameter denoted by $'\Omega'$ with a threshold value of 4.6, which corresponds to 99 % of cell damage, has been considered in the current simulation. Furthermore, temperature-dependent blood perfusion (η_b) within the tumour and the healthy region is implemented using the first-order irreversible kinetic Arrhenius model which is well describes in the section 3.3.5 of chapter 3. The (η_b) as having a linear relationship with a non-dimensional parameter, called the degree of microvascular stasis (MVS) (Eq. 3.15 & 3.16), which is a function of the thermal damage parameter (Ω) is well elaborated by S Nain et al. [178]. This study considers medium blood perfusion (η_b), which is 0.011 s^{-1} for the breast tumor tissue and 0.55×10^{-3} s^{-1} for the healthy tissue [156].

The cumulative thermal damage of tumor as well as healthy tissue is defined by a parameter C_d that quantifies in terms of volumetric percentage damage [76] of any tissue relative to the tumor volume. This parameter C_d has been calculated using Eq. (3.13) given in the section 3.3.4 of the previous chapter 3. Here, the thermal damage parameter represents the tissue volume having the value of $\Omega \geq 4.6$, (Eq. (3.11)) for each damaged cell.

4.2.2.2 Boundary Conditions (BC's) on the tumor models.

The tumor models in the current study are of the three-dimensional volume enclosed by different surfaces. The first is the outer surface (skin), which interacts with ambient conditions through convection, and the other is the surface attached to the core body. There is a third surface in this model, which is the interface of tumor and tissue. The boundary conditions applied on these respective surfaces of the physical breast model are shown in Figure 4.3 ($\bar{a}$). The interface boundary surface (tumor-healthy tissue) is tackled by the continuity equation given in Eq. (4.4). The convective surface of the geometric modal is liberating heat by convection (Eq. (4.5)) to the ambient, at a temperature of 20 ˚C. Moreover, the core body

temperature, i.e., 37 ˚C, is assumed at the interface of the breast and the core body surface (Eq. (4.6)). The mathematical form of all BC's are as follows,

$$-k_{t.t.}\frac{\partial T(0,t)}{\partial(x,y,z)} = -k_{ht.}\frac{\partial T(0,t)}{\partial(x,y,z)} \tag{4.4}$$

$$-k_{ht}\frac{\partial T(0,t)}{\partial(x,y,z)}\Big|_{CS} = h_c(T_{CS} - T_{amb}) \tag{4.5}$$

$$T_{CBS} = T_c \tag{4.6}$$

4.2.2.3 Numerical Simulation and Grid structure

Physics-controlled tetrahedral mesh elements are used to discretize the computational domain (tumor model). It should be noted from the meshing of all the tumor models (Figure 4.4) that the tetrahedral elements are fine in the tumor tissue and at the tumor and healthy tissue interface.

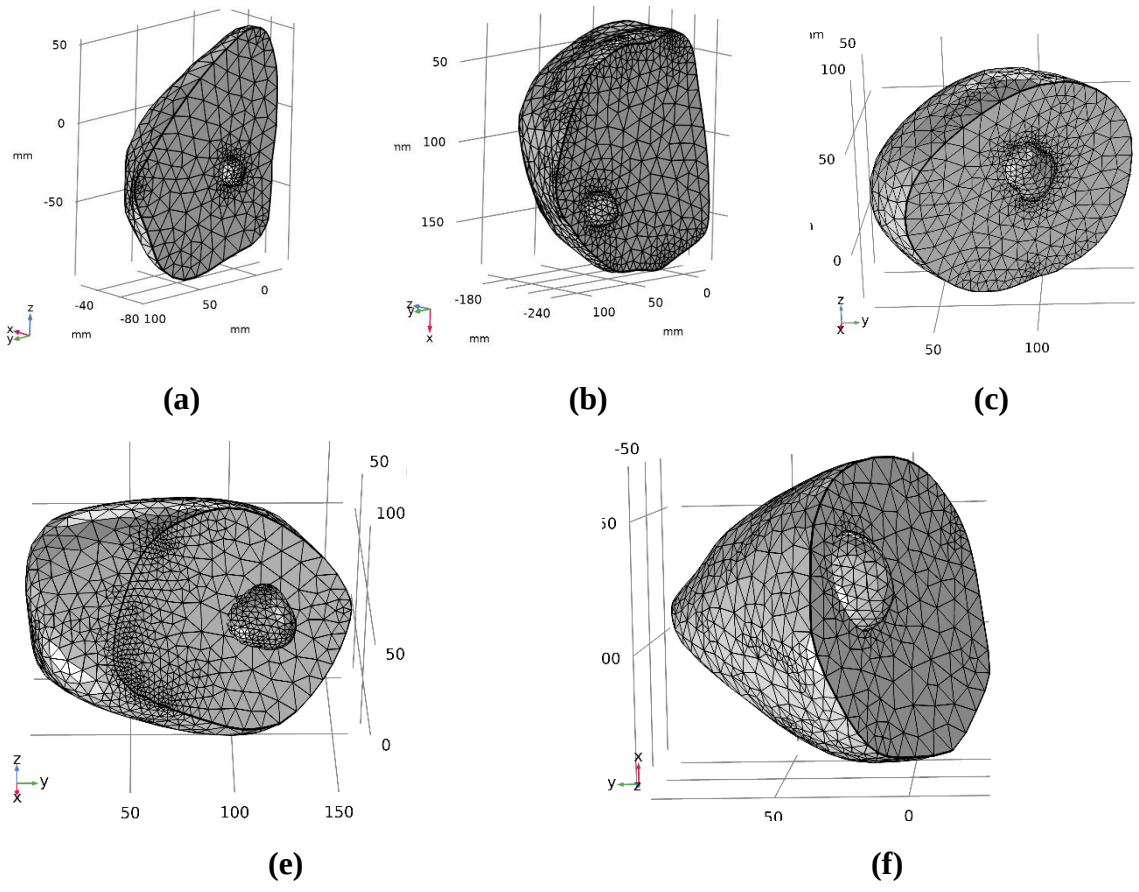

Figure 4.4. Sectional view of different breast models having discrete nodes and mesh generation.

Heat generation and its transport primarily occur in the tumor tissue, where the MNPs are concentrated. Thus, meshes are fine in the tumor tissue to capture the stiff temperature gradient in this volume. The temperature gradient is less in the outer healthy tissue away from the heat-generating domain. Thus, a coarser mesh is utilized in this region. Repair tolerance of $1e^{-8}$ at geometrical interfaces have been applied for the smooth application of boundary conditions and physics.

The unstructured tetrahedral grid elements used for the MNH simulation are shown in Figure 4.4. Generally, the computational results are sensitive to the grid type and size. Thus, a grid refinement test has been performed to assess the independency of computational results. This test is conducted on the smallest tumor (model 1st). The mesh is consecutively refined for each hyperthermia simulation on this model. The highest temperature attained during magnetic hyperthermia on this model is observed with different mesh sizes. It should be noted from Table 4.3 the deviation of the results is nearly 0.19 % for the elements 535431 and 115050, utilized for the simulation. Thus, 535431 number of elements is reasonable for 1st tumor model. A similar grid-independent test is also conducted for other models to estimate the required number of mesh elements for each model.

The numerical integrity of the current study has been done by comparing the computational and the experimental results. The temperature profile of an in-vivo mice study done by Attaluri [48] is selected to demonstrate the validation of the current study. The tumor is dosed with 25.17 mg mass of magnetic nanoparticle distributed in a volume of 60 (mm^3) and exposed to150 kHz and 6 kA/m frequency and amplitude of alternating magnetic field [48]. The combination of this filed and frequency develops a SLP (specific loss power) of 9.5 w/g, which has been used to predict temperature profile in the current study.

Table 4.3: Grid independence test for on 1st breast model (Maximum temperature in tumor tissue after one hour).

Number of tetrahedral elements	The maximum temperature at the tumor center (˚C)	Deviation (%)
18219	60.6	-
39930	60.0	1.0
115050	59.75	0.38
535431	59.87	0.19

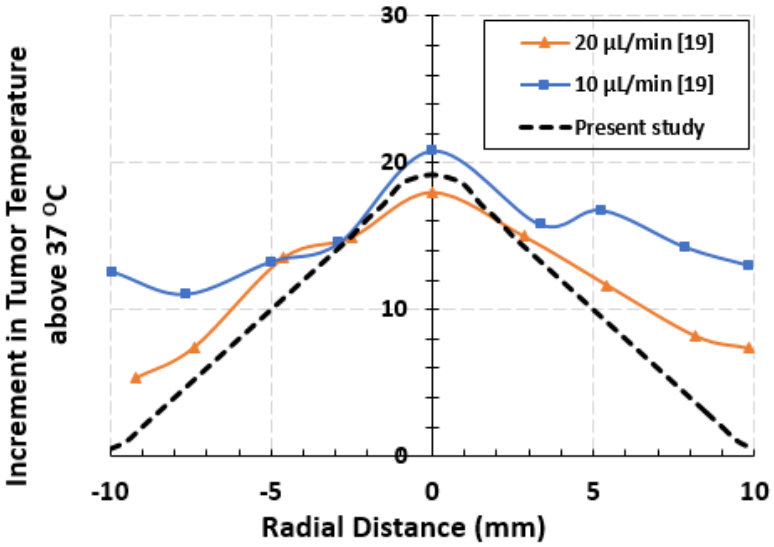

Figure 4.5. Comparison of the spatial temperature profile of tumor region between experimental [48] and the present study.

The temperature profile measured by a thermocouple in an experimental study is obtained at an infusion rate of 10 µL/min of MNP fluid to the tumor region. In Figure 4.5, the abscissa is a radial distance on both side of the injection point and the temperature is on ordinate, whose base temperature value i.e., 0 ˚C is equal to 37 ˚C. The MNP spread has been considered uniform inside the tumor in the same volume as done in the experiment by Attaluri et al [48]. Due to the heterogeneous MNP distribution in the experimental study, there is a difference between temperature profile that can be noticed in Figure 4.5. However, a close agreement has been found in the overall curvature of temperature distribution along the central axis of the computational domain and the experimental results.

4.2.2.4 MNP's injection dose methodology and their distribution in the tumor models:

As mentioned in the introduction, MNP produce heat under AMF to sensitize or ablate the tumor tissue. The heat spread and dissipation is influenced by the MNP distribution that depends upon the injection rate as well as the physiology of the tumor. However, to simulate the MNH, various theoretical studies have simplified the MNP spread with reasonable assumptions [49], [70]. And primarily, two types of MNP concentration distribution, either uniform or uniformly varying MNP distribution (Gaussian) are considered [76], [85]. Attaluri *et al*. [71] in their work have considered that the MNP is uniformly concentrated only in 40% of the tumor. Similarly, Kandala *et al.* [72] have considered three types of MNP distribution in elliptical-shaped tumors. Uniform distribution in the complete tumor, uniformly concentrated only in 40% of the tumor, and Gaussian distribution in tumor tissue. Again, for

the Gaussian, the MNPs are spread up to 44% of the major tumor axis and 17% of the minor tumor axis. Thus considering the approximations and simplifications stated in the previous works [71], [74], a uniformly concentrated MNP distribution has been assumed around the injection point. The details of the MNP dispersion after its injection in the tumor tissue are illustrated in Table 4.4. It should be noted from this table that for a single injection, the spread of MNP slightly increases from 35% to 43% of the tumor volume as tumor size increases (1^{st} to 5^{th} Model). This increase in the MNP dispersion accommodates higher MNP mass injected into the bigger tumors. For multi-injection, the total tumor volume has been divided according to the number of injection sites used in the multi-point MNP delivery. For the multi-injection approach, MNP mass injected through each injection depends upon the percentage of the tumor volume covered by specific injection. Since the tumors are complex in shape and may have multiple protrusions, thus total tumor volume is suitably divided to locate the injection points for multi-injection strategy. The respective MNP's mass for each injection depends upon the tumor volume weightage that injection covers. Again, the number of injection points depends upon the tumor shape's complexity and the tumor volume. Thus 1^{st}, 2^{nd} and 5^{th} tumor model has two injection points, however $3^{rd,}$ and 4^{th} tumor model has three injection points, respectively. Table 4.4, also depicts the percentage tumor volume associated with each injection point and the percentage tumor volume covered by MNP dispersion for each injection. In the multi-injection strategy, MNP mass is divided into multiple sites. Thus, the MNP spread volume at each site in multi-injection is smaller than the MNP dispersion volume due to the single-injection strategy.

As discussed in the introduction, quantifying the MNP dose that produced the required therapeutic effects is difficult to estimate. Although some efforts have been made in the literature related to MNP dose for increasing size tumors [172]. To investigate this aspect, numerical experiments are conducted in this work to evaluate the therapeutic effects in terms of thermal damage, induced by constant dose (*CD*) and reduced dose (*RD*) methodology, whose implementation is shown in the flow chart of Figure 4.6.

Thus, in all the generated tumor models (1^{st}-5^{th}) constant dose of $5\ mg/cm^3$ is injected through the single-site injection with the spread of MNP, as described in Table 4.4. Magnetic hyperthermia is simulated on these models for one hour using magnetic field parameters described in section 4.2.2.1. The computational results produce elevated spatial temperature profiles in and around the targeted tumor tissue volume.

Flow chart of optimum MNP dose implementation

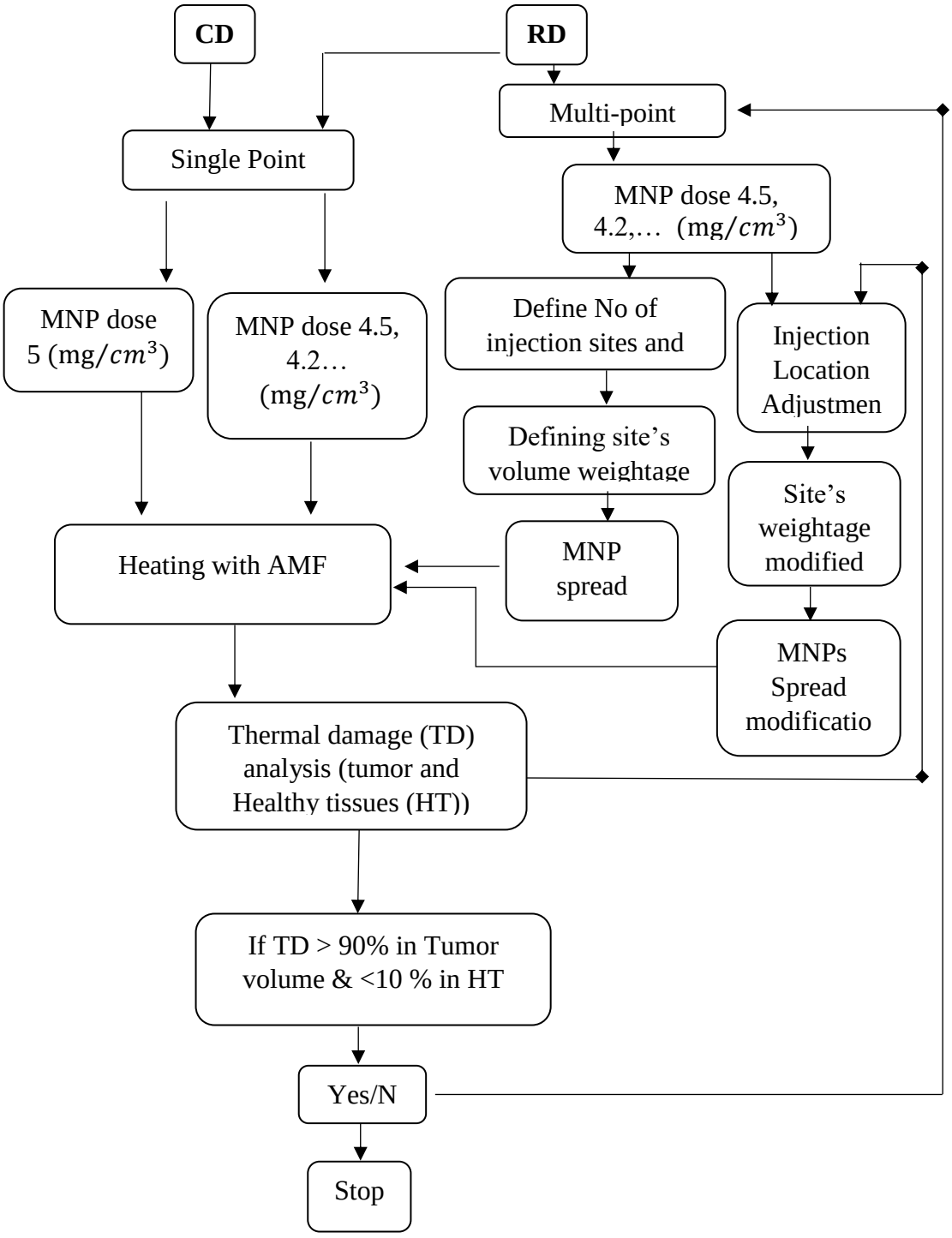

Figure 4.6: Procedural steps of implementation of constant and reduced dose methodology and different parameters arrangement.

Table 4.4: The tumor models with implemented injection protocol having centrally concentrated MNP distribution in allotted volume weightage in single-site (*CD & RD*) and multi-site injections (*RD*).

Models	Single-site injection		Multi-site injection	
	MNP distribution	MNP dispersion in Tumor volume (%)	MNP distribution	Site's tumor volume weightage (%) and spread in tumor volume (%)
1st	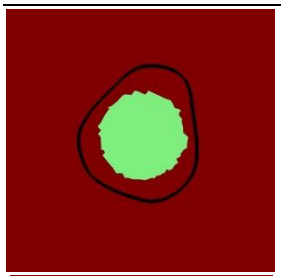	35	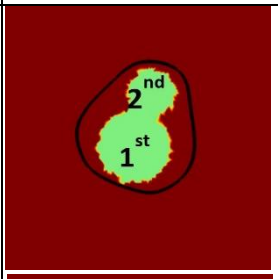	1st – 68, 35 2nd – 32, 25
2nd	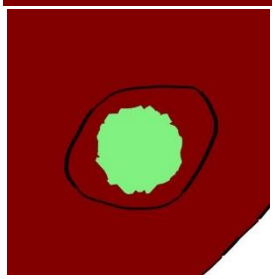	35	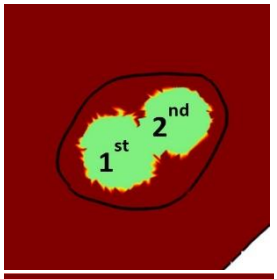	1st – 60, 35 2nd – 40, 35
3rd	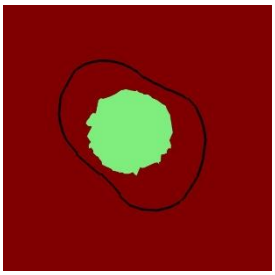	35	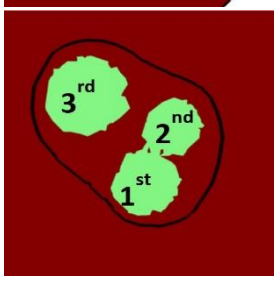	1st – 31, 25 2nd – 22, 25 3rd – 47, 32
4th	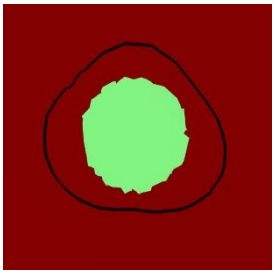	40	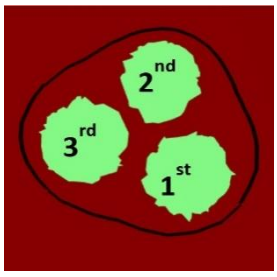	1st – 35, 25 2nd – 30, 25 3rd – 35, 25
5th	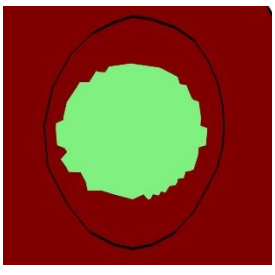	43	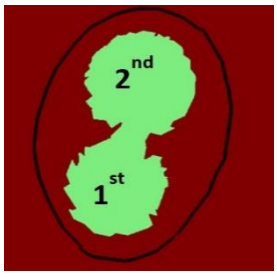	1st – 47, 28 2nd – 53, 30

The therapeutic effects in terms of thermal damage, C_d (Eq. (3.13)), are computed using this spatiotemporal temperature profile created during MNH. The thermal damage induced by

MNH with constant dose (*CD*) of MNP to all selected tumor models (1^{st}-5^{th}) is shown in Figure 4.7 (a-e). In these figures, the tumor-healthy tissue boundary is inscribed with white color. It can be seen from these figures thermal damage is within the tumor boundary only for the smallest tumor (1^{st} model).

However, as the tumor size increase, more thermal damage is inflicted to the healthy tissue (Figure 4.7 (b-e)). With these findings, it can be concluded that *CD* of MNPs (5 mg/cm^3) is not suitable for different sizes of tumors. Because *CD* of MNPs damages more healthy tissue volume in larger tumors during hyperthermia, thus the MNP dose must decrease as tumor size grow. Again, numerical experiments are conducted to optimize MNP dose for different shapes and tumor models. The MNP dose for the tumor models (2-5) is iteratively reduced until the thermal damage criterion, discussed in the previous section is obtained [72], [171]. Based on these numerical simulations, a reduced dose (*RD*) of MNP is estimated for all the tumors selected in this study.

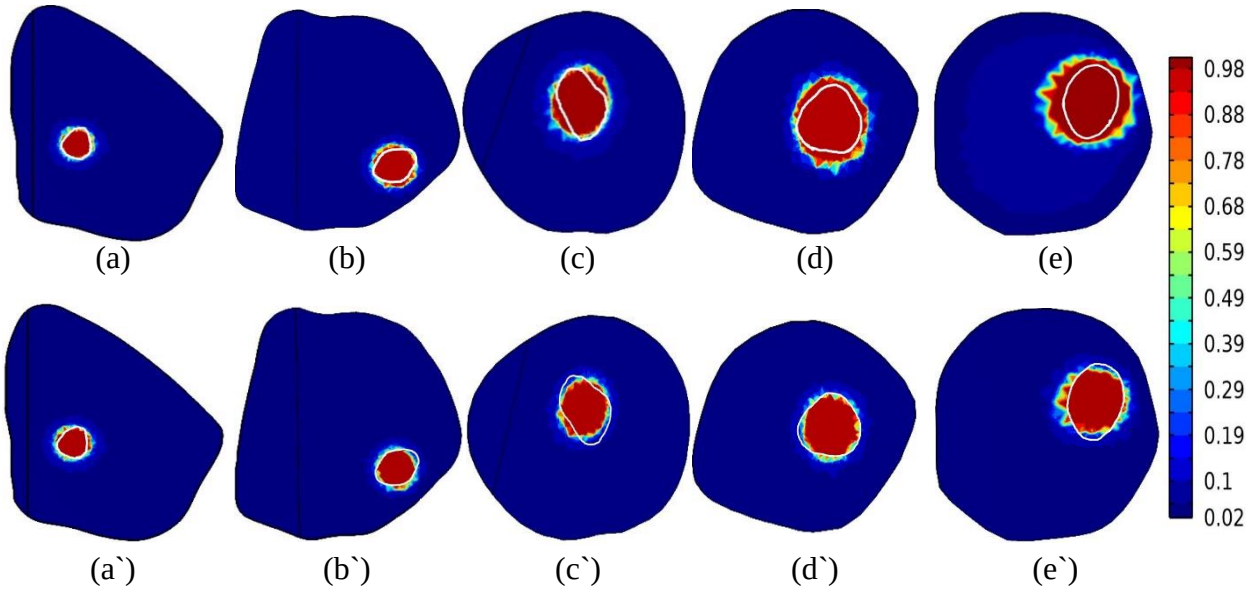

Figure 4.7. Comparison of thermal damage to the targeted tissue and surrounding healthy tissue having *CD* (a-e), and RD in Figure (a`-e`)

The numerical values for reduced MNP dose corresponding to each tumor is depicted in Table 4.5: Tumor models and their respective injected MNP dose with *CD*, and *RD* method. It should be noted from this table, the required MNP dose for the smallest tumor is slightly higher than 5 mg/cm^3 i.e. 5.5 mg/cm^3 to induce needed therapeutic effects during MNPH. However, for

the tumor models 2nd to 5th, as the tumor size increases, the MNP dose is continuously reduced to get the required therapeutic effects.

The thermal damage induced by the *RD* during MNPH on all the tumors is also shown in Figure 4.7 (a`- e`). Thus Figure 4.7, compares the thermal damage inflicted to the tumor as well as healthy tissue with *CD* and *RD* during MNPH. It should be noted from this figure that, *RD* induced much smaller damage to the healthy tissue, even for the biggest tumor (model 5th) in comparison to the *CD* MNP dose. Thus, MNP dose should be reduced as the tumor size increases to induce the required therapeutic effects during MNPH. The details of the investigation using single-point and multi-point injection strategy for constant MNP dose and reduced MNP dose is described in the result section.

4.3 Results

The details of MNH simulation results using constant and reduced MNP doses with single and multi-injection MNP delivery are discussed in this section. The MNH thermotherapy is induced in all tumor models, (Figure 4.3). The duration of MNH therapy is 3600 seconds for all the breast models [164]. The temperature in the targeted tissues starts rising as soon as the MNH applicator is induced.

4.3.1 The steady-state spatial distribution of the temperature during MNH

The steady-state spatial temperature distribution in the form of isotherms for MNP doses (*CD*, and *RD*) and injection methodology for all the breast models selected in this study are discussed in this section. We have categorized MNH into three categories based on the MNP dose (*CD* and *RD*) and its injection methodologies (single and multi-injection). These are single injection with constant MNP dose; single injection with reduced MNP dose; and multi injection with reduced MNP dose. It should be noted that *RD* of MNP for each tumor model, as mentioned in Table 4.5, is the same for single and multi-injection MNP delivery.

Thus, for reduced dose protocol, similar MNP mass is injected into a specific tumor irrespective of whether it is delivered through single or multi-injections. The MNH is intended to maintain at least 90% of the tumor tissue at a target temperature of 43 ˚C. The temperature assessment is compared by T_{90} and T_{10} (temperature achieved in at least 90% and 10% tumor volume), and a heterogeneity index (HI), which is defined as $(T_{10} - T_{90}/(T_{90} - T_{CB})$ [76]. Table 4.6

shows the statistical details of the temperature induced during MNH in the breast tumor tissue subjected to different injection strategies and the MNP dosages.

Table 4.5: Tumor models and their respective injected MNP dose with *CD*, and *RD* method

Models	Tumor Volume (cm^3)	**Constant dose (*CD*)**		**Reduced dose (*RD*)**	
		Injected MNP dose (mg/cm^3)	Total MNPs mass (mg)	Injected MNP dose (mg/cm^3)	Total MNPs mass (mg)
1st	3.07	5	15.35	5.5	16.88
2nd	5.91	5	29.55	4.2	24.83
3rd	8.65	5	43.25	3.6	31.57
4th	12.02	5	60.1	3.2	38.46
5th	14.8	5	74	2.8	41.44

It should be noted from Table 4.6, that when the tumors are injected with a constant dose (*CD*), i.e., of 5 $mg/cm^3$of MNPs, the T_{90}, T_{10}, and T_{max} temperature increases with the increase of the size of tumor. This is due to the increase in the total mass of MNPs being injected as tumor volume increases. This increase in the MNP mass is in proportion to the tumor size as given in Table 4.5. On the contrary, with the reduced doses (*RD*) of MNPs, the pointers of therapeutic temperatures (T_{90}, T_{10}, and T_{max}) have not been proportionally increased with tumor volume increment.

Table 4.6: The temperature achieved in the tumor region of all physical models subjected to different injection and MNP dosage strategies.

	Tumor Temperature (˚C)											
	T_{90}			**T_{10}**			**T_{max}**			**HI**		
Tumor Models	*CD-Single-point*	*RD-Single-point*	*RD-Multi-point*	*CD-Single-point*	*RD-Single point*	*RD-Multi-point*	*CD-Single-point*	*RD-Single point*	*RD-Multi-point*	*CD-Single-point*	*RD-Single point*	*RD-Multi-point*
1st	42.4	43.5	44.3	54.2	56.4	56.25	59	61.5	60.5	2.1	1.98	1.66
2nd	45.5	43.2	43.9	64.8	59.5	58.0	71.5	65.2	63.9	2.27	2.6	2.0
3rd	44.5	40.7	43.8	72.3	61.3	55.9	81	67.7	60.3	3.7	5.5	1.77
4th	50.1	42.6	44.5	80	62.3	57.7	89.6	68.4	62.5	2.28	3.5	1.76
5th	52.3	41.7	44.3	85	62.1	61.0	98.5	68.3	67.9	2.3	4.3	2.2

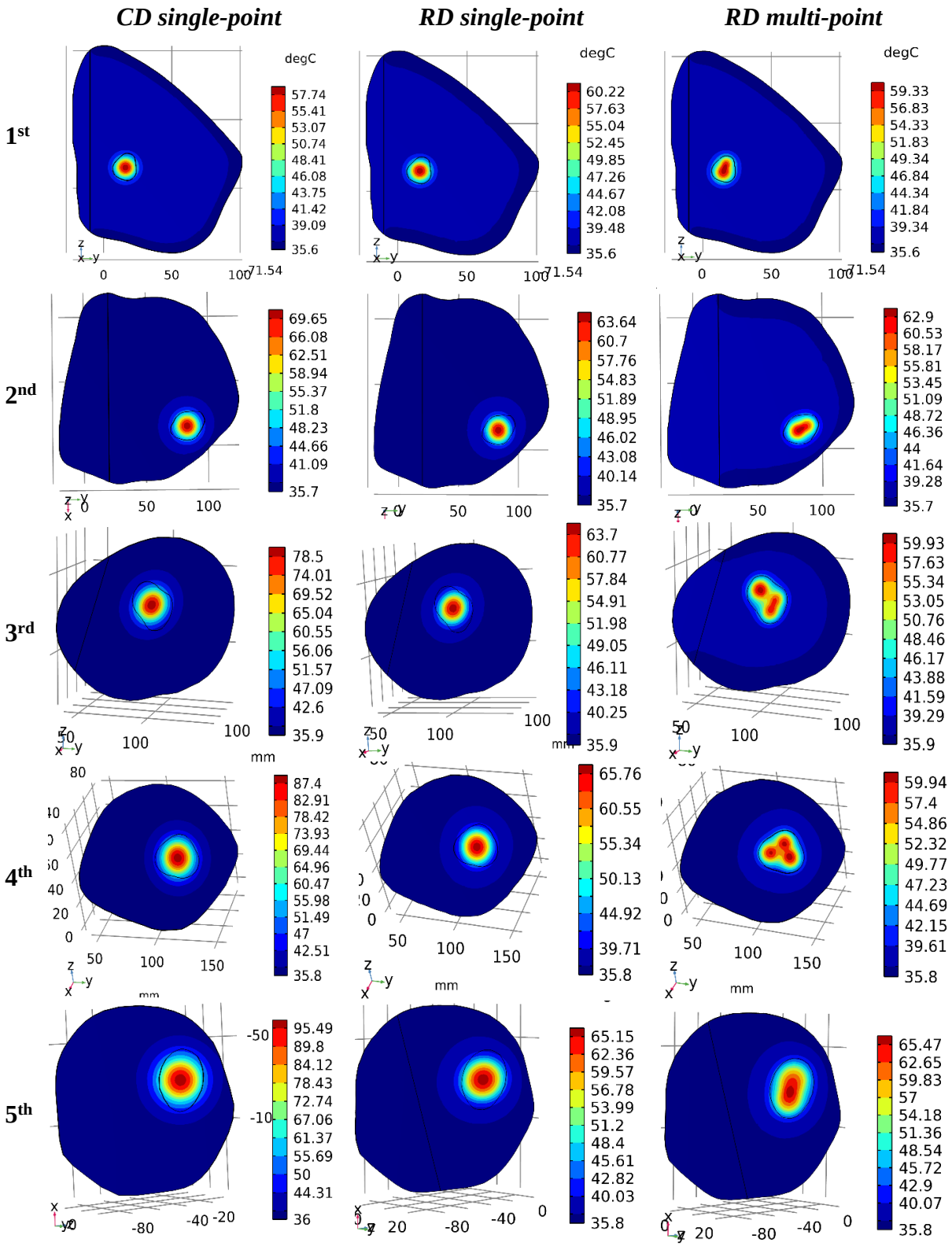

Figure 4.8. The contours of the temperature distribution of all five breast models in tumor tissue and healthy tissue infused with constant dose (*CD*), and reduced dose (*RD*), after one hour of heating. ***Column*** 1st have the *CD* single-point injection, ***Column 2nd*** represents the *RD* single-point injection at the centroid of tumor volume, and ***Column 3rd*** shows the *RD* multi-point injection strategy implemented in models.

It should be noted from Table 4.6. that with reduced dose (*RD*), T_{90} the temperature in the tumor mass is reduced with a single injection. However, with multi-injection delivery, the temperature T_{90} in the tumor volume remains closer to the therapeutic level, i.e., 43 ˚C. Thus, *RD* and multi-point injection strategy exhibits the temperature above the minimum therapeutic level, i.e., 43 ˚C, and cover at least 90% of tumor volume in all five models. The maximum temperature T_{max}, induced with *RD* and multi-injection strategy, is also much lower than the *CD* and single-injection strategy. In addition, *RD* with multi-injection has lesser heterogeneity in the temperature distribution among the considered dosage protocols.

Conclusively, the multi-point *RD* strategy shows better temperature distribution with significantly less temperature heterogeneity than the *CD* and *RD* single-point injection strategies. The temperature distribution inside the models generated during MNH with single-point and multi-point injection strategies with constant dose and reduced dose protocols have been compared, as shown in Figure 4.8. The color legends show the temperature range, with different colors and starting at core body temperature and rising to the maximum temperature reached inside the tumor after heating. The black line in these planer views is the tumor boundary that separates the healthy and tumor tissues.

It is noticed that contour lines are well merged and seem parallel to the tumor boundary, especially in the multi-site injection. Moreover, the maximum temperature in the multi-point injection is significantly lower than in the single-site injection. Overall, the results of multi-injection strategies have less heterogeneity in the temperature distribution inside the tumor region for all the considered tumors.

The details of the temperature profile obtained during MNH simulations on the considered tumor models have been discussed in the previous section. However, the quantitative therapeutic effects are also estimated in terms of thermal damage (C_d) induced during magnetic hyperthermia. The values of C_d, are estimated for both tumors as well as healthy tissue during MNPH. Details of the thermal damage induced on the considered tumors with different doses and injection strategies are as follow.

4.3.2 Thermal damage to the considered models during MNH with different injection strategies and doses

Ideally, there should be no damage to the healthy region during MNH, but due to the irregular shape and size of the tumor boundary, it's difficult to limit the heat distribution in the tumor

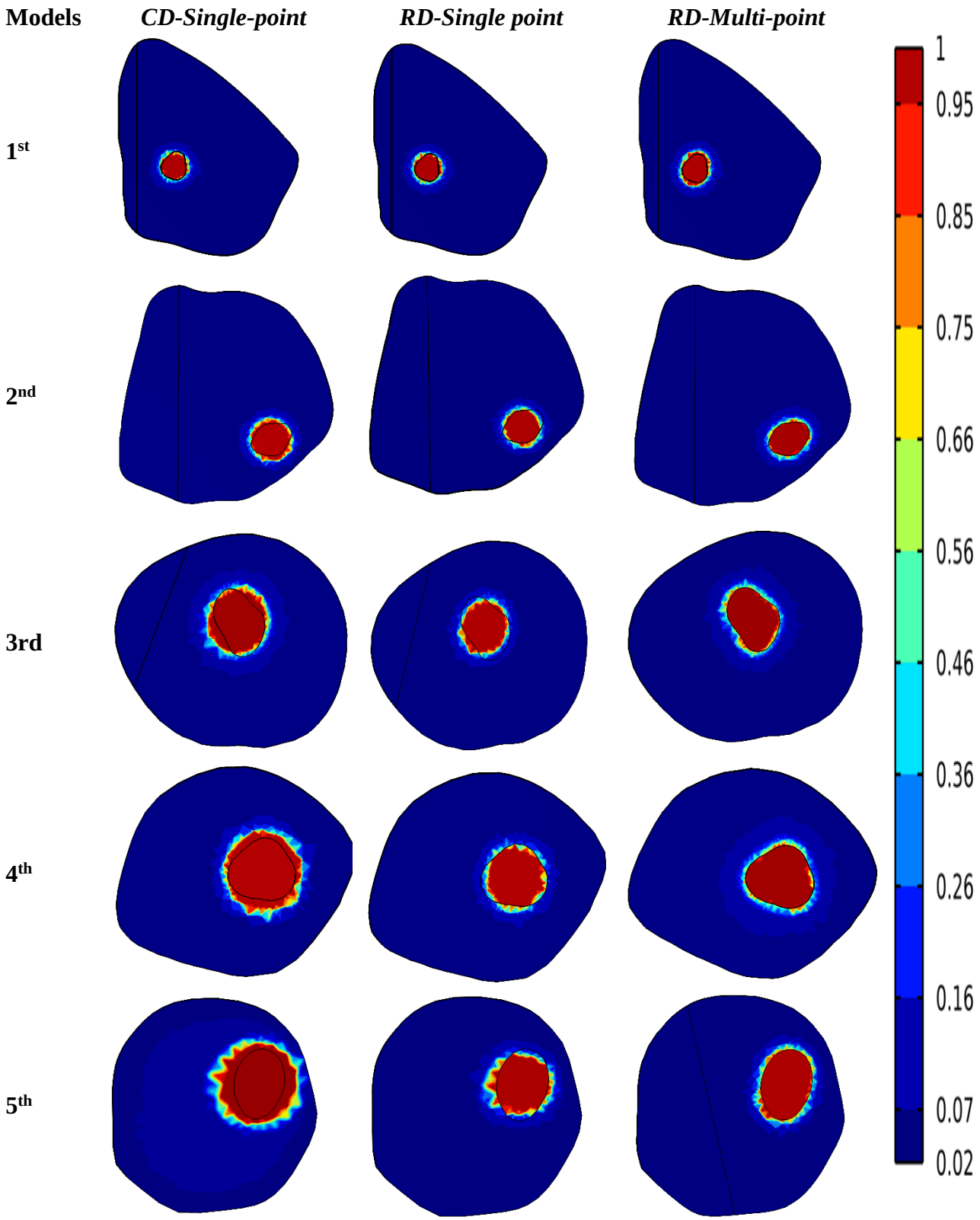

Figure 4.9. Fraction of tissue thermal damage *(MVS)* in the form of isotherms, achieved in the considered models (healthy and tumor region). MNPs are injected with a constant dose single point, with reduced dose (*RD*) single point, and *RD* multi-point injection strategy as shown in Columns 2nd, 3rd, and 4th, respectively.

region only. Figure 4.9, shows the level of thermal damage induce in all tumor models by *CD* using single injection, *RD* using single injection, and *RD* with a multi-injection. It should be noted from the figure that with *CD* and single injection, the thermal damage penetrates the healthy tissue. With the increase in the tumor size, more and more thermal damage is inflicted to healthy tissue with a constant dose regime (Figure 4.9). However, reduced dose of MNP, particularly with multi-injection methodology, restricts thermal damage within the tumor tissue boundary. The quantitative description of thermal damage is enlisted in Table 4.7. It should be noted from this table that for *CD* and single-dose regimes, the thermal damage to the healthy tissue in 2nd tumor model onward is much higher with respect to the maximum allowable damage, which is 10% of the tumor tissue volume. Thus, the MNP dose should not be constant as the size of the tumor increases. Therefore, the total mass of MNP should not linearly increase with tumor volume increment. The therapeutic effects induced by *RD* and single injection show the reduction in the thermal damage to the tumor tissue as well as healthy tissue.

It should be further noted from this table reduction in MNP dose with single injection also inflict less damage with respect to the minimum threshold tumor tissue damage i.e. 90% of tumor tissue.

Table 4.7: Percentage volume of tissues (tumor and healthy) damage in considered breast models having different injection protocols.

Breast models		$\%\ volume\ of\ C_d$				
		1st	***2nd***	***3rd***	***4th***	***5th***
Tumor tissue	*CD-Single-point*	73	94.8	90	97	94
	RD-Single-point	86	85.5	74	83	82.6
	RD-Multi-point	94.5	90.0	90.1	92.8	92.2
Healthy tissue	*CD-Single-point*	0.0	48	92	136	164
	RD-Single-point	2.8	16.3	35.8	25.8	11.6
	RD-Multi-point	4.0	9.5	4.4	2.2	0.48

However, when the same reduced MNP dose was injected through multi-injection, the thermal damage attained the required threshold thermal damage in all the tumor models. At the same time, thermal to the healthy tissue also remains less than the threshold criterion of 10%. Thus, thermal damage inflicted by the *RD* is well within the thermal damage criterion prescribed for hyperthermia therapy.

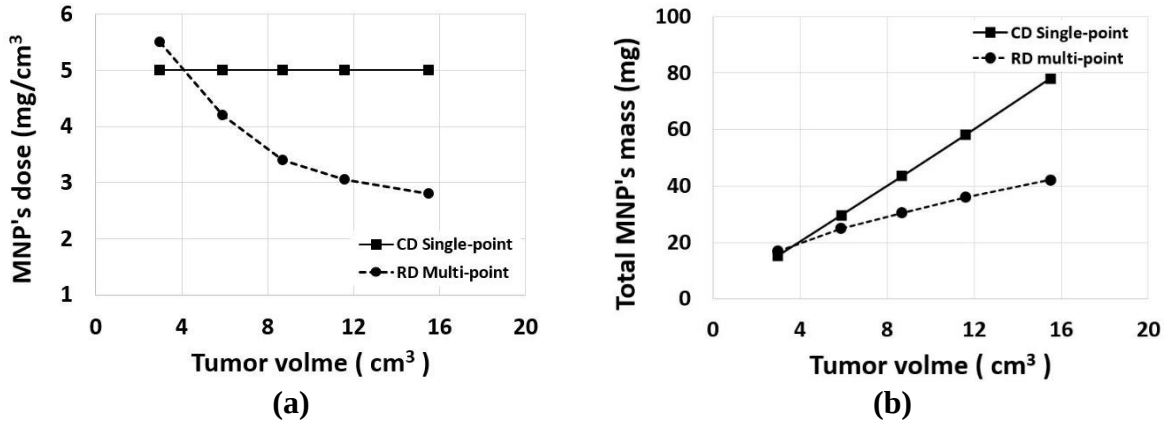

Figure 4.10. (a) Variation of dose of MNPs with different breast tumor volumes **(b)** total MNPs mass being injected under *CD* and *RD* for optimal therapeutic effect.

Figure 4.10, shows the plots of MNP dose (mg of MNP/volume of tumor mass) and total MNP mass injected with *CD* (single injection) and *RD* (multi-point injection) versus tumor volume. It should be noticed from this plot that if the tumor tissue volume increases five times, the optimal MNP dose (mg of MNP/volume of tumor mass) needed for thermo-therapy is dropped by 50%. Among the tested tumors, the maximum size tumor of 15 cm^3, only needs 2.8 mg/cm^3 dose of MNPs to reach a threshold of therapeutic effect. However, the smallest tumor mass (model 1^{st}) having nearly 3 cm^3 tumor tissue volume requires MNP dose of 5.5 mg/cm^3 to attain similar thermal damage. Furthermore, the total MNP mass necessary for the MNH increases with tumor size. However, this increment should not be linear with respect to the tumor size to obtain threshold therapeutic effects. Thus, total injectable MNP reduced from 74 mg to 41.44 mg for the biggest tumor (model 5^{th}) if *RD* is adopted instead of *CD* (Figure 4.10 (b)).

4.4 Discussion and Conclusions:

In this work, efforts have been made to get tumor size-dependent MNP doses for Magnetic hyperthermia therapy. In most of the previous magnetic hyperthermia simulations, the tumors

are considered simple in shape like spherical, elliptical, cylindrical, or cubical [73], [168] However, the actual tumor is usually arbitrary in shape. Thus, tumor models reconstructed from DICOM images enhance the applicability of current work for magnetic hyperthermia therapy. Furthermore, generated tumor models having tumor volumes ranging from $3\,cm^3$ to $15\,cm^3$that covers a wide range of tumor sizes (T1-T4). Thus, estimated MNP dosimetry encompasses a wide range of tumor size. The efficacy of Magnetic hyperthermia largely depends upon the dose of magnetic particles and their distribution in the tumor region. However, various studies have established that multi-point injection strategies help in the homogeneous distribution of MNP in the targeted tissue [22], [70], [76]. Thus, multi-injection delivery of MNP fluid in the targeted tumor volume increases the presence of MNP in a wider tumor mass volume. Therefore, current results also show that less MNP mass is required when MNPs are injected through a multi-injection strategy to produce specific thermal damage to a tumor in comparison to single-injection MNP delivery. Detailed comparative analysis of therapeutic effects in terms of temperature profile and thermal damage inflicted to the targeted tissue have been done to estimate the tumor size-dependent MNP dose.

The current observation states that MNP mass should not increase in a linear proportion as the tumor grows in size. The analysis found that if MNP mass is chosen based on the constant MNP (*CD*) dosimetry (5 mg MNP/ tumor volume in cm^3) for higher sizes tumors, more thermal damage is inflicted to healthy tissue along with the damage to the tumor mass. It is estimated in this work that the MNP dose can be reduced from 5.5 to 2.8 mg MNP/ cm^3 as the tumor size increse from $3\,cm^3$ to $15\,cm^3$ to have threshold thermal effects. Thus, the MNP dose (mg/cm^3) almost drops by 50% if the tumor volume increases by five times of the breast models. Moreover, the temperature in 90% of the tumor volume also remains well above the minimum therapeutic level, i.e., 43˚C, for the *RD*-multipoint regime in all models. However, for the *CD*, the temperature, T_{90} is in a range of 42-52 ˚C following a very random passion.

Based on the constant MNP dose and reduced MNP dose regime for MNH, plots have been drawn between tumor size versus MNP dose as well as tumor size versus total MNP mass. These plots produce some correlation between tumor size versus MNP dose for MNH. However, the MNP dose versus tumor size correlation inherits the error associated with the mathematical model, MNP distribution patterns. This is due to the fact that tumors, as well as healthy tissue, are not homogeneous, and heterogeneity exists due to the microstructure and other vascular non-homogeneity of the tissue and consideration of isotropic tissue properties. However, these assumptions are routinely utilized for the computation of complex physics like

bio-heat transfer in the tissue [168][172][72]. Future studies may reduce the error associated with simplifications by incorporating more realistic thermos-physical properties distribution based on the physiology of the tumors and more realistic MNP distribution in the targeted tissue. Additionally, the inclusion of microchannels and peristaltic blood vessels [182] embedded inside the tissue can be done in further studies to simulate more realistic physiology of the tumor models. However, this work may help to give some directions regarding the MNP dose based on the tumor size for experimental and other future studies.

CHAPTER 5

Effect of Arterial Blood Flow on Magnetic Fluid Hyperthermia Applied to Human Breast Tumor.

5.1 Introduction

The magnetic nanoparticle dose (MNP) (mg of MNP/tissue volume cm^3) for different shapes and sizes of tumors for optimal efficacy of MNPH has been investigated in the previous chapter. The results of that study aid in understanding the amount of MNP dose for increasing size breast tumor models while maintaining a minimum therapeutic level of MNPH. The physical tumor models were constructed from patient-specific DICOM images for MNPH application. As an extension to the previous chapter's work, a more realistic tumor model has been made using DICOM database in this chapter. The visible physiological entity, i.e., an artery embedded inside the tumor, has also been extracted to build a more realistic physical model for MNPH application. The inclusion of artery will increase the correctness of the physical model in terms of physiology, as well as increase the accuracy of numerical simulation by including multi-physics involved in the magnetic hyperthermia process. Besides the MNP distribution, its dose, and injection sites, the therapeutic effects of MNPH is significantly influenced by the blood vessels and arteries surrounding the tumor. These arteries may serve as a significant heat sink during MNPH if they intersect or close to the tumor boundary. Therefore, in the current MNPH simulation, the effect of blood flow through an artery partially engulfed in the tumor region has been investigated. The tumor tissue is infused with a dose of 5 mg/cm^3 (as per the previous study) using a multipoint injection strategy to gain a homogenous temperature distribution. The thermal damage of the tumor region has been evaluated with two flow conditions, i.e. with the flow, and without the flow of blood through the artery. It has been observed that arterial blood transports a substantial amount of heat and preserves a considerable proportion of undamaged tumor tissue during hyperthermia. This chapter begins with the physical model construction to replicate the human breast. A subsequent mathematical model having governing equations is implemented to the breast model. Finally, the results have been complied in form of spatial-temperature distribution and thermal damage for the tumor as well as the surrounding healthy tissue.

5.2 Materials and Methods

5.2.1 Physical tumor modal

The geometrical tumor model was reconstructed from the DCE_MRI DICOM image data of breast cancer patients. This DICOM data has been obtained from a public repository service, 'The Cancer Imaging Archive' (TCIA) [169], a part of the National Cancer Research (NCI), United States.

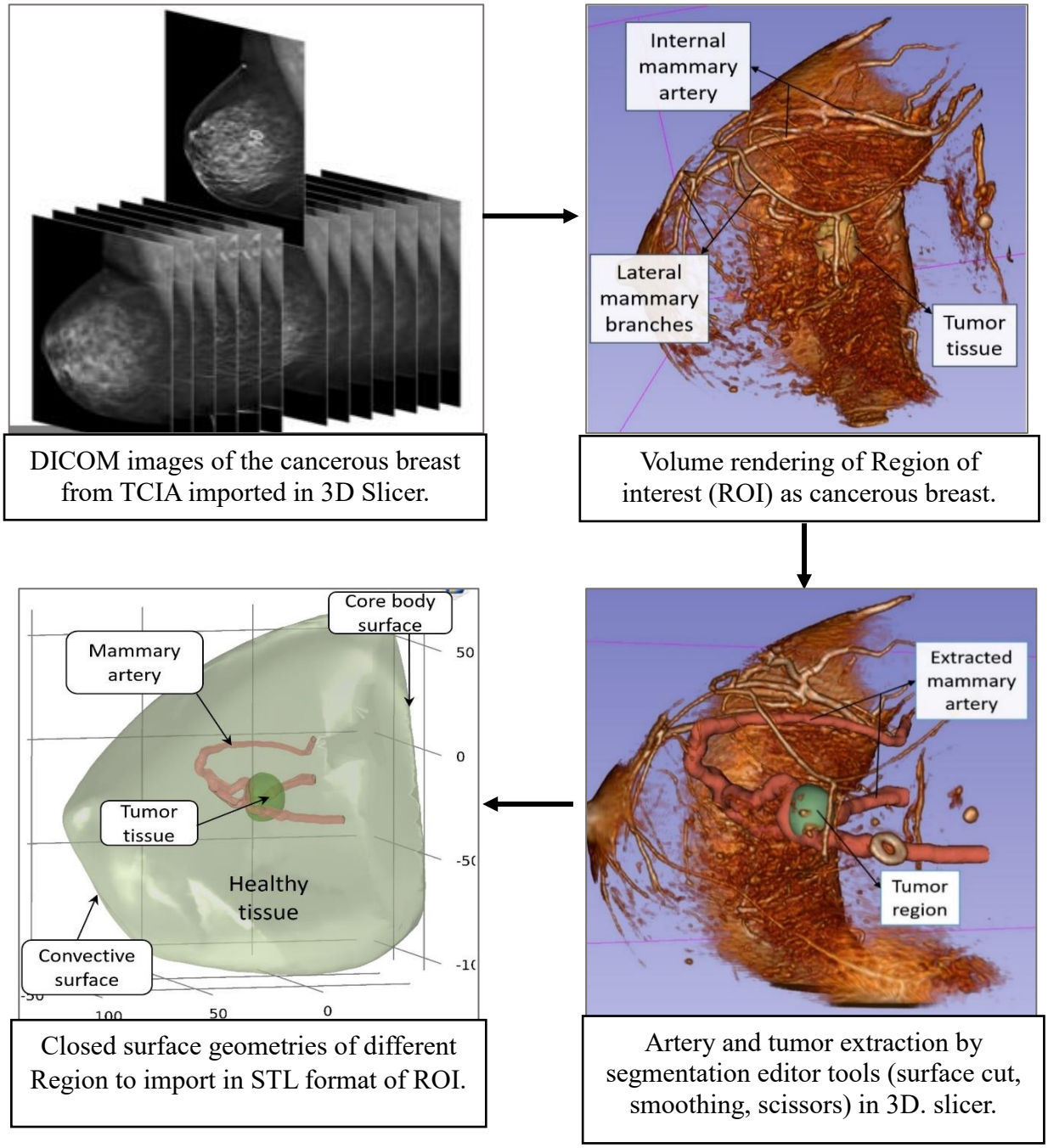

Figure 5.1: Procedural steps for breast and tumor tissue with arterial segmentation in 3D slicer.

The MRI scans of patients were imported into a 3D slicer software to develop a three-dimensional closed surface of the tumorous breast along with a mammary artery. The required procedural steps of the arterial and tumor tissue segmentation process have been given in Figure 5.1. Further, these closed surface geometries were imported into the COMSOL software in STL (stereo lithographic) file format to apply bioheat physics. More details can be found in the section 4.2 of the previous chapter 4.

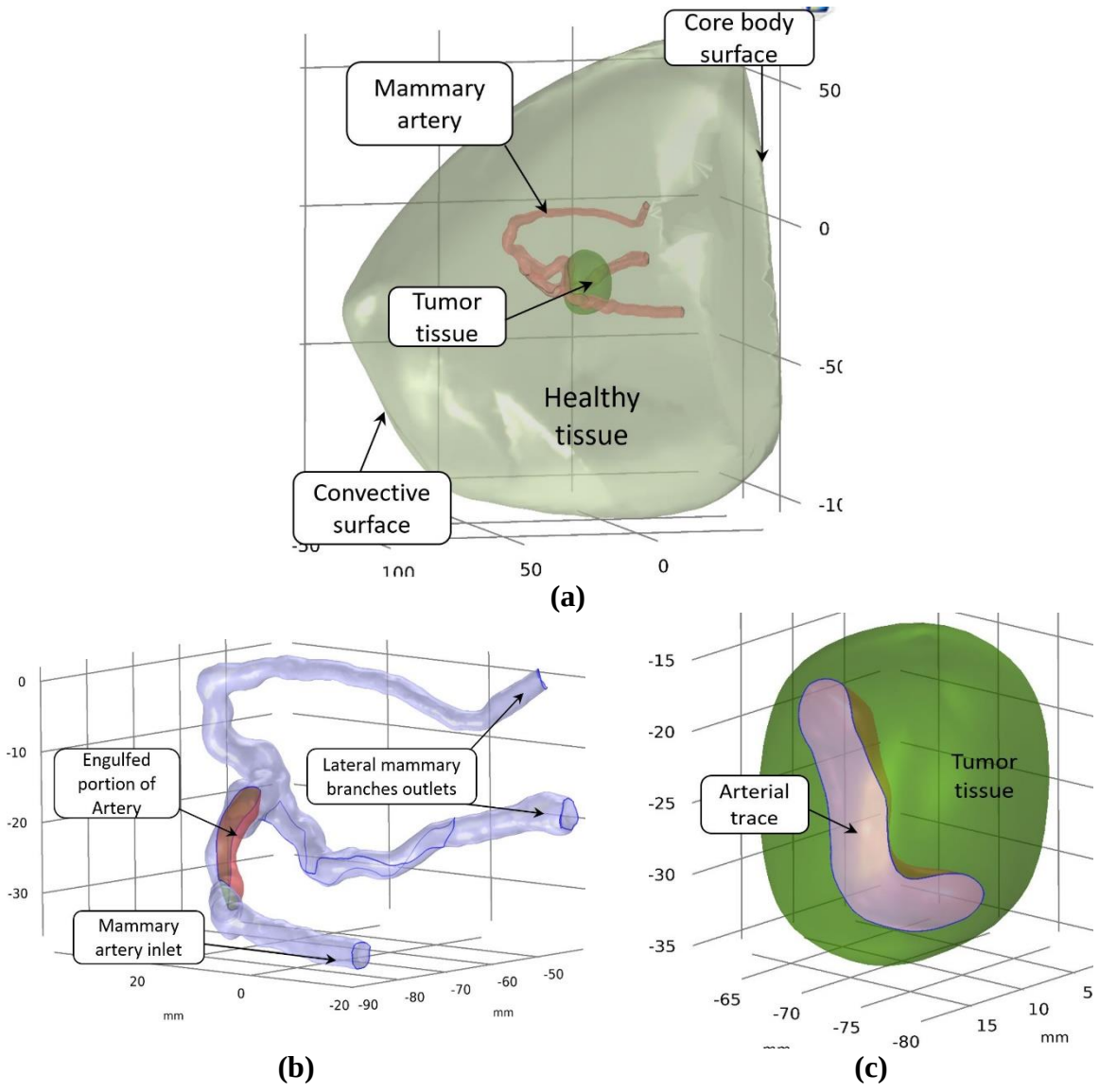

Figure 5.2: (a) Physical breast tumor model **(b)** mammary artery **(c)** tumor tissue with an arterial trace.

A physical breast model shown in Figure 5.2 (a), corresponds to the breast tissue model developed in COMSOL from the STL file. This includes the extracted mammary artery, tumor tissue, and surrounding healthy breast tissue with its thermal boundary conditions. It can be noticed from Figure 5.2 (a) that a small portion of the mammary artery is partially embedded

inside the tumor tissue surface. This engulfed portion of the artery is highlighted in Figure 5.2 (b) at the blood inlet branch and in the form of arterial trace in the tumor tissue, as shown in Figure 5.2 (c).

The present breast model is comprised of uniform healthy tissue that envelops the tumor and the arterial structure. The primary component of the breast is composed of lobes of the mammary gland, with 70-80% of breast cancer originating in this gland (ductal carcinoma and lobular carcinoma) [177]. Therefore, for healthy tissue properties, the gland's thermo-physical properties have been considered. The size of the tumor in this work is 4.3 cm^3 which comes under the T2 size category of the TNM classification of tumors [147]. The other statistical details of these extracted segments of breast have been given in Table 5.1.

Table 5.1: Statistics of Breast tumor model extracted for hyperthermia application [173]

Models	**Category**	**Volume (cm^3)**	**Surface Area (cm^2)**
Tumor Tissue	T2	4.30	1.30
Healthy Breast tissue	-	143	68.73
Mammary artery	-	3.01	2.90

5.2.2 Mathematical model

5.2.2.1 Heat transfer in tissues and arterial blood flow

The developed breast tumor geometry is simulated for MNPH treatment with the mathematical models discussed in this section. First of all, the temperature estimation in the tumor and the healthy tissue during MNH has been done using Penne's bio-heat model [153], the details of which have been discussed in section 3.3 of Chapter 3. The physical model includes the mammary artery, with two of its branches having blood flowing through them. The blood flow in arteries is considered as fully developed and laminar flow, since the blood's velocity within them is low. The Navier-Stokes (N-S) equation as a mathematical model has been used to describe the motion of viscous Newtonian incompressible flow inside the artery. This equation is derived by applying Newton's second law to fluid motion, assuming that the stress in the fluid is caused by both viscosity and pressure. N-S equation used by Gas et al. [183] for the arterial blood flow under the external magnetic field is utilized as shown in Eq. 5.1.

$$\frac{\partial u}{\partial t} + (u.\nabla)u - \nu \nabla^2 u + \frac{1}{\mu} \nabla P = F \qquad 5.1$$

$$\nabla . u = 0$$

Where u is the blood velocity, ν is the kinematic velocity, μ is dynamic viscosity of blood, P is the pressure, and F is the external gravitational force. The first part of Eq. 5.1 is the conservation of momentum, and the second part is the mass conservation. The inlet blood velocity of 0.5 m/s is considered through the artery [183], and a static pressure of 110 mmHg at the artery outlets with suppress backflow. The no-slip boundary wall has been considered along the artery walls [184]. Here the goal of applying the N-S equation to find the velocity profile inside the artery. This velocity serves as an input to apply the physics for convection heat transfer for arterial blood flow. The boundary wall of the artery is assumed to be non-porous for the mass transfer across it [184]. Therefore, the chances of MNP leakage into the stream of the artery are negligible. The tissue and material properties considered in the present for simulation have been considered as per Table 4.2 of the previous chapter.

5.2.2.2 MNP distribution and boundary conditions for the tumor model

It is well known that heat generation and its dissipation is highly influenced by the MNP distribution after injection. Regarding this, the MNPH theoretical studies utilize different types of MNP spread with certain assumptions [7][8]. Among these particle distributions, a uniformly concentrated MNP spread used by Attaluri *et al*. [71] has been considered in this work. In this type of spread, the MNP are uniformly dispersed in around 40% of the tumor volume for a single site injection. If the tumor is infused with a multi-site injection strategy, then the spread volume weightage (%) may vary to avoid the spread of the MNP near the healthy and tumor tissue boundary [185]. In the current study, two injection points have been employed, as shown in Figure 5.3. The reason for adopting two injection sites has been discussed in detail in section 4.2.2.4 of the previous chapter. Here, the tumor volume has been divided into two unequal portions, having 55 % and 45 % volume weightage. Then, the injection sites have been fixed at the centroid of these volumes. The MNPs were dispersed in 28% and 25 % volume of these two sites respectively, which is illustrated by the 1st and 2nd site spread in Figure 5.3.

The breast model in the current study is a three-dimensional volume enclosed by different surfaces. The physical model has three different morphological structures, which share boundaries with each other. So, the heat and fluid phenomenon across these boundary surfaces

have to be identified and need to be tackled with certain thermal boundary conditions for hyperthermia.

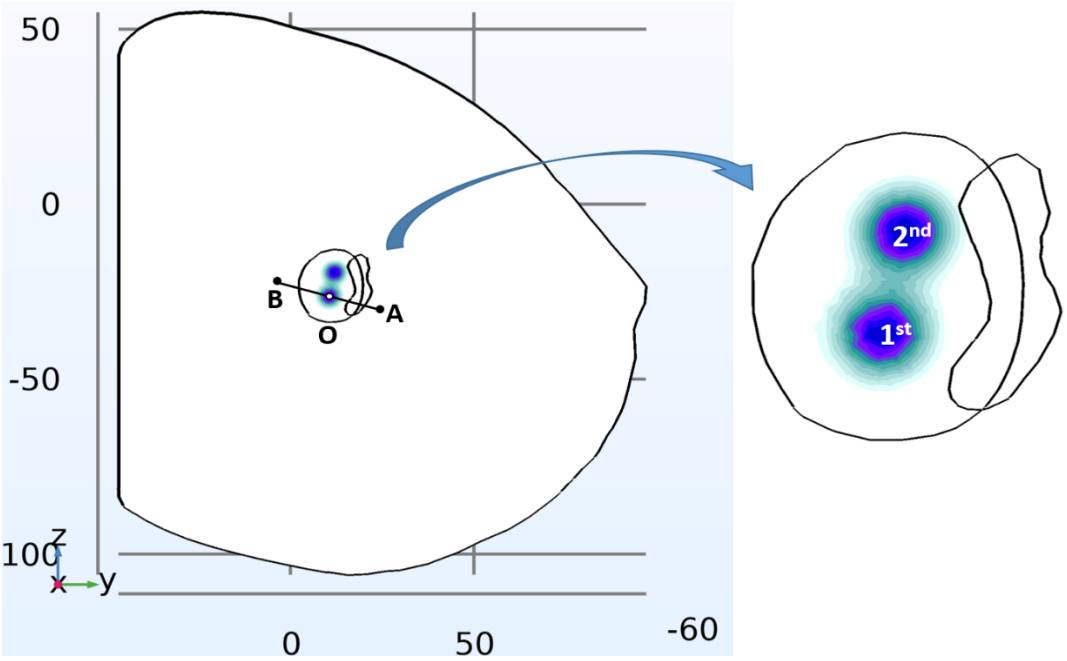

Figure 5.3: Sectional view of breast tumor on an inclined plane showing a line AOB, and the zoomed part shows the injection Sites and their respective MNP spread in tumor volume allotted to sites.

One of the interfaces is between arterial surface that is engulfed inside the tumor volume. The thermal boundary condition for this surface is the continuity in heat flux with surrounding tissue surface. The energy transported through the arterial surface will be carried away by the blood through convection. The outermost surface is considered as convective surface, liberating heat by convection to the atmosphere. The interface between the tumor tissue and the healthy tissue is tackled by continuity equation as discusses in previous chapter. The mathematical form of these boundary conditions has been discussed in section 4.2.2.2 of the previous chapter by equations 4.4 to 4.6.

5.2.2.3 The degree of tissue injury and applied heating

The effect of heating in the tissues (tumor and healthy) has been calculated in terms of thermal dosimetry (Thermal damage). Thermal damage to the tissue is calculated using the Arrhenius relation [160], whose details can be found in section 4.2.2.1 of the previous chapter. This parameter remains in a non-dimensional form, which is denoted by Ω. It is a natural log of the ratio of the percentage of undamaged tissue before heating starts, and the percentage of

undamaged tissue after being heated for a particular time. In this work $\Omega = 4.6$ has been considered, which denotes the corresponding to cell damage of 99 % [160]. Then, this parameter is integrated over the tumor volume to get the volumetric thermal damage for tumor tissue as well as healthy tissue. The relation for this volumetric thermal damage has been detailed in the section 4.2.2.1 of the previous chapter. In the current study, a constant heating power (SLP) of 50 $\mathrm{W/g}$ corresponding to the field amplitude (H_0) of 10 $\mathrm{kA/m}$ and 150 kHz of frequency (f) as chosen by Attluri et al. [9][12][13] has been considered.

5.2.2.4 Numerical Simulation and Grid Structure

In this work, all three domains are discretized with tetrahedral mesh elements for computational simulations.

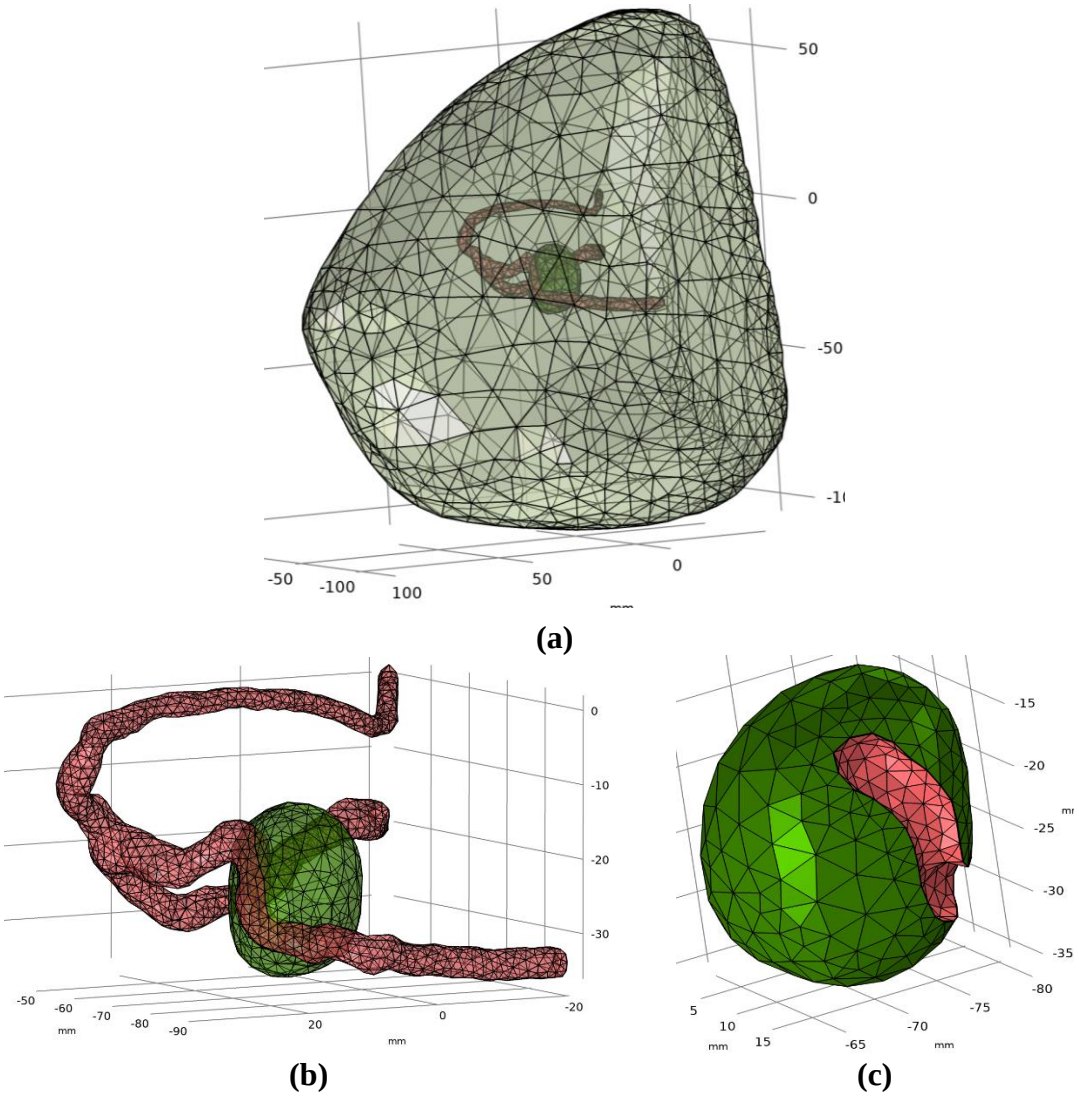

Figure 5.4: The adopted tetrahedral mesh grids for the physical breast model. **(a)** all three segments are combinedly meshed **(b)** mammary artery and tumor, and **(c)** tumor volume with arterial trace with fine mesh grid.

It should be noted from the meshed tumor model (Figure 5.4) that at the interface of any two-boundary surface i.e., of artery and tumor, or breast healthy tissue and tumor, the tetrahedral elements are kept fine. Apart from interface surfaces, towards the outer healthy tissue, a coarser mesh is utilized to reduce the computational resource. Additionally, the grid independence study was done by consecutive mesh refinement for MNPH simulation on this model. Initially, the entire geometry consists of 28084 domain elements, then the mesh was refined to 68549 number of elements. Finally, 203715 domain elements have been used for all the simulations under the current study.

The absolute deviation of around 0.1 % has been noticed in the temperature measurement of the centroid of the model. As this study is an extension of the study done in the previous chapter, the pursuit of its validation and integrity with the experimental work is similar, whose details can be found in section 4.2.2.3 of the previous chapter 4.

5.3 Results

This section comprises the results obtained from the MNPH simulation done on the breast physical model shown in Figure 5.2. The tumor tissue has been dosed with 5 (mg/cm^3) using multi-injection MNP delivery. The duration of MNPH therapy is simulated for 3600 seconds for the considered breast model [164]. The temperature in the targeted tissues starts rising as soon as the MNPH applicator induces heat and reaches to a steady state. The thermal profile in different parts of the present breast model has been discussed in the following section.

5.3.1 The thermal and fluid conditions for the artery during MNPH

The fluid flow through the arteries is an important part of transporting the blood. Additionally, this flow is responsible for thermal or heat convection from one part to another part of the body. The blood flow carries out the heat and mass convection phenomenon through the artery. So, in the current study, the effect of arterial blood flow on heat convection has been considered. In a contrary to this flow phenomenon, a non-flow blood condition has also been applied to compare the flow effect. In this non-flow condition, the artery becomes as part of healthy tissue during simulations. The velocity, pressure and temperature distribution inside the artery for these two different flow conditions has been obtained, as shown in Figure 5.5.

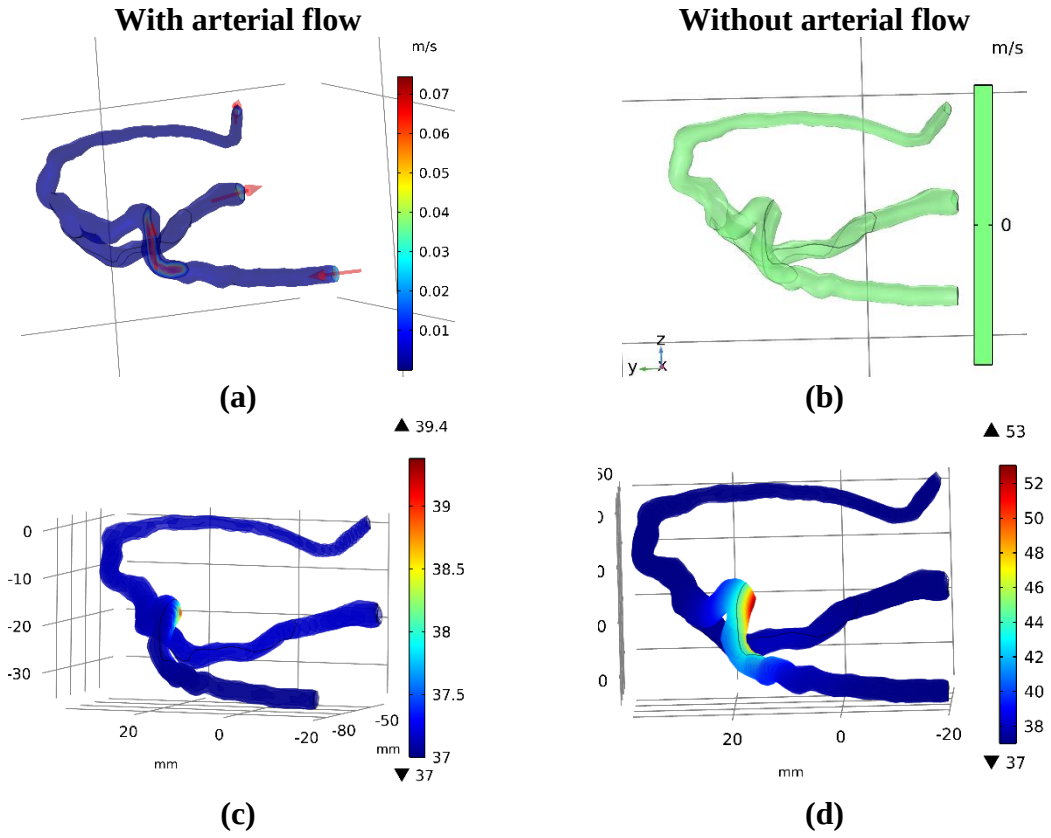

Figure 5.5: Thermo-fluid conditions of the artery under the hyperthermia under blood flow and without blood flow conditions. Fig. (a & b) shows blood velocity, and Fig. (c & d) shows the surface temperature of the artery.

The arterial blood flow is in the first column of Figure 5.5 (a), and (c), and without flow condition is in the second column of Figure 5.5 (b), and (d). The surface temperature of the artery rises upto only 39.4 ˚C for the flow condition. As the maximum of the heat diffused from the tumor at the artery interface has been carried away by the convection effect of the blood. On the other hand, the maximum surface temperature of artery reaches upto 53 ˚C in the non-flow blood condition through the artery. For this condition, the blood flow velocity remains zero for the artery. However, there is uniform blood flow through Figure 5.5 (a).

5.3.2 The steady-state spatial temperature and thermal damage distribution within the tumor model during MNPH.

The steady-state spatial temperature and tissue thermal damage distribution in the form of isotherms contours for the breast model selected in this study are discussed in this section. The

temperature contours have been plotted for the flow and non-flow blood conditions shown in two columns of Figure 5.6.

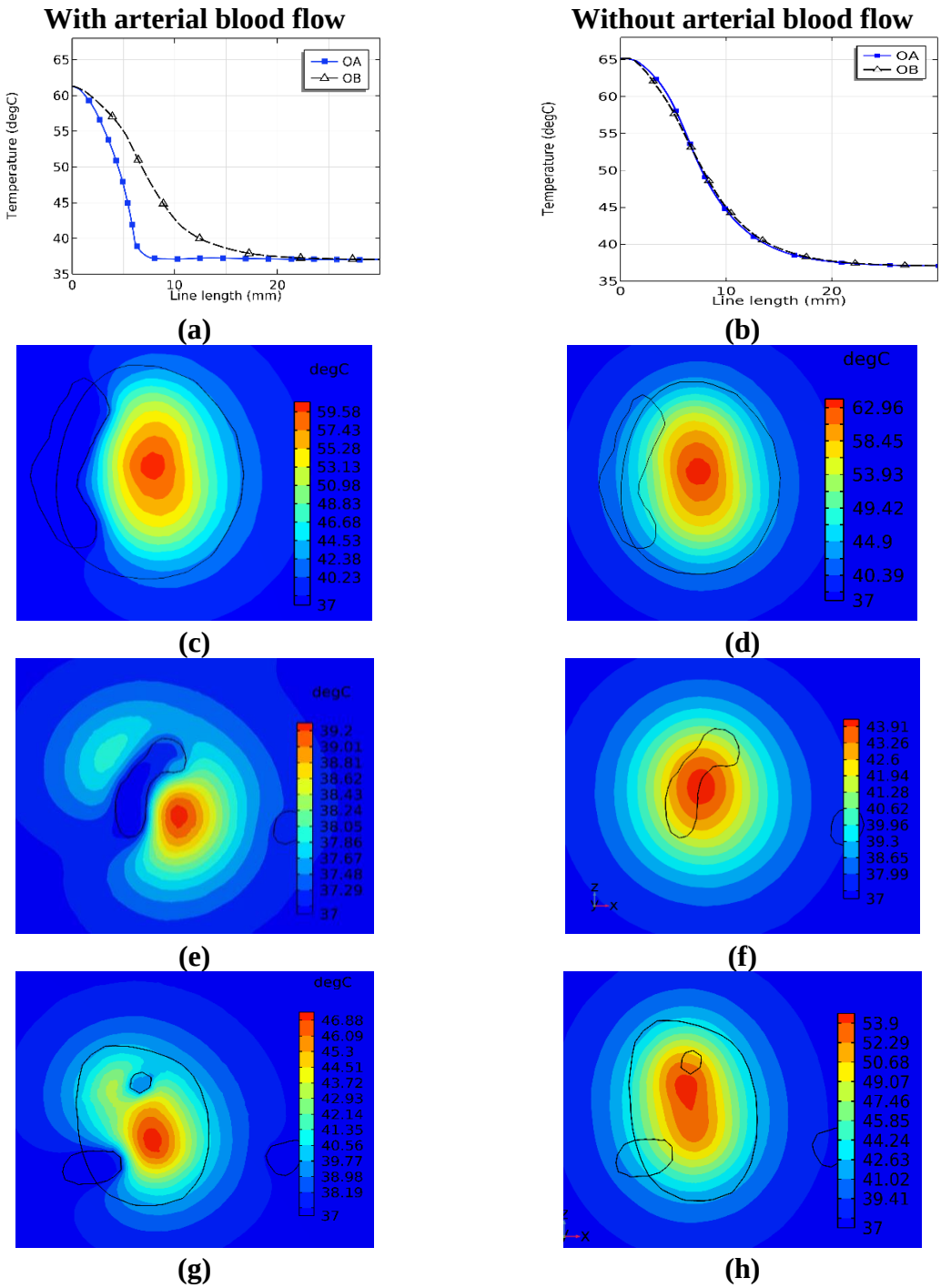

Figure 5.6. Temperature contour on different planes under the MNPH Figure. (a-c) with blood flow and Fig. (d-f) without blood flow conditions.

Additionally, the temperature profile along a center line AOB (Figure 5.3) throughout the tumor region has also been plotted. The maximum temperature inside the tumor region was

measured at the center point 'O'. The other points along this line, i.e., A and B are located inside the healthy tissue, far from the heated region. It is noticed from Figure 5.6 (a) that as we move towards the artery (along OA) for flow conditions through it, the temperature drops rapidly upto the boundary interface and reaches to the core body temperature at 37 ˚C. However, for the no-flow conditions, the temperature profile along OA and OB overlap each other, as shown in Figure 5.6 (b).

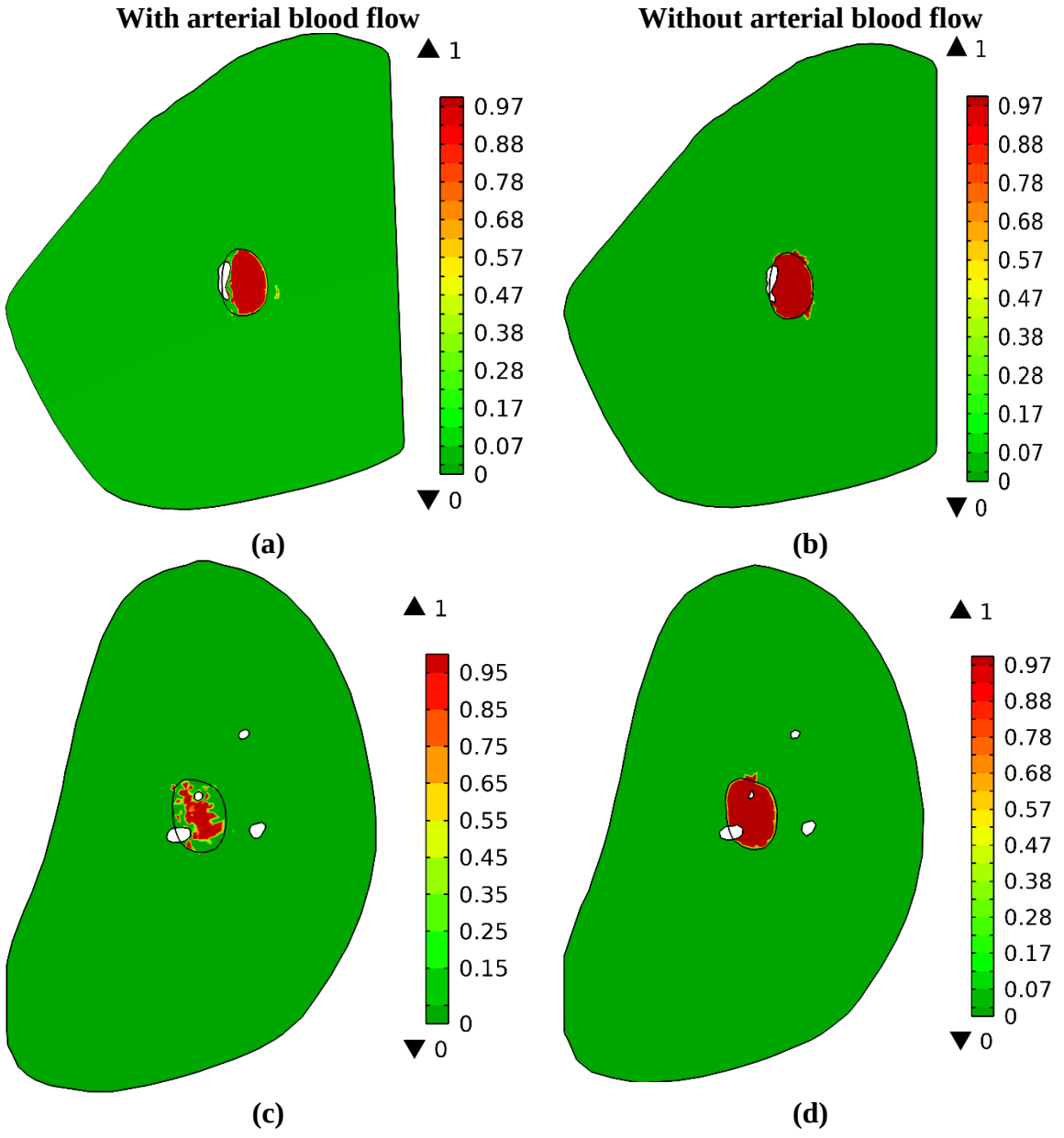

Figure 5.7. Thermal damage contour on two different planes under the hyperthermia Fig. (a & c) with blood flow and Fig. (b & d) without blood flow conditions.

This overlap temperature profile shows the symmetric heat diffusion towards both sides of the tumor centroid i.e., along OA and OB. Furthermore, the rapid heat sink is observed towards

the artery for the flow condition. This heat sink can be easily visualized from the temperature contours shown in Figure 5.6 (c), (e), and (g) at different planes. The contour lines along the arterial surface have reached a temperature equal to the arterial blood. However, when the artery behaves as part of healthy tissue, the heat diffusion takes place in a symmetric manner on all sides of the heating zone.

The thermal damage inside the tumor and healthy tissue has been observed in a similar way to the temperature distribution. The thermal damage pattern for both of the conditions have been shown in Figure 5.7 in the form of contours. In these contours, the black line separates the tumor tissue and the healthy tissue. The red zone inside Figure 5.7 describes the thermal damage spread in the tissues. The tissue damage has been calculated as per the damage criterion discussed in section 5.2.2.3. A significant decrease in thermal damage has been noticed for the arterial flow condition as compared to the non-flow condition.

Table 5.2: The temperature and thermal damage achieved in the tumor as well as the healthy region of the physical model.

Tissues	**Parameters**	***Without arterial flow***	***With arterial flow***
Tumor	T_{90}	43.9	40.5
	T_{10}	59.2	54.35
	T_{max}	65.2	60.4
	HI	2.2	3.9
	$\%\ volume\ of\ C_d$	91.27	65.1
Healthy	T_{max}	45.0	43.43
	$\%\ volume\ of\ C_d$	9.08	0.54

Furthermore, the quantification of the thermal damage for tumor as well as healthy tissue has been done in the form of percentage tissue volume damage. Additionally, the temperature assessment is done by T_{90} and T_{10} (temperature achieved in at least 90% and 10% tumor volume), and a heterogeneity index (HI), which is defined as $(T_{10} - T_{90}/(T_{90} - T_{CB})$ [76]. Table 5.2 shows the statistical details of the temperature and thermal damage induced during MNPH of the current breast tumor model. It should be noted that the thermal damage to the tumor tissue has decreased by around 25 % due to arterial blood flow in the vicinity of the

tumor. The temperature is in the 90% of the tumor volume, i.e., T_{90} has come to around 40.5 ˚C, which is not considered a therapeutic temperature under magnetic hyperthermia.

5.4 Conclusions:

The tumor model, which includes the artery, was created from DICOM data using 3D slicer software. Its goal is to determine the effect of blood flow on the quantity of thermal dose required for the best therapeutic outcome during hyperthermia. A significant quantity of heat is transported through arterial blood, which has been observed to preserve a substantial portion of undamaged tumor tissue throughout hyperthermia. Thus the heat sink effects by presence of artery on the therapeutic efficacy of MNPH is included to design the treatment protocals for MNPH.

CHAPTER 6

CONCLUSION AND FUTURE SCOPE

6.1 Conclusions:

Heat as a therapy for cancer treatment has been a field of attention from decades. One such application is hyperthermia in which the temperature of the targeted region or limb is increased by 2-6 ˚C, above normal body temperature by an external source. In the modern era, there are various types of external heat sources used for hyperthermia. These consist of electromagnetic (EM) antennas, EM capacitive electrodes, ultrasonic transducers, infrared heating systems, thermal chamber heating, intracavital heating, etc. Magnetically induced heating is one such non-invasive or minimally invasive hyperthermia treatment for cancer treatment has gained interest. Literature shows that the implementation of this therapy as a standalone is less explored due to some challenges associated with it. Nevertheless, it has been used as an adjuvant therapy with other conventional cancer therapies like radiotherapy and chemotherapy. The present work brought forth the solutions to improve the efficacy of magnetic nanoparticle induced hyperthermia (MNPH). The improvements are in form of better nanoparticle material selection, their dose, distribution inside the tissue, and injection method to attain higher therapeutic effect by this treatment. Both numerical and experimental studies have been performed in this work. However, major portion of the work is computational in nature to enhance the applicability of this hyperthermia therapy toward the clinical aspects. The following section consists of the summary and conclusions of this work.

1) Initially the numerical study is performed to explore the effect of magnetic nanoparticle size-dependent properties on induced heat generation or specific loss power (SLP). Mainly two major size-dependent magnetic properties, i.e., magnetic anisotropy and saturation magnetization for SLP estimation of cobalt, magnetite, and manganese ferrite nanoparticles were considered. It has been confirmed from the literature that the anisotropy energy value is highly influenced by particle shape, size, surface, blocking temperature, etc. The other key factor is saturation magnetization, which is also highly influenced by MNP size. However, theoretical studies consider constant value in SLP calculation. However, in this work empirical relations for these magnetic parameters considering the effect of influencing parameters obtained from experimental studies have been established.

- The results indicate that the SLP obtained with the size-dependent empirical relations is closer to the experimental value of SLP under similar conditions of magnetic hyperthermia.
- Additionally, it is concluded that a particular size of MNP at the resonant amplitude and frequency values generates the maximum SLP. Consequently, prior to implementing hyperthermia therapy, it is critical to choose a specific particle size and frequency at which it delivers a high amount of dissipative power.

  The *In Vitro* investigation demonstrates that the temperature profiles obtained from experimental computational heating are in good agreement with each other.

2) To elucidate the effects of tumor position and clinical environmental conditions (temperature, velocity of ambient air) on the therapeutic effects of MNPH in a superficial-like breast tumor model simulation studies are conducted with following conclusions.
    - It is noticed that the change in heat transfer rate from the skin by changing the ambient condition has greater effects on the therapeutic efficacy for superficial tumors. However, as the depth of the tumor increased the skin effects became negligible.
    - It infers from this study that under similar magnetic field parameters and MNP dose, superficial tumors have higher therapeutic effects in terms of thermal dosimetry in comparison to deep-rooted tumors.
    - This study concludes that, up to the critical depth of the tumor, about half of the tumor size, the therapeutic effects in terms of elevation of temperature and thermal dosimetry are susceptible to the change in therapeutic environment on the skin as well as the depth of the tumor. However, beyond these therapeutic effects of MNPH become independent of these two parameters.

3) The effects of tumor shape, size, and MNP injections on the MNP dose (mg of MNP/tissue volume cm^3) for MNPH are thoroughly investigated. MNPH has been applied to breast tumor models generated from patient-specific DICOM (Digital Imaging and Communications in Medicine) data using CT (Computed tomography) or MRI (Medical resonance imaging) scans.
    - It is observed that the MNP dose (mg/cm^3) almost drops by 50% if the tumor volume increases by five times of the breast models.

- The multipoint injection regime plays a critical role in decreasing the MNP dose input for the tumor.

4) It is observed from that last study that the blood vessels and arteries around the tumor have a substantial impact on the therapeutic efficacy of MNPH, in addition to the MNP distribution, dose, and injection sites.
    - The arteries serve as a significant heat sink during MNPH if they intersect the tumor boundary.
    - It was noticed that the thermal damage was reduced by 25% due to the arterial blood flow in the partially submerged artery in the tumor region.

6.2 Future scope of the present work

- In this work most of the studies are computational in nature. This may be due to the limitation in experimental facilities and infrastructure. However, future studies may include further experimental works on MNPH. Following are the few points that can be explored in the future studies for MNPH. Inclusion of more physiological entities in the tumor model can give a more realistic outcome of the MNPH therapy that will eventually help its usage in the clinical implementation.
- *In Vitro* studies can be extended toward more realistic phantom studies.
- This therapy can be further investigated through *In-Vivo* studies on MNPH.
- More tissue engineering and physics can be explored for this therapy.

BIBILOGRAPHY:

[1] "Cancer." https://www.who.int/news-room/fact-sheets/detail/cancer (accessed Sep. 05, 2023).

[2] "Cancer today." https://gco.iarc.fr/today/fact-sheets-cancers (accessed Nov. 21, 2023).

[3] H. Shahzad, *Neoplasm*. IntechOpen, 2018. [Online]. Available: https://books.google.co.in/books?id=-GiQDwAAQBAJ

[4] "National cancer institute |Cancer types," 2023. https://www.cancer.gov/types (accessed Sep. 07, 2023).

[5] H. Sung *et al.*, "Global Cancer Statistics 2020: GLOBOCAN Estimates of Incidence and Mortality Worldwide for 36 Cancers in 185 Countries," *CA. Cancer J. Clin.*, vol. 71, no. 3, pp. 209–249, May 2021, doi: https://doi.org/10.3322/caac.21660.

[6] H. Sung *et al.*, "Global Cancer Statistics 2020: GLOBOCAN Estimates of Incidence and Mortality Worldwide for 36 Cancers in 185 Countries," *CA. Cancer J. Clin.*, vol. 71, no. 3, pp. 209–249, 2021, doi: 10.3322/caac.21660.

[7] R. K. Nair *et al.*, "Enhancing the effects of chemotherapy by combined macrophage-mediated photothermal therapy (PTT) and photochemical internalization (PCI)," *Lasers Med. Sci.*, vol. 33, no. 8, pp. 1747–1755, 2018, doi: 10.1007/s10103-018-2534-5.

[8] W. Wu, Y. Pu, and J. Shi, "Nanomedicine-enabled chemotherapy-based synergetic cancer treatments," *J. Nanobiotechnology*, vol. 20, no. 1, pp. 1–21, 2022, doi: 10.1186/s12951-021-01181-z.

[9] Z. Lu *et al.*, "Deciphering the Biological Effects of Radiotherapy in Cancer Cells," *Biomolecules*, vol. 12, no. 9, 2022, doi: 10.3390/biom12091167.

[10] "Colon Cancer Surgery | Types of Colon Cancer Surgery | American Cancer Society." https://www.cancer.org/cancer/types/colon-rectal-cancer/treating/colon-surgery.htm (accessed Nov. 18, 2023).

[11] H. W. Zhang, Z. X. Lin, F. Cheung, W. C. S. Cho, and J. L. Tang, "Moxibustion for alleviating side effects of chemotherapy or radiotherapy in people with cancer," *Cochrane Database Syst. Rev.*, vol. 2018, no. 11, 2018, doi: 10.1002/14651858.CD010559.pub2.

[12] H. Majeed and V. Gupta, *Adverse Effects Of Radiation Therapy*. Icahn School of Medicine at Mount Sinai, Elmhurst Hospital: StatPearls Publishing, Treasure Island (FL), 2022. [Online]. Available: http://europepmc.org/abstract/MED/33085406

[13] Y. Yagawa, K. Tanigawa, Y. Kobayashi, and M. Yamamoto, "Cancer immunity and therapy using hyperthermia with immunotherapy, radiotherapy, chemotherapy, and surgery," *J. Cancer Metastasis Treat.*, vol. 3, no. 10, p. 218, 2017, doi: 10.20517/2394-4722.2017.35.

[14] H. H. Kampinga, E. Dikomey, H. H. Kampinga, and E. Dikomey, "Hyperthermic

radiosensitization : mode of action and clinical relevance Review Hyperthermic radiosensitization : mode of action and clinical relevance," *Int. J. Radiat. Biol.*, vol. 77, no. 4, pp. 399–408, 2017, doi: 10.1080/09553000010024687.

[15] M. L. Sottile and S. B. Nadin, "Heat shock proteins and DNA repair mechanisms: an updated overview," *Cell Stress Chaperones*, vol. 23, no. 3, pp. 303–315, May 2018, doi: 10.1007/s12192-017-0843-4.

[16] E. & Potter, "Thermal Tumor Ablation in Clinical Use," *IEEE Pulse*, vol. 23, no. 1, pp. 1–7, 2008, doi: 10.1109/MPUL.2011.942603.

[17] K. J. A. U.-Z. Grabarczyk, "Greek and Latin in medical terminology," *Greek and Latin in medical terminology*, vol. 1, no. 2. pp. 41–52, 2013. [Online]. Available: https://journals.viamedica.pl/medical_research_journal/article/view/36871

[18] W. Coley and E. Dashiell, "Fever in Cancer Treatment: Coley's Therapy and Epidemiologic Observations," vol. 1, no. 1, pp. 92–100, 2012.

[19] W. BUSCH, "No Title," *Berl Klin Wochenschr*, vol. 5, no. 5, p. 137, 1867.

[20] G. S. Kienle, "Fever in Cancer Treatment: Coley's Therapy and Epidemiologic Observations," *Glob. Adv. Heal. Med.*, vol. 1, no. 1, pp. 92–100, Mar. 2012, doi: 10.7453/gahmj.2012.1.1.016.

[21] A. Hervault and N. T. K. Thanh, "Magnetic nanoparticle-based therapeutic agents for thermo-chemotherapy treatment of cancer," *Nanoscale*, vol. 6, no. 20, pp. 11553–11573, 2014, doi: 10.1039/c4nr03482a.

[22] Z. Hedayatnasab, F. Abnisa, and W. M. A. W. Daud, "Review on magnetic nanoparticles for magnetic nanofluid hyperthermia application," *Mater. Des.*, vol. 123, pp. 174–196, 2017, doi: 10.1016/j.matdes.2017.03.036.

[23] A. Chicheł, J. Skowronek, M. Kubaszewska, and M. Kanikowski, "Hyperthermia – description of a method and a review of clinical applications," *Reports Pract. Oncol. Radiother.*, vol. 12, no. 5, pp. 267–275, 2007, doi: https://doi.org/10.1016/S1507-1367(10)60065-X.

[24] F. Sato *et al.*, "The operation of a magnetic micromachine for hyperthermia and its exothermic characteristic," *IEEE Trans. Magn.*, vol. 38, no. 5, pp. 3362–3364, 2002, doi: 10.1109/TMAG.2002.802304.

[25] D. Haemmerich and F. T. Lee, "Multiple applicator approaches for radiofrequency and microwave ablation," *Int. J. Hyperth.*, vol. 21, no. 2, pp. 93–106, 2005, doi: 10.1080/02656730412331286894.

[26] K. Hynynen *et al.*, "Temperature distributions during clinical scanned, focused ultrasound hyperthermia treatments," *Int. J. Hyperth.*, vol. 6, no. 5, pp. 891–908, Jan. 1990, doi: 10.3109/02656739009140971.

[27] A. B. Salunkhe, V. M. Khot, and S. H. Pawar, "Magnetic Hyperthermia with Magnetic Nanoparticles: A Status Review," *Curr. Top. Med. Chem.*, vol. 14, no. 5, pp. 572–594, 2014, doi: 10.2174/1568026614666140118203550.

[28] L. Asín, M. R. Ibarra, A. Tres, and G. F. Goya, “Controlled cell death by magnetic hyperthermia: Effects of exposure time, field amplitude, and nanoparticle concentration,” *Pharm. Res.*, vol. 29, no. 5, pp. 1319–1327, 2012, doi: 10.1007/s11095-012-0710-z.

[29] V. S. Saji, H. C. Choe, and K. W. K. Yeung, “Nanotechnology in biomedical applications: a review,” *Int. J. Nano Biomater.*, vol. 3, no. 2, pp. 119–139, Jan. 2010, doi: 10.1504/IJNBM.2010.037801.

[30] A. Miaskowski, B. Sawicki, and A. Krawczyk, “The use of magnetic nanoparticles in low frequency inductive hyperthermia,” *COMPEL - Int. J. Comput. Math. Electr. Electron. Eng.*, vol. 31, no. 4, pp. 1096–1104, 2012, doi: 10.1108/03321641211227348.

[31] R. E. Rosensweig, “Heating magnetic fluid with alternating magnetic field,” *J. Magn. Magn. Mater.*, vol. 252, pp. 370–374, 2002, doi: https://doi.org/10.1016/S0304-8853(02)00706-0.

[32] K. Simeonidis *et al.*, “In-situ particles reorientation during magnetic hyperthermia application: Shape matters twice,” *Sci. Rep.*, vol. 6, no. October, pp. 1–11, 2016, doi: 10.1038/srep38382.

[33] M. Salloum, R. H. Ma, D. Weeks, and L. Zhu, “Controlling nanoparticle delivery in magnetic nanoparticle hyperthermia for cancer treatment: Experimental study in agarose gel,” *Int. J. Hyperth.*, vol. 24, no. 4, pp. 337–345, Jan. 2008, doi: 10.1080/02656730801907937.

[34] T. Lam *et al.*, “Fabricatingwater dispersible superparamagnetic iron oxide nanoparticles for biomedical applications through Ligand exchange and direct conjugation,” *Nanomaterials*, vol. 6, no. 6, p. 100, 2016, doi: 10.3390/nano6060100.

[35] S. Singh, “Size dependence of the effective magnetic anisotropy in Co, Ni, Fe, and magnetite nanoparticles: Testing the core-shell-surface-layer (CSSL) model,” pp. 1–11.

[36] C. Liu, A. J. Rondinone, and Z. J. Zhang, “Synthesis of magnetic spinel ferrite CoFe2O4 nanoparticles from ferric salt and characterization of the size-dependent superparamagnetic properties,” *Pure Appl. Chem.*, vol. 72, no. 1–2, pp. 37–45, 2000, doi: 10.1351/pac200072010037.

[37] C. Caizer, “Computational study on superparamagnetic hyperthermia with biocompatible SPIONs to destroy the cancer cells,” *J. Phys. Conf. Ser.*, vol. 521, no. 1, pp. 6–10, 2014, doi: 10.1088/1742-6596/521/1/012015.

[38] S. R. Patade, D. D. Andhare, S. B. Somvanshi, S. A. Jadhav, M. V. Khedkar, and K. M. Jadhav, “Self-heating evaluation of superparamagnetic MnFe2O4 nanoparticles for magnetic fluid hyperthermia application towards cancer treatment,” *Ceram. Int.*, vol. 46, no. 16, pp. 25576–25583, 2020, doi: 10.1016/j.ceramint.2020.07.029.

[39] A. Salunkhe, V. Khot, S. I. Patil, S. A. M. Tofail, J. Bauer, and N. D. Thorat, “MRI Guided Magneto-chemotherapy with High-Magnetic-Moment Iron Oxide Nanoparticles for Cancer Theranostics,” *ACS Appl. Bio Mater.*, vol. 3, no. 4, pp. 2305–2313, 2020, doi: 10.1021/acsabm.0c00077.

[40] H. M. Joshi *et al.*, “Effects of shape and size of cobalt ferrite nanostructures on their MRI contrast and thermal activation,” *J. Phys. Chem. C*, vol. 113, no. 41, pp. 17761–17767, 2009, doi: 10.1021/jp905776g.

[41] K. V. Chandekar and K. M. Kant, “Effect of size and shape dependent anisotropy on superparamagnetic property of CoFe2O4 nanoparticles and nanoplatelets,” *Phys. B Condens. Matter*, vol. 520, no. February, pp. 152–163, 2017, doi: 10.1016/j.physb.2017.06.001.

[42] S. Oyarzún, A. Tamion, F. Tournus, V. Dupuis, and M. Hillenkamp, “Size effects in the magnetic anisotropy of embedded cobalt nanoparticles: From shape to surface,” *Sci. Rep.*, vol. 5, no. March, pp. 16–21, 2015, doi: 10.1038/srep14749.

[43] M. P. Calatayud *et al.*, “Cell damage produced by magnetic fluid hyperthermia on microglial BV2 cells,” *Sci. Rep.*, vol. 7, no. 1, pp. 1–16, 2017, doi: 10.1038/s41598-017-09059-7.

[44] R. Di Corato *et al.*, “Magnetic hyperthermia efficiency in the cellular environment fordifferent nanoparticle designs,” *Biomaterials*, vol. 35, no. 24, pp. 6400–6411, 2014, doi: 10.1016/j.biomaterials.2014.04.036.

[45] K. V. Chandekar and K. M. Kant, “Effect of size and shape dependent anisotropy on superparamagnetic property of CoFe2O4 nanoparticles and nanoplatelets,” *Phys. B Condens. Matter*, vol. 520, no. May, pp. 152–163, 2017, doi: 10.1016/j.physb.2017.06.001.

[46] M. Salloum, R. Ma, and L. Zhu, “An in-vivo experimental study of temperature elevations in animal tissue during magnetic nanoparticle hyperthermia,” *Int. J. Hyperth.*, vol. 24, no. 7, pp. 589–601, 2008, doi: 10.1080/02656730802203377.

[47] M. Johannsen *et al.*, “Thermotherapy of Prostate Cancer Using Magnetic Nanoparticles: Feasibility, Imaging, and Three-Dimensional Temperature Distribution,” *Eur. Urol.*, vol. 52, no. 6, pp. 1653–1662, 2007, doi: 10.1016/j.eururo.2006.11.023.

[48] A. Attaluri, R. Ma, Y. Qiu, W. Li, and L. Zhu, “Nanoparticle distribution and temperature elevations in prostatic tumours in mice during magnetic nanoparticle hyperthermia,” *Int. J. Hyperth.*, vol. 27, no. 5, pp. 491–502, 2011, doi: 10.3109/02656736.2011.584856.

[49] A. A. Golneshan and M. Lahonian, “The effect of magnetic nanoparticle dispersion on temperature distribution in a spherical tissue in magnetic fluid hyperthermia using the lattice Boltzmann method,” *Int. J. Hyperth.*, vol. 27, no. 3, pp. 266–274, 2011, doi: 10.3109/02656736.2010.519370.

[50] D. Chang *et al.*, “Biologically targeted magnetic hyperthermia: Potential and limitations,” *Front. Pharmacol.*, vol. 9, no. AUG, 2018, doi: 10.3389/fphar.2018.00831.

[51] M. Johannsen *et al.*, “Evaluation of Magnetic Fluid Hyperthermia in a Standard Rat Model of Prostate Cancer,” *J. Endourol.*, vol. 18, no. 5, pp. 495–500, 2004, doi: 10.1089/0892779041271715.

[52] H. Chiriac *et al.*, “In vitro cytotoxicity of Fe–Cr–Nb–B magnetic nanoparticles under

high frequency electromagnetic field," *J. Magn. Magn. Mater.*, vol. 380, pp. 13–19, 2015, doi: https://doi.org/10.1016/j.jmmm.2014.10.015.

[53] I. M. Obaidat, V. Narayanaswamy, S. Alaabed, S. Sambasivam, and C. V. V. Muralee Gopi, "Principles of magnetic hyperthermia: A focus on using multifunctional hybrid magnetic nanoparticles," *Magnetochemistry*, vol. 5, no. 4, 2019, doi: 10.3390/magnetochemistry5040067.

[54] M. A. Giordano, G. Gutierrez, and C. Rinaldi, "Fundamental solutions to the bioheat equation and their application to magnetic fluid hyperthermia," *Int. J. Hyperth.*, vol. 26, no. 5, pp. 475–484, 2010, doi: 10.3109/02656731003749643.

[55] Y. Tang, R. C. C. Flesch, and T. Jin, "Numerical investigation of temperature field in magnetic hyperthermia considering mass transfer and diffusion in interstitial tissue," *J. Phys. D. Appl. Phys.*, vol. 51, no. 3, 2018, doi: 10.1088/1361-6463/aa9b9a.

[56] I. Raouf, S. Khalid, A. Khan, J. Lee, H. S. Kim, and M. H. Kim, "A review on numerical modeling for magnetic nanoparticle hyperthermia: Progress and challenges," *J. Therm. Biol.*, vol. 91, no. April, p. 102644, 2020, doi: 10.1016/j.jtherbio.2020.102644.

[57] A. Doaga *et al.*, "Synthesis and characterizations of manganese ferrites for hyperthermia applications," *Mater. Chem. Phys.*, vol. 143, no. 1, pp. 305–310, 2013, doi: 10.1016/j.matchemphys.2013.08.066.

[58] P. T. Phong *et al.*, "Study of specific loss power of magnetic fluids with various viscosities," *J. Magn. Magn. Mater.*, vol. 428, no. October 2016, pp. 36–42, 2017, doi: 10.1016/j.jmmm.2016.12.008.

[59] R. Gupta and D. Sharma, "Biofunctionalization of magnetite nanoparticles with stevioside: effect on the size and thermal behaviour for use in hyperthermia applications," *Int. J. Hyperth.*, vol. 36, no. 1, pp. 301–311, Jan. 2019, doi: 10.1080/02656736.2019.1565787.

[60] N. K. Prasad, K. Rathinasamy, D. Panda, and D. Bahadur, "Mechanism of cell death induced by magnetic hyperthermia with nanoparticles of γ-MnxFe2–xO3 synthesized by a single step process," *J. Mater. Chem.*, vol. 17, no. 48, pp. 5042–5051, 2007, doi: 10.1039/B708156A.

[61] A. Yao, F. Ai, D. Wang, W. Huang, and X. Zhang, "Synthesis, characterization and in vitro cytotoxicity of self-regulating magnetic implant material for hyperthermia application," *Mater. Sci. Eng. C*, vol. 29, no. 8, pp. 2525–2529, 2009, doi: https://doi.org/10.1016/j.msec.2009.07.021.

[62] B. Samanta, H. Yan, N. O. Fischer, J. Shi, D. J. Jerry, and V. M. Rotello, "Protein-passivated Fe3O4nanoparticles: low toxicity and rapid heating for thermal therapy," *J. Mater. Chem.*, vol. 18, no. 11, pp. 1204–1208, 2008, doi: 10.1039/B718745A.

[63] F. M. Martín-Saavedra, E. Ruíz-Hernández, A. Boré, D. Arcos, M. Vallet-Regí, and N. Vilaboa, "Magnetic mesoporous silica spheres for hyperthermia therapy," *Acta Biomater.*, vol. 6, no. 12, pp. 4522–4531, 2010, doi: https://doi.org/10.1016/j.actbio.2010.06.030.

[64] P.-E. Le Renard *et al.*, "Magnetic and in vitro heating properties of implants formed in situ from injectable formulations and containing superparamagnetic iron oxide nanoparticles (SPIONs) embedded in silica microparticles for magnetically induced local hyperthermia," *J. Magn. Magn. Mater.*, vol. 323, no. 8, pp. 1054–1063, 2011, doi: https://doi.org/10.1016/j.jmmm.2010.12.003.

[65] C. Caizer, "Optimization study on specific loss power in superparamagnetic hyperthermia with magnetite nanoparticles for high efficiency in alternative cancer therapy," *Nanomaterials*, vol. 11, no. 1, pp. 1–22, 2021, doi: 10.3390/nano11010040.

[66] R. Hergt, S. Dutz, and M. Röder, "Effects of size distribution on hysteresis losses of magnetic nanoparticles for hyperthermia," *J. Phys. Condens. Matter*, vol. 20, no. 38, 2008, doi: 10.1088/0953-8984/20/38/385214.

[67] R. K. GILCHRIST, R. MEDAL, W. D. SHOREY, R. C. HANSELMAN, J. C. PARROTT, and C. B. TAYLOR, "Selective inductive heating of lymph nodes," *Ann. Surg.*, vol. 146, no. 4, pp. 596–606, Oct. 1957, doi: 10.1097/00000658-195710000-00007.

[68] A. LeBrun, R. Ma, and L. Zhu, "MicroCT image based simulation to design heating protocols in magnetic nanoparticle hyperthermia for cancer treatment," *J. Therm. Biol.*, vol. 62, pp. 129–137, 2016, doi: 10.1016/j.jtherbio.2016.06.025.

[69] M. Lahonian and A. A. Golneshan, "Numerical study of temperature distribution in a spherical tissue in magnetic fluid hyperthermia using lattice Boltzmann method.," *IEEE Trans. Nanobioscience*, vol. 10, no. 4, pp. 262–268, Dec. 2011, doi: 10.1109/TNB.2011.2177100.

[70] A. A. Golneshan and M. Lahonian, "Diffusion of magnetic nanoparticles in a multi-site injection process within a biological tissue during magnetic fluid hyperthermia using lattice Boltzmann method," *Mech. Res. Commun.*, vol. 38, no. 6, pp. 425–430, 2011, doi: 10.1016/j.mechrescom.2011.05.012.

[71] A. Attaluri *et al.*, "Magnetic nanoparticle hyperthermia enhances radiation therapy: A study in mouse models of human prostate cancer," *Int. J. Hyperth.*, vol. 31, no. 4, pp. 359–374, 2015, doi: 10.3109/02656736.2015.1005178.

[72] S. K. Kandala, E. Liapi, L. L. Whitcomb, A. Attaluri, and R. Ivkov, "Temperature-controlled power modulation compensates for heterogeneous nanoparticle distributions: a computational optimization analysis for magnetic hyperthermia," *Int. J. Hyperth.*, vol. 36, no. 1, pp. 115–129, 2019, doi: 10.1080/02656736.2018.1538538.

[73] K. Shen, Y. Yan, W. Gao, and L. Li, "Numerical simulation of the effect of injection sites arrangement on the thermal ablation in the magnetic fluid hyperthermia," *J. Magn. Magn. Mater.*, vol. 555, no. January, p. 169393, 2022, doi: 10.1016/j.jmmm.2022.169393.

[74] F. Soetaert, L. Dupré, R. Ivkov, and G. Crevecoeur, "Computational evaluation of amplitude modulation for enhanced magnetic nanoparticle hyperthermia," *Biomed. Tech.*, vol. 60, no. 5, pp. 491–504, 2015, doi: 10.1515/bmt-2015-0046.

[75] M. Salloum, R. Ma, and L. Zhu, "Enhancement in treatment planning for magnetic

nanoparticle hyperthermia: Optimization of the heat absorption pattern," *Int. J. Hyperth.*, vol. 25, no. 4, pp. 309–321, Jan. 2009, doi: 10.1080/02656730902803118.

[76] G. Singh, N. Kumar, and P. K. Avti, "Computational evaluation of effectiveness for intratumoral injection strategies in magnetic nanoparticle assisted thermotherapy," *Int. J. Heat Mass Transf.*, vol. 148, p. 119129, 2020, doi: 10.1016/j.ijheatmasstransfer.2019.119129.

[77] A. Attaluri, R. Ma, Y. Qiu, W. Li, and L. Zhu, "Nanoparticle distribution and temperature elevations in prostatic tumours in mice during magnetic nanoparticle hyperthermia," *Int. J. Hyperth.*, vol. 27, no. 5, pp. 491–502, 2011, doi: 10.3109/02656736.2011.584856.

[78] I. HILGER, R. HIERGEIST, R. HERGT, K. WINNEFELD, H. SCHUBERT, and W. A. KAISER, "Thermal Ablation of Tumors Using Magnetic Nanoparticles: An In Vivo Feasibility Study," *Invest. Radiol.*, vol. 37, no. 10, 2002, [Online]. Available: https://journals.lww.com/investigativeradiology/fulltext/2002/10000/thermal_ablation_of_tumors_using_magnetic.8.aspx

[79] I. Hilger, "In vivo applications of magnetic nanoparticle hyperthermia," *Int. J. Hyperth.*, vol. 29, no. 8, pp. 828–834, 2013, doi: 10.3109/02656736.2013.832815.

[80] A. Attaluri *et al.*, "Magnetic nanoparticle hyperthermia enhances radiation therapy: A study in mouse models of human prostate cancer," *Int. J. Hyperth.*, vol. 31, no. 4, pp. 359–374, 2015, doi: 10.3109/02656736.2015.1005178.

[81] Q. Jiang *et al.*, "On the magnetic nanoparticle injection strategy for hyperthermia treatment," *Int. J. Mech. Sci.*, vol. 235, no. September, p. 107707, 2022, doi: 10.1016/j.ijmecsci.2022.107707.

[82] Y. D. Tang, R. C. C. Flesch, and T. Jin, "Injection Strategy for the Optimization of Therapeutic Temperature Profile Considering Irregular Tumors in Magnetic Hyperthermia," *IEEE Trans. Magn.*, vol. 54, no. 6, pp. 5–10, 2018, doi: 10.1109/TMAG.2018.2808206.

[83] N. Mahesh, N. Singh, and P. Talukdar, "Investigation of a breast cancer magnetic hyperthermia through mathematical modeling of intratumoral nanoparticle distribution and temperature elevations," *Therm. Sci. Eng. Prog.*, vol. 40, p. 101756, 2023, doi: https://doi.org/10.1016/j.tsep.2023.101756.

[84] A. Dahaghin *et al.*, "A numerical investigation into the magnetic nanoparticles hyperthermia cancer treatment injection strategies," *Biocybern. Biomed. Eng.*, vol. 41, no. 2, pp. 516–526, 2021, doi: 10.1016/j.bbe.2021.04.002.

[85] A. Singh and N. Kumar, "A coupled finite-volume immersed boundary method for the simulation of bioheat transfer in 3D complex tumor," *Eng. Comput.*, vol. imm, no. 0123456789, 2023, doi: 10.1007/s00366-023-01797-9.

[86] V. E. Orel *et al.*, "Computer-assisted Inductive Moderate Hyperthermia Planning for Breast Cancer Patients," *2020 IEEE 40th Int. Conf. Electron. Nanotechnology, ELNANO 2020 - Proc.*, pp. 474–477, 2020, doi: 10.1109/ELNANO50318.2020.9088908.

[87] D. Zhang *et al.*, “Multiple antenna placement in microwave ablation assisted by a three-dimensional fusion image navigation system for hepatocellular carcinoma,” *Int. J. Hyperth.*, vol. 35, no. 1, pp. 122–132, 2018, doi: 10.1080/02656736.2018.1484183.

[88] E. J. Xu *et al.*, “Immediate evaluation and guidance of liver cancer thermal ablation by three-dimensional ultrasound/contrast-enhanced ultrasound fusion imaging,” *Int. J. Hyperth.*, vol. 34, no. 6, pp. 870–876, 2018, doi: 10.1080/02656736.2017.1373306.

[89] I. Hilger, W. Andrä, R. Hergt, R. Hiergeist, H. Schubert, and W. A. Kaiser, “Electromagnetic Heating of Breast Tumors in Interventional Radiology: In Vitro and in Vivo Studies in Human Cadavers and Mice,” *Radiology*, vol. 218, no. 2, pp. 570–575, Feb. 2001, doi: 10.1148/radiology.218.2.r01fe19570.

[90] K. Maier-Hauff *et al.*, “Intracranial Thermotherapy using Magnetic Nanoparticles Combined with External Beam Radiotherapy: Results of a Feasibility Study on Patients with Glioblastoma Multiforme,” *J. Neurooncol.*, vol. 81, no. 1, pp. 53–60, 2007, doi: 10.1007/s11060-006-9195-0.

[91] S. J. DeNardo *et al.*, “Thermal Dosimetry Predictive of Efficacy of ¹¹¹In-ChL6 Nanoparticle AMF–Induced Thermoablative Therapy for Human Breast Cancer in Mice,” *J. Nucl. Med.*, vol. 48, no. 3, pp. 437 LP – 444, Mar. 2007, [Online]. Available: http://jnm.snmjournals.org/content/48/3/437.abstract

[92] H. S. Huang and J. F. Hainfeld, “Intravenous magnetic nanoparticle cancer hyperthermia,” *Int. J. Nanomedicine*, vol. 8, pp. 2521–2532, 2013, doi: 10.2147/IJN.S43770.

[93] S. Balivada *et al.*, “A/C magnetic hyperthermia of melanoma mediated by iron(0)/iron oxide core/shell magnetic nanoparticles: A mouse study,” *BMC Cancer*, vol. 10, 2010, doi: 10.1186/1471-2407-10-119.

[94] I. Hilger, R. Hergt, and W. A. Kaiser, “Towards breast cancer treatment by magnetic heating,” *J. Magn. Magn. Mater.*, vol. 293, no. 1, pp. 314–319, 2005, doi: 10.1016/j.jmmm.2005.02.026.

[95] K. Maier-Hauff *et al.*, “Efficacy and safety of intratumoral thermotherapy using magnetic iron-oxide nanoparticles combined with external beam radiotherapy on patients with recurrent glioblastoma multiforme,” *J. Neurooncol.*, vol. 103, no. 2, pp. 317–324, 2011, doi: 10.1007/s11060-010-0389-0.

[96] A. Etminan *et al.*, “Simulation of heat transfer, mass transfer and tissue damage in magnetic nanoparticle hyperthermia with blood vessels,” *J. Therm. Biol.*, vol. 110, no. September, p. 103371, 2022, doi: 10.1016/j.jtherbio.2022.103371.

[97] A. Etminan, M. Salimibani, A. Dahaghin, M. Haghpanahi, and A. Maleki, “FEM thermal assessment of a 3-D irregular tumor with capillaries in magnetic nanoparticle hyperthermia via dissimilar injection points,” *Comput. Biol. Med.*, vol. 157, no. November 2022, p. 106771, 2023, doi: 10.1016/j.compbiomed.2023.106771.

[98] I. Astefanoaei, H. Chiriac, and A. Stancu, “Investigation of the temperature field in the magnetic hyperthermia using FeCrNbB magnetic particles,” *Eur. Phys. J. Plus*, vol. 131,

no. 9, pp. 1–9, 2016, doi: 10.1140/epjp/i2016-16322-1.

[99] T. Arun *et al.*, "Size dependent magnetic and capacitive performance of MnFe2O4 magnetic nanoparticles," *Mater. Lett.*, vol. 276, p. 128240, 2020, doi: 10.1016/j.matlet.2020.128240.

[100] K. V. Chandekar and K. M. Kant, "Effect of size and shape dependent anisotropy on superparamagnetic property of CoFe2O4 nanoparticles and nanoplatelets," *Phys. B Condens. Matter*, vol. 520, pp. 152–163, 2017, doi: 10.1016/j.physb.2017.06.001.

[101] A. Jordan, P. Wust, H. Fähling, W. John, A. Hinz, and R. Felix, "Inductive heating of ferrimagnetic particles and magnetic fluids: Physical evaluation of their potential for hyperthermia," *Int. J. Hyperth.*, vol. 25, no. 7, pp. 499–511, 2009, doi: 10.3109/02656730903287790.

[102] Z. Li, M. Kawashita, N. Araki, M. Mitsumori, M. Hiraoka, and M. Doi, "Magnetite nanoparticles with high heating efficiencies for application in the hyperthermia of cancer," *Mater. Sci. Eng. C*, vol. 30, no. 7, pp. 990–996, 2010, doi: https://doi.org/10.1016/j.msec.2010.04.016.

[103] A. I. Prasad *et al.*, "Bi-functional properties of Fe3O4@YPO4:Eu hybrid nanoparticles: Hyperthermia application," *Dalt. Trans.*, vol. 42, no. 14, pp. 4885–4896, 2013, doi: 10.1039/c2dt32508j.

[104] A. J. GIUSTINI, A. A. PETRYK, S. M. CASSIM, J. A. TATE, I. BAKER, and P. J. HOOPES, "Magnetic Nanoparticle Hyperthermia in Cancer Treatment," *Nano Life*, vol. 01, no. 01n02, pp. 17–32, 2010, doi: 10.1142/s1793984410000067.

[105] K. V. Chandekar and K. M. Kant, "Size-strain analysis and elastic properties of CoFe2O4 nanoplatelets by hydrothermal method," *J. Mol. Struct.*, vol. 1154, pp. 418–427, 2018, doi: 10.1016/j.molstruc.2017.09.104.

[106] A. Gholizadeh, "A comparative study of physical properties in Fe 3 O 4 nanoparticles prepared by coprecipitation and citrate methods," no. October 2016, 2017, doi: 10.1111/jace.14896.

[107] D. Ravinder and T. Alivelumanga, "Composition dependence of elastic behaviour of mixed manganese-zinc ferrites," *Mater. Lett.*, vol. 37, no. 1–2, pp. 51–56, 1998, doi: 10.1016/S0167-577X(98)00062-7.

[108] B. Issa, I. M. Obaidat, B. A. Albiss, and Y. Haik, "Magnetic nanoparticles: Surface effects and properties related to biomedicine applications," *Int. J. Mol. Sci.*, vol. 14, no. 11, pp. 21266–21305, 2013, doi: 10.3390/ijms141121266.

[109] G. F. Goya and M. P. Morales, "Field dependence of blocking temperature in magnetite nanoparticles," *J. Metastable Nanocrystalline Mater.*, vol. 20–21, pp. 673–678, 2004, doi: 10.4028/www.scientific.net/JMNM.20-21.673.

[110] A. López-Ortega, E. Lottini, C. D. J. Fernández, and C. Sangregorio, "Exploring the Magnetic Properties of Cobalt-Ferrite Nanoparticles for the Development of a Rare-Earth-Free Permanent Magnet," *Chem. Mater.*, vol. 27, no. 11, pp. 4048–4056, 2015, doi: 10.1021/acs.chemmater.5b01034.

[111] T. E. Torres *et al.*, “Magnetic properties and energy absorption of CoFe2O4 nanoparticles for magnetic hyperthermia,” *J. Phys. Conf. Ser.*, vol. 200, no. SECTION 7, 2010, doi: 10.1088/1742-6596/200/7/072101.

[112] R. Hergt, S. Dutz, R. Müller, and M. Zeisberger, “Magnetic particle hyperthermia: Nanoparticle magnetism and materials development for cancer therapy,” *J. Phys. Condens. Matter*, vol. 18, no. 38, 2006, doi: 10.1088/0953-8984/18/38/S26.

[113] T. Hanemann and D. V. Szabó, *Polymer-nanoparticle composites: From synthesis to modern applications*, vol. 3, no. 6. 2010. doi: 10.3390/ma3063468.

[114] K. L. Lopez Maldonado *et al.*, “Effects of grain boundary width and crystallite size on conductivity and magnetic properties of magnetite nanoparticles,” *J. Nanoparticle Res.*, vol. 16, no. 7, 2014, doi: 10.1007/s11051-014-2482-3.

[115] K. Maaz, A. Mumtaz, S. K. Hasanain, and A. Ceylan, “Synthesis and magnetic properties of cobalt ferrite (CoFe2O4) nanoparticles prepared by wet chemical route,” *J. Magn. Magn. Mater.*, vol. 308, no. 2, pp. 289–295, 2007, doi: 10.1016/j.jmmm.2006.06.003.

[116] Z. X. Tang, C. M. Sorensen, K. J. Klabunde, and G. C. Hadjipanayis, “Size-dependent magnetic properties of manganese ferrite fine particles,” *J. Appl. Phys.*, vol. 69, no. 8, pp. 5279–5281, 1991, doi: 10.1063/1.348048.

[117] T. Arun *et al.*, “Size dependent magnetic and capacitive performance of MnFe2O4 magnetic nanoparticles,” *Mater. Lett.*, vol. 276, p. 128240, 2020, doi: 10.1016/j.matlet.2020.128240.

[118] Y. Iqbal, H. Bae, I. Rhee, and S. Hong, “Magnetic heating of silica-coated manganese ferrite nanoparticles,” *J. Magn. Magn. Mater.*, vol. 409, pp. 80–86, 2016, doi: 10.1016/j.jmmm.2016.02.078.

[119] C. Iacovita *et al.*, “Hyperthermia, cytotoxicity, and cellular uptake properties of manganese and zinc ferrite magnetic nanoparticles synthesized by a polyol-mediated process,” *Nanomaterials*, vol. 9, no. 10, pp. 1–23, 2019, doi: 10.3390/nano9101489.

[120] A. Makridis *et al.*, “In vitro application of Mn-ferrite nanoparticles as novel magnetic hyperthermia agents,” *J. Mater. Chem. B*, vol. 2, no. 47, pp. 8390–8398, 2014, doi: 10.1039/c4tb01017e.

[121] X. L. Liu *et al.*, “Magnetic nanoparticle-loaded polymer nanospheres as magnetic hyperthermia agents,” *J. Mater. Chem. B*, vol. 2, no. 1, pp. 120–128, 2014, doi: 10.1039/c3tb21146k.

[122] E. Mazarío *et al.*, “High specific absorption rate and transverse relaxivity effects in manganese ferrite nanoparticles obtained by an electrochemical route,” *J. Phys. Chem. C*, vol. 119, no. 12, pp. 6828–6834, 2015, doi: 10.1021/jp510937r.

[123] Y. V. Kolen’Ko *et al.*, “Large-scale synthesis of colloidal Fe3O4 nanoparticles exhibiting high heating efficiency in magnetic hyperthermia,” *J. Phys. Chem. C*, vol. 118, no. 16, pp. 8691–8701, 2014, doi: 10.1021/jp500816u.

[124] S. Verma and D. Pravarthana, “One-pot synthesis of highly monodispersed ferrite nanocrystals: Surface characterization and magnetic properties,” *Langmuir*, vol. 27, no. 21, pp. 13189–13197, 2011, doi: 10.1021/la202394n.

[125] P. Kucheryavy *et al.*, “Superparamagnetic iron oxide nanoparticles with variable size and an iron oxidation state as prospective imaging agents,” *Langmuir*, vol. 29, no. 2, pp. 710–716, 2013, doi: 10.1021/la3037007.

[126] S. Ge *et al.*, “Facile hydrothermal synthesis of iron oxide nanoparticles with tunable magnetic properties,” *J. Phys. Chem. C*, vol. 113, no. 31, pp. 13593–13599, 2009, doi: 10.1021/jp902953t.

[127] C. Vázquez-Vázquez, M. A. López-Quintela, M. C. Buján-Núñez, and J. Rivas, “Finite size and surface effects on the magnetic properties of cobalt ferrite nanoparticles,” *J. Nanoparticle Res.*, vol. 13, no. 4, pp. 1663–1676, 2011, doi: 10.1007/s11051-010-9920-7.

[128] G. Baldi *et al.*, “Synthesis and coating of cobalt ferrite nanoparticles: A first step toward the obtainment of new magnetic nanocarriers,” *Langmuir*, vol. 23, no. 7, pp. 4026–4028, 2007, doi: 10.1021/la063255k.

[129] K. O. Abdulwahab *et al.*, “A one-pot synthesis of monodispersed iron cobalt oxide and iron manganese oxide nanoparticles from bimetallic pivalate clusters,” *Chem. Mater.*, vol. 26, no. 2, pp. 999–1013, 2014, doi: 10.1021/cm403047v.

[130] M. S. Shakil *et al.*, “In Vivo Toxicity Studies of Chitosan-Coated Cobalt Ferrite Nanocomplex for Its Application as MRI Contrast Dye,” *ACS Appl. Bio Mater.*, 2020, doi: 10.1021/acsabm.0c01069.

[131] J. A. Peters, “Relaxivity of manganese ferrite nanoparticles,” *Prog. Nucl. Magn. Reson. Spectrosc.*, vol. 120–121, pp. 72–94, 2020, doi: 10.1016/j.pnmrs.2020.07.002.

[132] P. T. Phong, N. X. Phuc, P. H. Nam, N. V. Chien, D. D. Dung, and P. H. Linh, “Size-controlled heating ability of CoFe2O4 nanoparticles for hyperthermia applications,” *Phys. B Condens. Matter*, vol. 531, no. September 2017, pp. 30–34, 2018, doi: 10.1016/j.physb.2017.12.010.

[133] Y. Piñeiro-Redondo, M. Bañobre-López, I. Pardiñas-Blanco, G. Goya, M. A. López-Quintela, and J. Rivas, “The influence of colloidal parameters on the specific power absorption of PAA-coated magnetite nanoparticles,” *Nanoscale Res. Lett.*, vol. 6, pp. 1–7, 2011, doi: 10.1186/1556-276X-6-383.

[134] G. Kandasamy, A. Sudame, T. Luthra, K. Saini, and D. Maity, “Functionalized Hydrophilic Superparamagnetic Iron Oxide Nanoparticles for Magnetic Fluid Hyperthermia Application in Liver Cancer Treatment,” *ACS Omega*, vol. 3, no. 4, pp. 3991–4005, 2018, doi: 10.1021/acsomega.8b00207.

[135] S. Dutz and R. Hergt, “Magnetic nanoparticle heating and heat transfer on a microscale: Basic principles, realities and physical limitations of hyperthermia for tumour therapy,” *Int. J. Hyperth.*, vol. 29, no. 8, pp. 790–800, Dec. 2013, doi: 10.3109/02656736.2013.822993.

[136] A. Karimi and M. Navidbakhsh, “Material properties in unconfined compression of gelatin hydrogel for skin tissue engineering applications,” vol. 59, no. 6, pp. 479–486, 2014, doi: doi:10.1515/bmt-2014-0028.

[137] M. Javidi *et al.*, “Cylindrical agar gel with fluid flow subjected to an alternating magnetic field during hyperthermia,” *Int. J. Hyperth.*, vol. 31, no. 1, pp. 33–39, 2015, doi: 10.3109/02656736.2014.988661.

[138] Y. Kaur, A. Chandel, and B. Chudasama, “Magnetic hyperthermia of AFe2O4 (A = Fe, Mn, Co) nanoparticles prepared by Co-precipitation method,” *AIP Adv.*, vol. 13, no. 2, p. 25034, Feb. 2023, doi: 10.1063/9.0000478.

[139] S. Y. Wang, S. Huang, and D. A. Borca-Tasciuc, “Potential sources of errors in measuring and evaluating the specific loss power of magnetic nanoparticles in an alternating magnetic field,” *IEEE Trans. Magn.*, vol. 49, no. 1, pp. 255–262, 2013, doi: 10.1109/TMAG.2012.2224648.

[140] L. Kranold, J. Boparai, L. Fortaleza, and M. Popovic, “Skin Phantoms for Microwave Breast Cancer Detection: A Comparative Study,” *IEEE J. Electromagn. RF Microwaves Med. Biol.*, vol. 6, no. 2, pp. 175–181, 2022, doi: 10.1109/JERM.2021.3084126.

[141] Z. J. Fu, Q. Xi, L. Ling, and C. Y. Cao, “Numerical investigation on the effect of tumor on the thermal behavior inside the skin tissue,” *Int. J. Heat Mass Transf.*, vol. 108, pp. 1154–1163, 2017, doi: 10.1016/j.ijheatmasstransfer.2016.11.109.

[142] D. Fiala, K. J. Lomas, and M. Stohrer, “Computer prediction of human thermoregulatory and temperature responses to a wide range of environmental conditions.,” *Int. J. Biometeorol.*, vol. 45, no. 3, pp. 143–159, Sep. 2001, doi: 10.1007/s004840100099.

[143] A. Sobolewski, M. Młynarczyk, M. Konarska, and J. Bugajska, “The influence of air humidity on human heat stress in a hot environment,” *Int. J. Occup. Saf. Ergon.*, pp. 1–11, Nov. 2019, doi: 10.1080/10803548.2019.1699728.

[144] Y. Kurazumi and L. Rezgals, “Convective Heat Transfer Coefficients of the Human Body under Forced Convection from Ceiling,” *J. Ergon.*, vol. 04, no. 01, pp. 1–6, 2014, doi: 10.4172/2165-7556.1000126.

[145] A. Singh and N. Kumar, “Parameterizing the Effects of Tumor Shape in Magnetic Nanoparticle Thermotherapy Through a Computational Approach,” *J. Heat Transfer*, vol. 144, no. 3, Jan. 2022, doi: 10.1115/1.4052967.

[146] V. P. Saxena and D. Arya, “Steady-state heat distribution in epidermis, dermis and subdermal tissues,” *J. Theor. Biol.*, vol. 89, no. 3, pp. 423–432, 1981, doi: 10.1016/0022-5193(81)90360-X.

[147] “American Cancer Society. Types of Breast Cancer | About Breast Cancer.” https://www.cancer.org/cancer/breast-cancer/about/types-of-breast-cancer.html (accessed Mar. 28, 2022).

[148] A. Rydholm and P. Gustafson, “Should tumor depth be included in prognostication of soft tissue sarcoma?,” *BMC Cancer*, vol. 3, pp. 1–5, 2003, doi: 10.1186/1471-2407-3-17.

[149] Y. Kurazumi, T. Tsuchikawa, J. Ishii, K. Fukagawa, Y. Yamato, and N. Matsubara, "Radiative and convective heat transfer coefficients of the human body in natural convection," *Build. Environ.*, vol. 43, no. 12, pp. 2142–2153, 2008, doi: https://doi.org/10.1016/j.buildenv.2007.12.012.

[150] R. J. de Dear, E. Arens, Z. Hui, and M. Oguro, "Convective and radiative heat transfer coefficients for individual human body segments.," *Int. J. Biometeorol.*, vol. 40, no. 3, pp. 141–156, May 1997, doi: 10.1007/s004840050035.

[151] A. Shajahan, C. H. Culp, and B. Williamson, "Effects of indoor environmental parameters related to building heating, ventilation, and air conditioning systems on patients' medical outcomes: A review of scientific research on hospital buildings," *Indoor Air*, vol. 29, no. 2, pp. 161–176, 2019, doi: 10.1111/ina.12531.

[152] H. Zhang *et al.*, "Air movement preferences observed in office buildings," *Int. J. Biometeorol.*, vol. 51, no. 5, pp. 349–360, 2007, doi: 10.1007/s00484-006-0079-y.

[153] H. H. Pennes, "Analysis of Tissue and Arterial Blood Temperatures in the Resting Human Forearm," *J. Appl. Physiol.*, vol. 1, no. 2, pp. 93–122, Aug. 1948, doi: 10.1152/jappl.1948.1.2.93.

[154] P. Das, M. Colombo, and D. Prosperi, "Recent advances in magnetic fluid hyperthermia for cancer therapy," *Colloids Surfaces B Biointerfaces*, vol. 174, no. July 2018, pp. 42–55, 2019, doi: 10.1016/j.colsurfb.2018.10.051.

[155] B. Sanz *et al.*, "In silico before in vivo: How to predict the heating efficiency of magnetic nanoparticles within the intracellular space," *Sci. Rep.*, vol. 6, no. December, pp. 1–10, 2016, doi: 10.1038/srep38733.

[156] S. Singh and R. Repaka, "Effect of different breast density compositions on thermal damage of breast tumor during radiofrequency ablation," *Appl. Therm. Eng.*, vol. 125, pp. 443–451, 2017, doi: https://doi.org/10.1016/j.applthermaleng.2017.07.057.

[157] M. Lahonian and A. A. Golneshan, "Numerical study of temperature distribution in a spherical tissue in magnetic fluid hyperthermia using lattice Boltzmann method," *IEEE Trans. Nanobioscience*, vol. 10, no. 4, pp. 262–268, 2011, doi: 10.1109/TNB.2011.2177100.

[158] S. Dutz and R. Hergt, "Magnetic nanoparticle heating and heat transfer on a microscale: Basic principles, realities and physical limitations of hyperthermia for tumour therapy," *Int. J. Hyperth.*, vol. 29, no. 8, pp. 790–800, 2013, doi: 10.3109/02656736.2013.822993.

[159] S. K. Kandala, E. Liapi, L. L. Whitcomb, A. Attaluri, and R. Ivkov, "Temperature-controlled power modulation compensates for heterogeneous nanoparticle distributions: a computational optimization analysis for magnetic hyperthermia," *Int. J. Hyperth.*, vol. 36, no. 1, pp. 115–129, Jan. 2019, doi: 10.1080/02656736.2018.1538538.

[160] J. A. Pearce, "Relationship between Arrhenius models of thermal damage and the CEM 43 thermal dose," *Energy-based Treat. Tissue Assess. V*, vol. 7181, no. 2, p. 718104, 2009, doi: 10.1117/12.807999.

[161] S. A. Sapareto and W. C. Dewey, "Thermal dose determination in cancer therapy," *Int.*

J. Radiat. Oncol., vol. 10, no. 6, pp. 787–800, 1984, doi: https://doi.org/10.1016/0360-3016(84)90379-1.

[162] G. Singh, A. Paul, H. Shekhar, and A. Paul, "Pulsed Ultrasound Assisted Thermo-Therapy for Subsurface Tumor Ablation: A Numerical Investigation," *J. Therm. Sci. Eng. Appl.*, vol. 13, no. 4, Jan. 2021, doi: 10.1115/1.4048674.

[163] M. W. Dewhirst, Z. Vujaskovic, E. Jones, and D. Thrall, "Re-setting the biologic rationale for thermal therapy," *Int. J. Hyperth.*, vol. 21, no. 8, pp. 779–790, Dec. 2005, doi: 10.1080/02656730500271668.

[164] G. C. van Rhoon, T. Samaras, P. S. Yarmolenko, M. W. Dewhirst, E. Neufeld, and N. Kuster, "CEM43°C thermal dose thresholds: a potential guide for magnetic resonance radiofrequency exposure levels?," *Eur. Radiol.*, vol. 23, no. 8, pp. 2215–2227, 2013, doi: 10.1007/s00330-013-2825-y.

[165] M. Liangruksa, R. Ganguly, and I. K. Puri, "Parametric investigation of heating due to magnetic fluid hyperthermia in a tumor with blood perfusion," *J. Magn. Magn. Mater.*, vol. 323, no. 6, pp. 708–716, 2011, doi: 10.1016/j.jmmm.2010.10.027.

[166] A. Bhowmik, R. Singh, R. Repaka, and S. C. Mishra, "Conventional and newly developed bioheat transport models in vascularized tissues: A review," *J. Therm. Biol.*, vol. 38, no. 3, pp. 107–125, 2013, doi: 10.1016/j.jtherbio.2012.12.003.

[167] R. Hergt, S. Dutz, and M. Zeisberger, "Validity limits of the Néel relaxation model of magnetic nanoparticles for hyperthermia.," *Nanotechnology*, vol. 21, no. 1, p. 015706, 2010, doi: 10.1088/0957-4484/21/1/015706.

[168] S. Singh and R. Melnik, "Thermal ablation of biological tissues in disease treatment: A review of computational models and future directions," *Electromagn. Biol. Med.*, vol. 39, no. 2, pp. 49–88, 2020, doi: 10.1080/15368378.2020.1741383.

[169] B. K. Byrd *et al.*, "The shape of breast cancer," *Breast Cancer Res. Treat.*, vol. 183, no. 2, pp. 403–410, 2020, doi: 10.1007/s10549-020-05780-6.

[170] G. Singh, A. Singh, N. Kumar, and P. Avti, "Effects of injection rates and tissue diffusivity in magnetic nano-particle hyperthermia," *Med. Eng. Phys.*, vol. 113, no. July 2022, p. 103965, 2023, doi: 10.1016/j.medengphy.2023.103965.

[171] S. Kossatz *et al.*, "High therapeutic efficiency of magnetic hyperthermia in xenograft models achieved with moderate temperature dosages in the tumor area," *Pharm. Res.*, vol. 31, no. 12, pp. 3274–3288, 2014, doi: 10.1007/s11095-014-1417-0.

[172] G. Bellizzi, O. M. Bucci, and G. Chirico, "Numerical assessment of a criterion for the optimal choice of the operative conditions in magnetic nanoparticle hyperthermia on a realistic model of the human head," *Int. J. Hyperth.*, vol. 32, no. 6, pp. 688–703, 2016, doi: 10.3109/02656736.2016.1167258.

[173] N. C. Institute, "The Cancer Imaging Archive," 2015. https://www.cancerimagingarchive.net/nbia-search/?CollectionCriteria=QIN Breast DCE-MRI (accessed Oct. 02, 2022).

[174] A. Fedorov *et al.*, "3D Slicer as an image computing platform for the Quantitative Imaging Network," *Magn. Reson. Imaging*, vol. 30, no. 9, pp. 1323–1341, 2012, doi: 10.1016/j.mri.2012.05.001.

[175] D. Y. Chan, S. R. Moavenzadeh, T. J. Polascik, M. L. Palmeri, and K. R. Nightingale, "Screening and Image-Guided Targeted Biopsy of Prostate Cancer Using 3D Acoustic Radiation Force Impulse (ARFI) Imaging," *IEEE Int. Ultrason. Symp. IUS*, vol. 2022-Octob, 2022, doi: 10.1109/IUS54386.2022.9957510.

[176] H. Veerman *et al.*, "3D-Reconstructed Contact Surface Area and Tumour Volume on Magnetic Resonance Imaging Improve the Prediction of Extraprostatic Extension of Prostate Cancer," *J. Digit. Imaging*, no. 0123456789, 2022, doi: 10.1007/s10278-022-00756-y.

[177] A. C. Society, "Types of Breast Cancer | About Breast Cancer." https://www.cancer.org/cancer/breast-cancer/about/types-of-breast-cancer.html (accessed Jan. 17, 2023).

[178] S. Nain, N. Kumar, and P. Kumar Avti, "Computational investigation of the tumor position and ambient conditions on magnetic nanoparticle thermo-therapy," *Therm. Sci. Eng. Prog.*, vol. 34, no. July, p. 101396, 2022, doi: 10.1016/j.tsep.2022.101396.

[179] R. Rahpeima and C. A. Lin, "Numerical study of magnetic hyperthermia ablation of breast tumor on an anatomically realistic breast phantom," *PLoS One*, vol. 17, no. 9 September, pp. 1–30, 2022, doi: 10.1371/journal.pone.0274801.

[180] S. Nain, N. Kumar, B. Chudasama, and P. Kumar Avti, "The SLP estimation of the nanoparticle systems using size-dependent magnetic properties for the magnetic hyperthermia therapy," *J. Magn. Magn. Mater.*, vol. 565, no. November 2022, p. 170219, 2023, doi: 10.1016/j.jmmm.2022.170219.

[181] D. E. Bordelon, C. Cornejo, C. Grttner, F. Westphal, T. L. Deweese, and R. Ivkov, "Magnetic nanoparticle heating efficiency reveals magneto-structural differences when characterized with wide ranging and high amplitude alternating magnetic fields," *J. Appl. Phys.*, vol. 109, no. 12, 2011, doi: 10.1063/1.3597820.

[182] S. Noreen, S. Waheed, D. C. Lu, and D. Tripathi, "Heat stream in electroosmotic bio-fluid flow in straight microchannel via peristalsis," *Int. Commun. Heat Mass Transf.*, vol. 123, p. 105180, 2021, doi: https://doi.org/10.1016/j.icheatmasstransfer.2021.105180.

[183] P. Gas and M. Skowron, "Impact of multiple magnet sources on flow parameters of arterial blood with a specific pulse," in *2018 International Interdisciplinary PhD Workshop (IIPhDW)*, 2018, pp. 244–247. doi: 10.1109/IIPHDW.2018.8388366.

[184] S. Salem and V. Tuchin, "Trapping of magnetic nanoparticles in the blood stream under the influence of a magnetic field," *Izv. Saratov Univ. New Ser. Phys.*, vol. 20, no. 1, pp. 72–79, 2020, doi: 10.18500/1817-3020-2020-20-1-72-79.

[185] S. Nain, N. Kumar, and P. K. Avti, "Tumor size dependent MNP dose evaluation in realistic breast tumor models for effective magnetic hyperthermia.," *Med. Eng. Phys.*, p. 104065, 2023, doi: https://doi.org/10.1016/j.medengphy.2023.104065.